

Faculty of Physics and Astronomy

University of Heidelberg

Diploma thesis

in Physics

submitted by

Jochen Klein

born in Mainz

2008

Commissioning of
and
Preparations for Physics with
the Transition Radiation Detector
in
A Large Ion Collider Experiment
at CERN

Corrected version

This diploma thesis has been carried out by Jochen Klein

at the

Physikalisches Institut

under the supervision of

Frau Prof. Dr. Johanna Stachel

**Inbetriebnahme und Vorbereitungen für Physik
mit dem Übergangsstrahlungsdetektor TRD
bei ALICE (A Large Ion Collider Experiment, CERN)**

Der Large Hadron Collider (LHC) wird sowohl Protonen als auch Schwerionen bei hochrelativistischen Energien zur Kollision bringen. In dem Zusammenstoß werden aus der verfügbaren Energie Teilchen erzeugt. Sie werden in Experimenten nachgewiesen, die um den Wechselwirkungspunkt gebaut sind, um Erkenntnisse über die ablaufenden Prozesse zu gewinnen. ALICE ist spezialisiert auf die Untersuchung von Schwerionen-Kollisionen. Das Experiment besteht aus dem Zusammenschluss einzelner Detektoren, unter ihnen der Übergangsstrahlungsdetektor TRD zur Elektron-/Pion-Separation und als Trigger-Detektor.

Diese Arbeit besteht aus zwei Teilen. Zuerst werden das Testen und die Inbetriebnahme der ersten TRD Supermodule am CERN beschrieben. Der Detektor wurde in Betrieb genommen und in die ALICE-weite Datennahme integriert.

Der zweite Teil beschreibt die Simulation der globalen Spurrekonstruktionseinheit. Sie wurde in die ALICE off-line Umgebung eingebunden und soll für die detaillierte Untersuchung von Trigger-Szenarien verwendet werden, die auf simulierten oder echten Daten basiert werden kann. Schließlich wird die Idee eines Jet-Triggers durch den TRD skizziert.

**Commissioning of and Preparations for Physics with
the Transition Radiation Detector
in A Large Ion Collider Experiment at CERN**

The Large Hadron Collider (LHC) at CERN, Geneva, shall collide protons and heavy-ions at ultrarelativistic energies. At the interaction points new particles are created from the available energy. They are detected and traced in experiments built around the collision point in order to draw conclusions on the initial interactions. A Large Ion Collider Experiment (ALICE) is dedicated to the study of heavy-ion collisions. It comprises a series of special detectors, among them the Transition Radiation Detector (TRD) for e/π -separation and triggering.

This thesis is composed of two parts. First, the testing and commissioning of the first TRD supermodules at CERN is described. The detector has been brought into operation and included in global ALICE data-taking.

The second part discusses the simulation of the Global Tracking Unit (GTU). It has been included in the ALICE off-line framework and shall be used for detailed trigger studies which can be based on simulated or real data. Finally, the idea of a jet trigger contribution from the TRD is sketched.

Contents

1	Introduction	1
1.1	Heavy-ion physics	2
1.2	The Large Hadron Collider	5
1.3	A Large Ion Collider Experiment	8
1.4	The Transition Radiation Detector	9
1.5	Commissioning and Start-Up	10
2	The Transition Radiation Detector	11
2.1	Principle of Operation	11
2.2	Overall structure	14
2.3	Front-End Electronics	16
2.4	DCS Board	19
2.5	Readout scheme	20
2.6	Services	21
2.7	Trigger	22
2.8	Status	24
3	Surface testing	26
3.1	Testing setup	26
3.2	Testing procedure	29
3.2.1	Detector Control System Board	29
3.2.2	Front-end electronics	31
3.2.3	Cooling and temperature measurements	32
3.2.4	Gas system	35
3.2.5	High Voltage	37
3.2.6	Front-End Electronics stress tests	38
3.2.7	JTAG tests	39
3.3	Supermodule repairs	40
3.3.1	Observed issues	40
3.3.2	Supermodule Re-Assembly	41
3.4	Conclusions	43
4	Installation and Commissioning	45
4.1	Installation procedure	45
4.2	Services and Infrastructure	46
4.3	After the insertion of the supermodule	47
4.4	Readout checks	49
4.5	Noise measurements	52
4.5.1	RMS plots	52
4.5.2	Frequency spectrum	52
4.5.3	Common mode current noise	53

4.5.4	Results	54
4.6	Detector Control	54
4.6.1	PCU DIM-server	57
4.6.2	Remote command execution via DIM	57
4.7	Developments during cosmic runs	58
5	Global tracking simulation	63
5.1	Idea of the tracking algorithm	63
5.2	Tracklets	65
5.3	Tracking simulation	69
5.3.1	Input units	70
5.3.2	z -Channel-Units	72
5.3.3	Track matching	73
5.3.4	Merging and Unification	75
5.3.5	p_T -reconstruction	76
5.4	Integration to Off-line Framework	80
5.5	Hardware Comparison	83
5.6	Results	85
5.7	Open issues	87
6	Jets in TRD	88
6.1	Expectations for ALICE	89
6.2	Jet trigger	90
6.2.1	Full Monte-Carlo information	91
6.2.2	Monte-Carlo tracks in the TRD	92
6.2.3	Reconstructed tracks	92
6.2.4	L1-reconstructed tracks	96
6.3	Results and Outlook	96
7	Summary	98
A	Technical Data and Specifications	100
A.1	Tracking parameters	100
B	Checklists	103
B.1	Surface testing checklist	103
B.2	Pre-Installation checklist	104
B.3	Commissioning checklist	105
C	Observed problems	106
C.1	Supermodule I (Sector 8)	106
C.2	Supermodule II (Sector 0)	106
C.3	Supermodule V (Sector 17)	106

List of Figures

1	QCD phase diagram	5
2	LHC and the Experiments	7
3	ALICE overview	8
4	Transition radiation spectrum	11
5	TRD chamber cross-section	12
6	Particle traversing a TRD chamber	13
7	Pulse height	14
8	Pad plane and tilted pads	15
9	TRD structure	16
10	Supermodule structure	16
11	Filter stages in the MCM	17
12	Readout tree	21
13	TRD trigger overview	23
14	TRD trigger sequence	24
15	TRD installation status	25
16	Overview of connections in the cleanroom	27
17	FEE FSM diagram	29
18	InterComLayer and FEE	32
19	Chamber temperature measurement	33
20	Sketch of the cooling connections	34
21	TRAP temperature measurement	35
22	Stress test	39
23	JTAG loops in a supermodule	40
24	Chamber noise	43
25	Overview of the experimental area	45
26	Data acquisition scheme as in the 2008 run	50
27	Common mode noise observed on PASA power supply for SM 00	54
28	Noise comparison with Wiener power supplies PL 512 and PL 508	55
29	Noise using Wiener PL 512 without and with ferrite added.	55
30	FFT spectrum as observed in the installed supermodules	56
31	Coincidence condition for TOF trigger	59
32	Tracklet arrival time	60
33	Cosmic event triggered by TRD	62
34	ADC values for a cosmic track	62
35	Track in TRD stack	64
36	Tracklet classification in z -direction	65
37	From pad plane signal to clusters	66
38	Tracklet without and with magnetic field	68
39	Tracking stages	70
40	Tracklet calculations in input units	71
41	z -Channel map	73

42	Track matching from tracklet lists	74
43	Track merging	76
44	p_T reconstruction	79
45	Simulation and Reconstruction in AliRoot	81
46	ModelSim Environment for comparison of the tracking simulation	84
47	Testbeam setup	85
48	Projected y -position of tracklets	86
49	p_T -distribution of tracks from the testbeam data	86
50	Incident track angle	87
51	Jet in η - φ -grid (MC tracks)	92
52	Efficiency of p_T -cut (MC tracks)	93
53	Efficiency of p_T -cut (MC TRD tracks)	94
54	Efficiency of p_T -cut (ESD tracks)	95
55	Efficiency of p_T -cut (TRD GTU tracks)	97

List of Tables

1	Overview of the Standard Model	3
2	Low voltage channels and typical currents	27
3	Overview of tests done in the cleanroom	30
4	Oxygen contamination	37
5	Electric properties of the high voltage system	38
6	Raw data from one link (case of zs data)	51
7	TRAP trigger timing settings	61
8	TRAP cosmic trigger settings	61
9	Tracklet relevant TRAP registers	68
10	Tracklet information	69
11	Supermodule measures	71
12	Sorting criteria for the z -channel track merging	77
13	Anticipated jet abundances for ALICE	90
14	Jet energy bins used in ALICE	91
15	Tracking parameters	100
16	Values of $A_{k,i}$	101
17	z -channel map listing	102

1 Introduction

The composition and inner structure of matter has been a fundamental and fascinating puzzle for mankind ever since ancient times. It has been addressed in many philosophical studies and the idea of elementary and indivisible (atomos) constituents, general to all matter, was already proposed by Democritus (around 460 - 390 BC). After the Middle Ages in which Aristotle's picture of continuous matter was favoured, the atomic theory was revived in modern science. Providing explanations for experimental observations in chemical reactions (Dalton) it achieved wide acceptance. Whereas the elements consist of only one type of atoms, most materials are made up from compounds of certain atoms. The development of the kinetic gas theory further established the role of atoms by explaining macroscopic laws (Boyle-Mariotte, Gay-Lussac) on the basis of simple and general mechanical principles applied to the microscopic entities.

The subatomic structure was hinted at by the discovery of the electron (e^-) as a charged particle, which is extractable from any material and characterised by its charge-to-mass ratio (J. J. Thomson, 1894-1897). Thus, it was considered a common building block of all matter. This led to intensive research and the formulation of atomic models, such as Thomson's model. The experimental study of the subatomic structure in scattering experiments climaxed in the unexpected discovery of the nucleus carrying almost all the mass of an atom (Geiger, Marsden and Rutherford, 1911). Furthermore, it was found that the arrangement of the elements in the periodic system corresponds to the nuclear charge Z — which itself is equal to the number of electrons bound in the atom by the electromagnetic interaction which was intensively studied in macroscopic systems. Experimental efforts continued and finally revealed the inner structure of the nucleus consisting of nucleons, summarising the charged proton p with the opposite charge of the electron and the neutral neutron n . This picture of the nuclear structure implies the need for a new interaction for the nuclear binding since the equal charge of the protons results in electromagnetic repulsion.

Starting from these known particles — e^- , p , n — many more were found in systematic experiments with cosmic rays and radioactive sources (explained by nuclear reactions resulting in the emission of particles). A dramatic change in the understanding of particle physics was caused by the experimental verification of anti-particles (as negative energy solutions of Dirac's equation, 1928) and the prediction of a so far unobserved particle, the neutrino, to explain the energy spectrum of the e^\pm emitted in radioactive β -decays. The intensive search for new particles led to the particle zoo (due to the vast number). A lot of effort went to understanding the relation between these particles. Sakata's model and others evolved in order to explain the underlying structures. Eventually, the description by the eightfold way (Gell-Mann, Ne'eman) proved very successful and led to the quark model.

An era of particle physics was started in which, besides the discovery of new particles, fundamental concepts of classical physics were tested and surprising results

were found, such as the observation of parity violation. All these experiments led to deep insights in the fundamental structure of matter and the relevant interactions. The theoretical developments lead to the formulation of Quantum Electrodynamics (QED), a theory describing the behaviour of particles under the electromagnetic interaction. The effective force, i. e. the transfer of momentum, results from the exchange of photons. The coupling strength of the elementary single-photon exchange depends on the momentum transferred by the photon, getting stronger with increasing momentum exchange. Interactions with large momentum exchange are often referred to as hard interactions. After its successes, QED was used as paradigm for other Quantum Field Theories.

The developments culminated in a model unifying the electromagnetic and the weak interaction (relevant for the β -decay). Inspired from QED, the strong interaction acting between colour-charged objects (quarks and gluons) was formulated as Quantum Chromodynamics (QCD). It is the basis of the nuclear force.

In contrast to QED, the coupling constant is large and prohibits the perturbative expansion in powers of the coupling constant. But, opposite as in QED, the coupling weakens with increasing momentum transfer. It becomes arbitrarily small for sufficiently high momentum transfers. This feature is known as asymptotic freedom of QCD and results in a perturbative and a non-perturbative regime of QCD.

The Standard Model describes the behaviour of the fundamental fermions (quarks and leptons) under the electroweak and strong interaction by the exchange of gauge bosons (W^\pm, Z^0, γ, g). It contains a limited number of elementary particles, the leptons and quarks (s. Table 1), both arranged in three families, and the exchange bosons. The Standard Model has been extremely successful in quantitative comparisons to experimental results. However, it does not explain the existence of exactly three generations of leptons/quarks and it contains a number of non-intrinsic parameters which have to be taken from experimental measurements. Furthermore, it does not provide an explanation for the very different masses of its fundamental particles and the Higgs mechanism, responsible for the generation of the fermion masses in the Standard Model, has not yet been experimentally verified. Thus, it is not considered a complete and fundamental theory.

1.1 Heavy-ion physics

The experimental non-observation of free colour-charged objects (not bound in hadrons) is interpreted as confinement due to the strong interaction. This confinement is assumed to be a direct consequence of the fundamental QCD interactions in a realm not amenable to perturbative calculations. Gluons as the exchange particles of the strong interaction are coloured objects themselves. Pictorially, the separation of two quarks results in a focused gluon field along the distance. The energy content depends linearly on the length of this colour flux tube. When moving apart the quarks the stored energy becomes sufficiently high to create new particle/antiparticle pairs. Eventually, only colour neutral compounds of quarks, the

Fundamental fermions (Spin- $\frac{1}{2}$):				
Family	Flavour			$Q(e)$
Leptons	e^-	μ^-	τ^-	-1
	ν_e	ν_μ	ν_τ	0
Quarks	u	c	t	$\frac{2}{3}$
	d	s	b	$-\frac{1}{3}$

Interactions:		
Interaction	Mediator	Coupling to
electromagnetic	γ	electric charge
weak	W^\pm, Z^0	weak hypercharge
strong	gluons	colour charge

Table 1: The Standard Model contains three generations of both quarks and leptons. The former are subject to the strong interaction (mediated by the gluons) whereas the latter are only affected by the electroweak interaction (mediated by γ, W^\pm, Z^0)

hadrons, can emerge. However, the detailed mechanisms leading to confinement are not yet fully understood and subject to ongoing research.

Due to the asymptotic freedom of QCD it has been anticipated that nuclear matter at sufficiently high densities and/or temperatures should free the quarks and gluons to form a plasma of colour-charged objects, referred to as Quark Gluon Plasma (QGP). This is reflected in the presumed phase diagram of bulk QCD matter (s. Fig. 1) which shows a hadronic phase and a partonic phase at high densities and/or temperatures.

Sufficiently high densities could appear in the cores of compact neutron (or quark) stars, whereas in the laboratory a stable formation of such a plasma is not feasible. Instead heavy-ion collisions at relativistic energies are used to produce such conditions for a very short time and explore the properties of hot and dense nuclear matter. The collision determines the initial energy density and temperature. In these reactions the system is never static and has a very short lifetime. As further complication, it can only be studied by the emerging reaction products. Such experiments aim at the understanding of QCD confinement and the quest for the QGP.

For the formation of such a plasmonic phase in a heavy-ion collision the products of the initial interactions — sufficiently hard ones can be described by perturbative calculations — have to come rapidly to local thermal equilibrium which requires sufficiently frequent interactions. The outcome would be a finite-size region of locally thermalized partons resulting in high pressure gradients. Such a region appears as medium to traversing particles. If the thermalization is fast enough the expansion and cool-down of the system can be described by relativistic hydrodynamics until it reaches the so-called freeze-out temperature. Then, hadrons are formed and pro-

propagate independently. The hydrodynamic description relies on the input condition and the knowledge of the equation of state specifying the relation between pressure and energy density.

Regardless of the creation of QGP in a collision, the initial properties are not directly observable since the involved partons are confined. The only detectable products are colour-neutral hadrons, leptons and photons emitted from the system at different stages of evolution which can be tracked in particle detectors. The properties of the medium can only be studied by its effect on the finally emitted particles.

Leptons and photons, not undergoing hadronization, give a more direct access to the initial system. But they have to be separated from particles of the same species which are created during later stages of the evolution, e. g. from decays of other particles or the thermal production in the hadronic phase. To understand the process of hadronization — which changes the properties of the emerging particles — it is analysed in nucleon collisions where no medium is formed. The properties of the medium can then be concluded on by the modifications in the case of heavy-ion compared to pp collisions. The details should contain information about the early stage of the collision.

The wish to observe properties of the intermediate plasmonic state raises the need for appropriate probes, i. e. detectable or reconstructable particles carrying information about the initial state. This includes the measurement of heavy-quark vector-resonances, such as J/Ψ and Υ . With the J/Ψ composed of $c\bar{c}$ its yield is believed to depend in a characteristic way on the initial energy density due to its production mechanism as combination of free c, \bar{c} quarks at the phase boundary — leading to a quadratic dependency on the number of free c, \bar{c} . The unstable J/Ψ has to be reconstructed from its decay products. To use the di-electron channel $J/\Psi \rightarrow e^+e^-$ the resulting electrons¹ have to be well identified. The same holds for the Υ . Furthermore, the anticipated event rates require a trigger on such events to achieve statistical significance. In ALICE a multi-level trigger scheme is used which decides at different stages whether the acquisition should be started and continued.

The measurement of particles with open charm or beauty, i. e. imbalanced content of c - or b -quarks, also requires the reliable detection of electron or muon tracks for the reconstruction from their semi-leptonic decays.

Another promising probe for the medium effects are jets due to their production as hadrons resulting from the fragmentation of initial hard partons. They have to propagate through the medium and lose energy thereby (jet quenching). The details of this in-medium modifications are believed to give hints on the medium properties.

With these and other ideas hot and dense nuclear matter was studied experimentally. A series of experiments was carried out at the Alternating Gradient Synchrotron (AGS, BNL) and the Super Proton Synchrotron (SPS, CERN). The

¹In the following, electron refers to both e^- and e^+ .

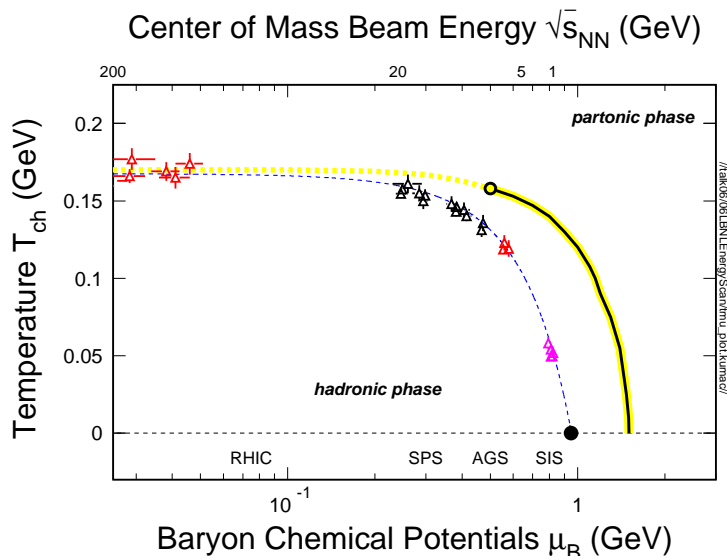


Figure 1: The QCD phase diagram[38]: The horizontal axis shows the baryon chemical potential (corresponding to density) and the relation to the center of mass energy in nuclear collisions resulting in such a density. The vertical axis plots the temperature. The transition from the hadronic phase to the partonic phase (at high temperatures and/or densities) is under experimental investigation.

data was interpreted as an “Evidence for a New State of Matter” [11]. For further studies a dedicated accelerator, the Relativistic Heavy-Ion Collider (RHIC, BNL), was built to achieve higher collision energies and, thus, higher initial energy densities and longer lifetimes of the system before its freeze-out. The data taken within the first years of its operation confirmed the previous results [1].

Besides the experimental efforts there has been great advance in the so-called lattice QCD, referring to numerical calculations of QCD on a discretized space-time lattice. This method depends crucially on input parameters and needs calibration from experiment but is able to produce predictions for other quantities then. Still the computing power is limiting the number of lattice points used in the calculation which makes predictions for the continuum limit more difficult and error-prone.

From both experiment and theory conclusions on the phase diagram of nuclear matter have been drawn and its notion has strongly advanced compared to the first proposal solely indicating the existence of a phase transition from hadronic to deconfined matter.

1.2 The Large Hadron Collider

Despite the big progress in particle physics during the last century there are still many open questions. The Higgs mechanism, responsible for the generation of mass by the spontaneous electroweak symmetry breaking in the Standard Model, has not

yet been verified experimentally by the observation of the Higgs particle.

Having many parameters, the Standard Model is considered to be an effective model arising from an underlying theory. There are many ideas how physics beyond the Standard Model could look like but progress is lacking experimental input. The ideas include supersymmetry, extra dimensions and many more.

In order to study these questions in particle and heavy-ion physics, the need for higher collision energies than achieved in previous accelerator facilities arises. This also requires increased luminosity to sustain reasonable event rates for processes with low cross-sections — typically scaling as $\frac{1}{s}$ where \sqrt{s} is the center of mass energy in the collision.

These demands led to the proposal of a hadron collider with very high beam energy. It was realized by the installation of the Large Hadron Collider (LHC) in the tunnel (about 100 m below surface) formerly used by LEP at CERN. The LHC can store and accelerate different hadrons, such as protons and heavy-ions, up to 7 TeV or 2.75 TeV/nucleon, respectively. To reach the necessary injection energy a series of accelerators is used sequentially, some of them especially built for this purpose.

As shown in Fig. 2 two opposing beams are collided in four interaction points around which particle detectors are installed to study the reaction products. The aim is to detect and reconstruct the trajectories of the emerging particles within a magnetic field to determine the kinetic properties.

The LHC hosts several experiments addressing different fields of physics with the four major experiments being:

ATLAS (A Toroidal LHC ApparatuS)

The experiment is designed to search for the Higgs boson in any of its anticipated decay channels (depending on its actual mass). Furthermore, the possibility of additional massive vector bosons and CP violation can be studied.

CMS (Compact Muon Solenoid)

This experiment also aims at the search for the Higgs boson as well as the search for other new phenomena, such as supersymmetric particles, massive vector bosons, extra dimensions as well as the limitations of the Standard Model. Furthermore a heavy-ion program is planned.

LHCb (LHC beauty)

The major aim of this experiment is the study of the CP violation whose origin is still unclear. The description within the Standard Model is insufficient to explain the observed matter-antimatter asymmetry in the universe.

ALICE (A Large Ion Collider Experiment)

ALICE is the dedicated heavy-ion experiment at the LHC. It is designed to study the QCD confinement and to investigate the Quark Gluon Plasma.

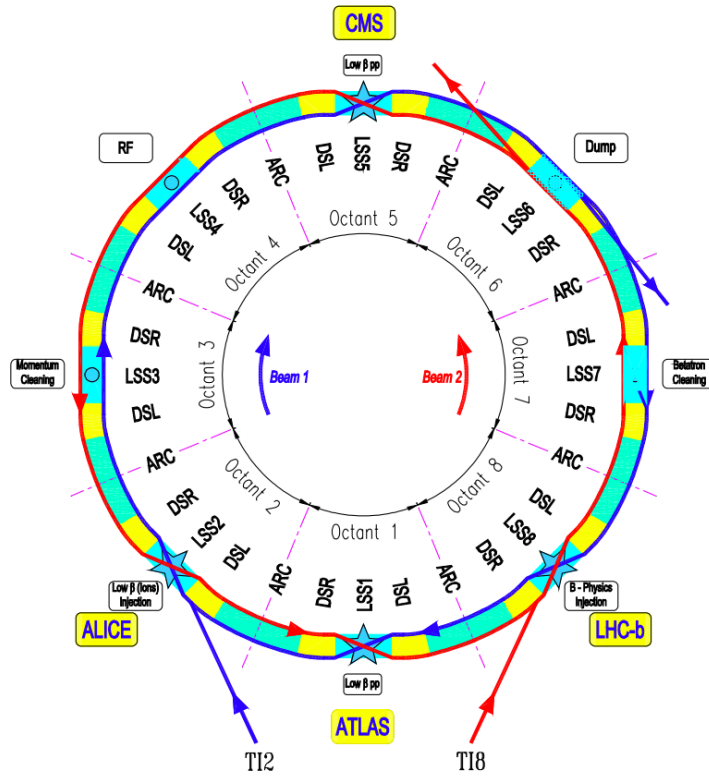


Figure 2: The LHC will store and accelerate two opposing beams of protons or heavy-ions which are collided in the positions where the experiments have been installed. The particles are accelerated in radio-frequency cavities (indicated by RF) along a small section of the ring [9].

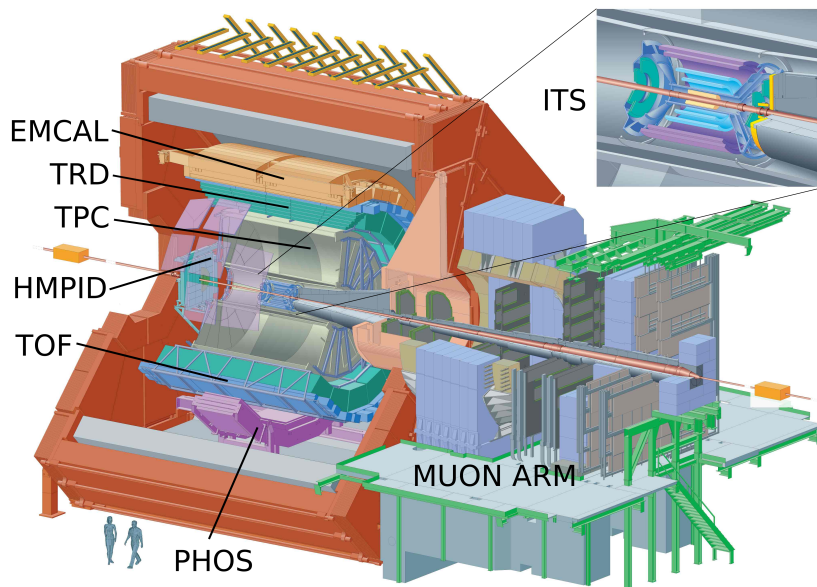


Figure 3: Schematic view of the ALICE detector system: The central barrel of the ALICE detector contains the Inner Tracking System (ITS), the Time Projection Chamber (TPC), the Transition Radiation Detector (TRD) and the Time-Of-Flight (TOF) detector with full azimuthal coverage. Two electromagnetic calorimeters, EMCAL and PHOS, and the High Momentum Particle Identification detector extend the detectors within the magnet. A muon arm is installed in the forward direction.

The needs of the experiments are not equal with respect to the species of the collided particle, the maximum interaction rate etc. Nevertheless, they can be fulfilled by one accelerator implementing different run modes and special focusing elements in front of every experiment. It is foreseen to dedicate about one month per year (10^6 s) to heavy-ion runs.

1.3 A Large Ion Collider Experiment

ALICE addresses the above mentioned questions in the field of heavy-ion physics. The experiment is hosted in a cavern about 50 m below the surface within the LHC ring. The design goal has been the study of the non-perturbative regime of QCD and the investigation of the existence and properties of the Quark-Gluon-Plasma.

The experimental observables by which this understanding shall be gathered are the flavour content of the reaction products and the phase space distribution for hadrons, leptons and photons. The analysis shall be possible on an event-by-event basis.

The ALICE detector design (s. Fig. 3) reflects these aims: The detector consists of a central barrel placed in a homogeneous axial magnetic field (≈ 0.5 T).

Trajectories of charged particles are bent with a momentum dependent curvature. The main tracking device is a large Time Projection Chamber (TPC) with full azimuthal coverage and a pseudo-rapidity range of ± 0.9 as all the barrel detectors². It is capable of the reconstruction of individual charged particle tracks up to the highest anticipated multiplicities of 20000 tracks per event. In order to achieve a high tracking resolution close to the primary vertex (for hyperon, B and D measurements by vertex displacements) an Inner Tracking System (ITS) is installed within the TPC. It consists of six layers of silicon detectors and achieves a vertex position resolution of about $50 \mu\text{m}$. Outside the TPC a Transition Radiation Detector (TRD) is placed allowing electron identification. It is followed by the Time Of Flight detector (TOF) for particle identification (K/p separation) by a precise time measurement. The central barrel detectors are mounted in the spaceframe, a steel support structure.

In addition there are further detectors not covering the full azimuthal acceptance. The High Momentum Particle IDentification (HMPID) detector is based on a Ring Imaging Cherenkov detector (RICH) and gives the possibility to identify hadrons up to high momenta. Furthermore, there will be two electromagnetic calorimeters allowing also photon detection, namely EMCAL and PHOS.

This setup is complemented by a set of forward detectors and a muon arm with an additional bending magnet for the detection and tracking of muons at forward rapidities. The muon detectors are installed behind an absorber.

The CERN and ALICE infrastructures, such as network and storage, are designed for a recording rate of 100 Hz for PbPb minimum bias events. Since the hadronic interaction rate will be much higher, interesting events must be selected on an on-line basis. This decision is made by a multi-level trigger system. It activates the required detectors and decides at several stages whether the acquisition should be continued or aborted.

As mentioned above ALICE is designed for the study of heavy-ion collisions. The other LHC experiments are mainly interested in cleaner pp collisions for the study of fundamental interactions. It is now planned to have one month per year of heavy-ion running while the rest of the annual run period will be used for pp runs. ALICE will also participate in the pp runs which are needed as reference data for the analysis of the heavy-ion data, but will also be subject to specific analysis.

1.4 The Transition Radiation Detector

For the previously mentioned studies on the QGP, such as of di-leptons, it is important to have tracks of well-identified electrons. These can be used for the reconstruction of mesons with leptonic decay channels, e. g. $J/\Psi \rightarrow e^+e^-$.

Due to the low mass the behaviour of the electron is relativistic even at low momenta. This is used for e/π -separation by dE/dx measurements. The TRD uses

²This pseudo-rapidity range corresponds to a polar angle of 45° to the beam axis.

the effect of transition radiation, i. e. the emission of photons by highly relativistic charged particles traversing medium boundaries with different refractive indices. Within the relevant momentum ranges this process only occurs for electrons. By the detection of this transition radiation a probability for a particle to be an electron can be calculated.

The TRD is included in the global central barrel tracking which uses the information from ITS, TPC and TRD. The main part of the tracks is within the TPC from where they are matched and propagated to the ITS — to achieve a high vertex resolution — and to the TRD and TOF — to enlarge the lever arm for the momentum measurement and to use the PID information. Within this tracking scheme the PID information is calculated from the measurements in different detectors. It includes the dE/dx measurements in the TPC, the TRD electron identification by dE/dx as well as transition radiation and the TOF signal.

Besides the ability of global tracking based on recorded data (off-line processing) the TRD allows a very fast standalone tracking on-line. This opens the possibility of an L1 trigger based on tracks with available PID information. This can be used for a trigger on single or di-electrons. Also, a trigger on jets is foreseen.

1.5 Commissioning and Start-Up

The LHC experiments are long-term projects which have been proposed in the 1990s. During the time of this thesis both the accelerator and the detectors reached the phase of commissioning after a long planning and construction period. This means bringing all the detectors and subsystems into operation within the global ALICE system and making them ready for common data taking in global runs.

This commissioning is still on-going and includes cosmic runs with many subdetectors participating. The cosmic particles are used for the testing and calibration of the detectors and the reconstruction software.

During the integration of the subdetectors many challenges were faced. It is necessary to have fast diagnostic and debugging tools ready in order to localize problems within the complex global system.

In section 2 an overview of the Transition Radiation Detector is given. The two subsequent sections describe the testing and installation of the detector at the experimental site and its commissioning to achieve first data taking. Section 5 describes the on-line tracking simulation framework for the TRD trigger system in order to study the trigger efficiency, purity and biases on the basis of simulated and real data. In section 6, a possible implementation of a jet trigger based on the TRD is sketched.

2 The Transition Radiation Detector

This chapter gives an overview of the fundamental principles of particle detection, tracking and electron identification in the Transition Radiation Detector (TRD) as well as its design and integration into ALICE.

2.1 Principle of Operation

The goal of the TRD is adding electron identification and tracking capabilities to the central barrel of ALICE allowing e/π -separation up to high momenta. The matching of the track segments of the central barrel detectors is required to combine all information for the reconstructed tracks. With the TRD extending the lever arm of the tracks it contributes to a more precise p_T -measurement based on the trajectory curvature in the magnetic field. The TRD is planned to cover the full acceptance of the central barrel, i. e. $\eta = \pm 0.9$ and the full azimuthal angle.

The aimed π -rejection by a factor 100 at high transverse momenta is neither amenable to the dE/dx measurements in the TPC nor the time of flight measurements in TOF nor the Cherenkov separation in the HMPID. As unique signature for electrons the production of transition radiation is used: A charged particle traversing a boundary between media of different refractive indices can radiate (though with low probability) a photon. This relativistic effect strongly depends on $\gamma = \frac{E}{m}$ and is only relevant for $\gamma \gtrsim 1000$. Such a high relativisticity occurs only for electrons within the relevant momentum range. The photons produced are predominantly in the X-ray range (s. Fig. 4). The detection and recognition of this transition radiation is used for the identification of an electron.

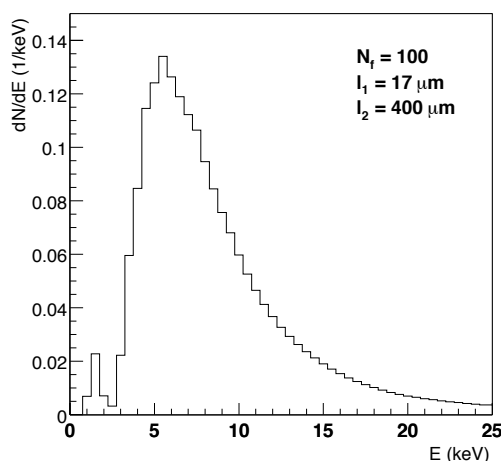


Figure 4: Calculated energy spectrum of the produced transition radiation in 100 foils of $17 \mu\text{m}$ thickness with gaps of $400 \mu\text{m}$. The photons are in the X-ray range. [14]

Due to the low probability of transition radiation emission many boundaries are

needed. This is achieved by the use of a special radiator consisting of a combination of polypropylene fibres and foam. The thickness of the radiator is limited by the necessity of intermediate tracking devices — needed for track matching at high multiplicities. This determines the structure of the TRD consisting of six layers, each comprising a radiator and a tracking chamber. For the detection of the transition radiation the tracking chamber is used as well, which requires the efficient detection of X-ray photons.

The above considerations show that a large area has to be covered with tracking devices, favouring the use of gas detectors. They are fundamentally based on the ionisation of the gas by traversing charged particles. An appropriate gas with a high photoabsorption cross section allows the simultaneous detection of the transition radiation photons. The ionisation clusters are detected in a Multi-Wire Proportional Chamber (MWPC). Since such a chamber by itself acquires only position information and has no local tracking capabilities, it is preceded by a drift chamber. Thus, a trajectory of a charged particle can be detected as a local track segment within an individual chamber instead of only a crossing point. This allows a precise matching of the segments across layers which is non-trivial in case of high multiplicities. The resulting structure of a TRD chamber is shown in Fig. 5.

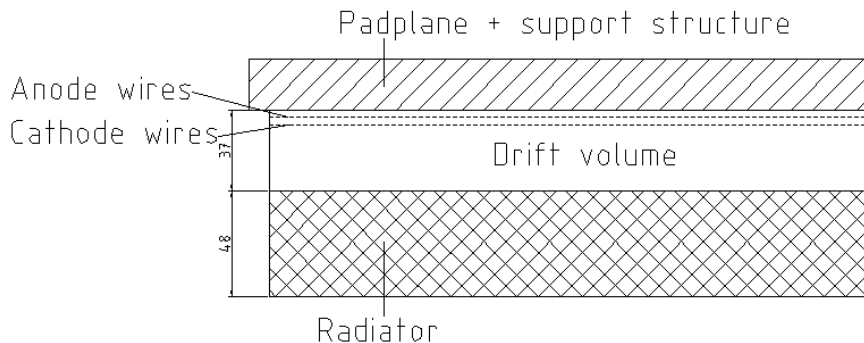


Figure 5: The cross-section shows the radiator (pointing to the interaction vertex) followed by the tracking chamber. It consists of a gas-filled volume in which an electric field is generated by the application of voltage between the surface of the radiator and the cathode wire plane. The anode wires are required to achieve gas amplification such that detectable signals on the pad plane are produced. All dimensions are given in mm.

A charged particle reaching the TRD from the interaction point first passes through the radiator. Subsequently, in the drift chamber, it deposits energy by ionising the gas. This results in clusters of electrons and ions. If an electron emitted transition radiation in the radiator, the absorption of the photon leads to additional ionisation at the entrance of the drift chamber (s. Fig. 6). By applying a voltage between the chamber panels an electric field is generated resulting in the drift of the freed charges within the filling gas. The electrons move in the positive x -direction —

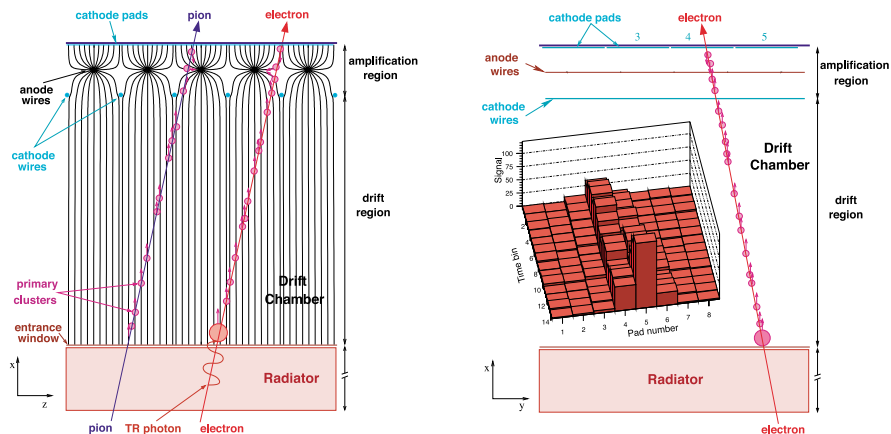


Figure 6: The left figure shows the passage of a pion/electron through a TRD chamber. Along the trajectory clusters of electrons are produced which drift in the electric field towards the amplification region. In the case of an electron the absorption of the transition radiation photon leads to a bigger cluster close to the radiator. The right figure shows the signal as detected on the pad plane due to the amplification of the primary electrons. [14]

the ions in negative x -direction — and finally reach the amplification region where avalanches are created in the vicinity of the thin anode wires supplied with positive high voltage — by repeated collisions of the electrons gaining energy in the electric field.

The movement of the created charges in the electric field around the anode wires leads to a detectable signal on the anode wires and the cathode plane as in any MWPC. By segmenting the cathode plane into pads, the position of a charge cluster can be measured (s. Fig. 8). The pad width (~ 8 mm) is chosen such that a single cluster leads to a charge shared between 2-3 adjacent pads. Then, the position can be determined to the sub-pad resolution from the center of gravity of the charges. In z -direction the pads are much longer (~ 8 cm). To increase the z -resolution to be better than the mere pads size, the pads of neighbouring layers are tilted by $\beta_{\text{tilt}} = 2^\circ$ in opposite direction. By this correlation of the two directions tracks can be reconstructed with an increased z -resolution — on the cost of a slight deterioration of the y -resolution.

The signal on the pad plane (and on the anode wire) is mainly due to the ion drift³ which is significantly slower than the electron drift. This results in a signal that is characterised by a sharp rising edge and a long tail. The tail has to be treated specially since it can overlap with the signal of subsequent clusters and thus lead to a deterioration of the resolution.

³The ions move through the higher difference in potential.

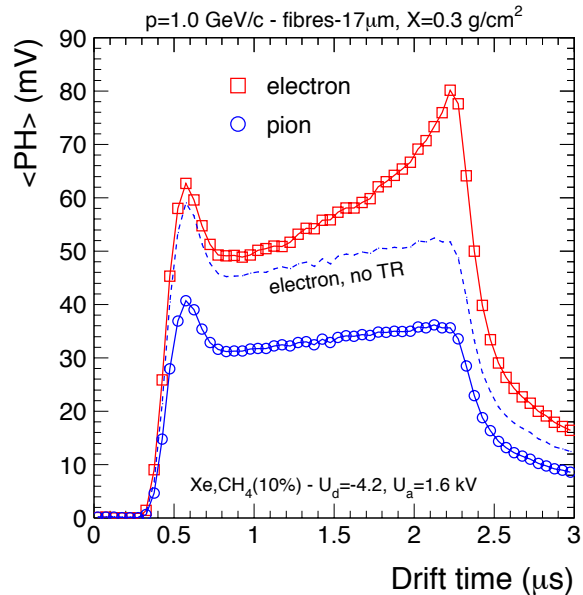


Figure 7: This plot shows the average pulse height evolution with drift time. The absorption of the transition radiation photon leads to a peak in the end of the pulse. [14]

The response of the detector can be characterised by so-called response functions. The pad response function $PRF(y)$ specifies the charge induced on a pad by a point-like cluster with y -coordinate y measured in units of the pad width. The time response function describes the temporal signal on the pad (relevant due to the long tail). Assuming a linear behaviour of the detector the total response can be calculated by the convolution of the response functions with the cluster shape.

The trajectory of a particle is reconstructed from its clusters, whereby the position of each cluster is determined from the drift time (x) and the charge distribution on the pads (y). Fig. 7 shows the pulse height evolution along the drift-time of the clusters from a traversing particle with the parameters as given in the figure. The signal of a pion shows a peak in the beginning which is caused by clusters from two sides of the anode wires in the amplification region. The plateau extends over the full drift-time. An electron signal differs in the deposited energy and the transition radiation photon which leads to a peak at the end of the drift-time (corresponding to the entrance of the drift volume).

2.2 Overall structure

The layered structure of the TRD is driven by the need for significant transition radiation production. The overall structure follows the ALICE-wide 18-fold azimuthal segmentation with the entities of supermodules for each sector (s. Fig. 9). Each supermodule contains 5 stacks (in z -direction) of 6 layers each (s. Fig. 10). The

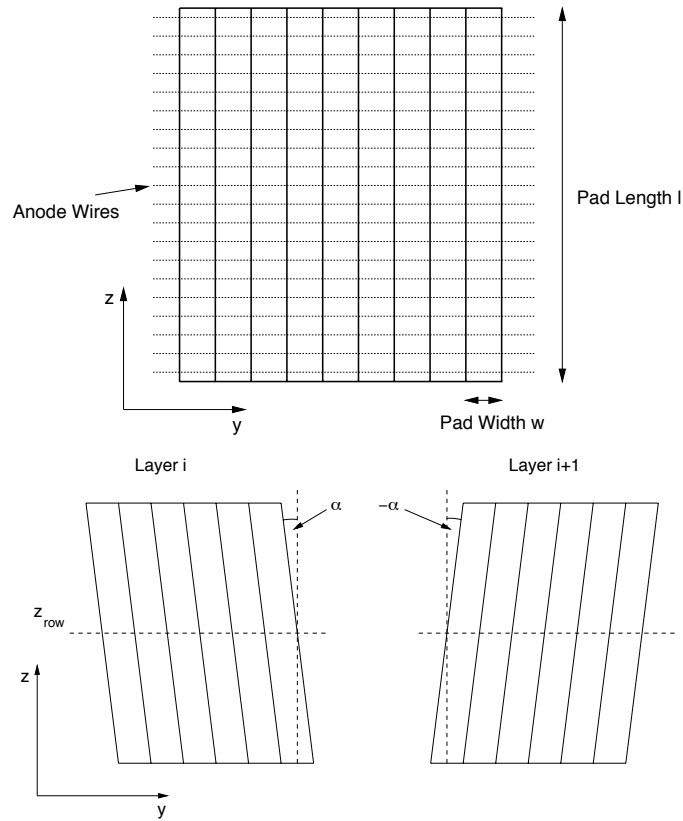


Figure 8: The top figure shows the pad plane as seen from top. The lower figure shows the tilting of the pads in different orientation in neighbouring layers by an angle of $\beta_{\text{tilt}} = 2^\circ$. This leads to an improvement of the z -position resolution. [14]

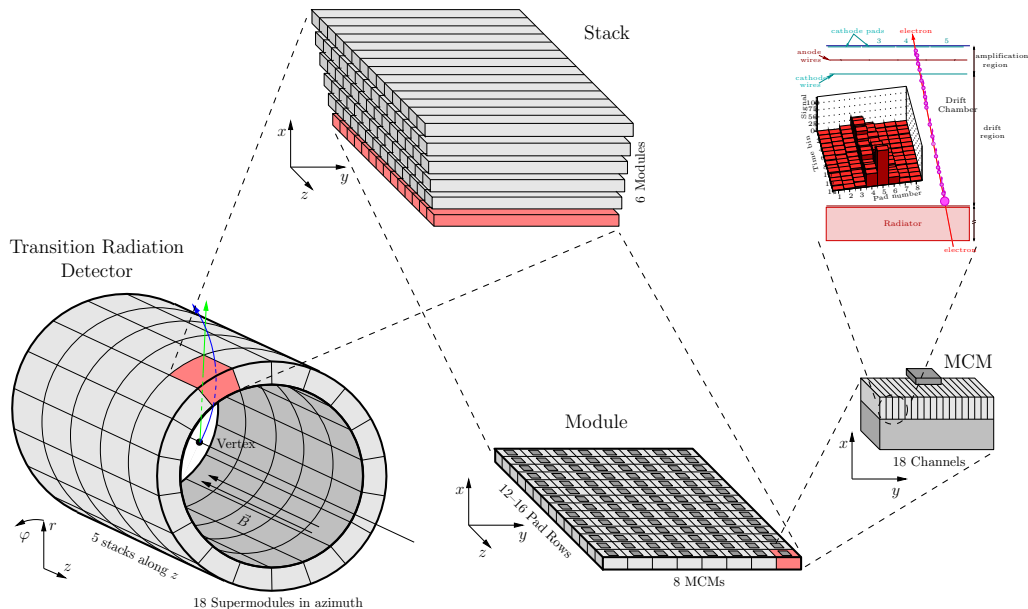


Figure 9: The full TRD consists of 18 supermodules. Each contains 5 stacks of 6 chambers. The chamber-mounted electronics performs the readout and the local tracking [17].

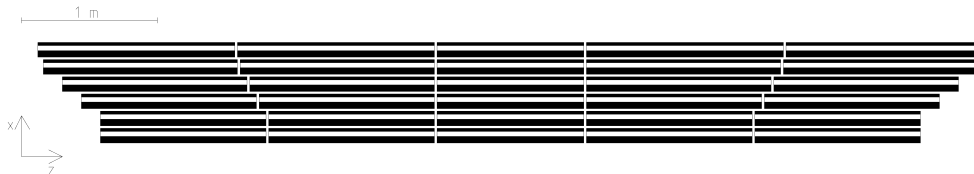


Figure 10: The structure of a TRD supermodule with 30 individual chambers. The total length is about 7 m.

chamber dimensions are given by a compromise of the coverage of a certain pseudorapidity interval and the number of different chambers to be constructed. These considerations affect the TRD trigger capabilities because the on-line tracking is performed only stack-wise.

The supermodules are placed in the spaceframe of ALICE adjacent to the TPC. The lower ones will not contain chambers in the middle stack (mid-rapidity) in order to reduce the material budget in front of the PHOS detector (s. Fig. 3).

2.3 Front-End Electronics

The pad plane signal generated as described above is extremely small ($\approx 10^5$ electrons for a minimum ionising particle). To avoid the deterioration of the signal by additional noise from the capacitance of cables, the registration of these signals is

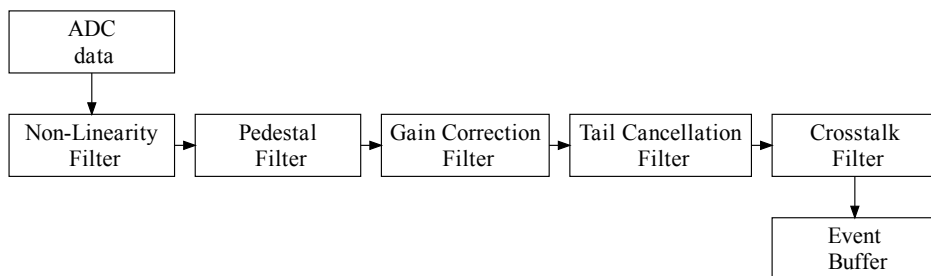


Figure 11: The digitized data from the PASA is passed through several filter stages which can be individually configured or bypassed. The output is stored in the event buffer for further readout and passed to the preprocessor for immediate analysis.

done as close as possible to the pad plane by the front-end electronics. Groups of 18 pads within a row are connected by short cables to a Multi-Chip Module (MCM) on the back-side of the chamber. This module comprises the Pre-Amplifier and Shaper Amplifier (PASA) and the Tracklet Processor (TRAP).

The pad charges are registered on the PASA individually. The PASA contains several amplification stages and converts the input signal to a voltage on a pedestal value. Additionally, the signal is shaped to cancel the long ion tail.

The PASA output voltages are converted to digital values by ADCs in the TRAP. The sampling rate is 10 MHz and the signal is digitized with 10 bits resolution. In addition to the PASA channels from the same MCM one or two channels from the PASA in the left or right MCM, respectively, are included. This sharing, leading to 21 ADC channels per MCM, is needed for the on-chip tracklet calculation (s. section 5.2).

The digitized data is processed in a series of digital filters [6]. This is necessary at this stage since the trigger calculation is based on this information:

Non-linearity: This stage allows the correction of non-linearities in the amplification and/or electronics, realized by a lookup table (LUT) with 64 entries:

$$O(t) = I(t) \cdot 4 + \text{LUT}_{\text{NL}} \left(\frac{I(t)}{16} \right)$$

where $I(t)$ and $O(t)$ denote the input and output values, respectively, of the filter stage⁴. Besides the correction for non-linearities two bits are added to avoid rounding errors during the further calculations. The use of a lookup table results in a high flexibility for the correction.

⁴The same notation is used for all filter stages described here.

Pedestal: For the analysis the signal on top of the low-frequency baseline is relevant. In this stage the signal is adjusted to a common (adjustable) pedestal value P :

$$O(t) = I(t) - P(t) + P$$

where the subtracted value $P(t)$ is calculated in a relaxation process with parameter β :

$$\begin{aligned} P'(t+1) &= P'(t) + (I(t) - \beta \cdot P'(t)) \\ P(t) &= \beta \cdot P'(t) \end{aligned}$$

Gain correction: To account for channel-wise differences in the gas gain and electronic amplification, a correction γ of $\pm 12\%$ can be applied:

$$O(t) = \gamma_n \cdot I(t) + \rho_n$$

where n indicates the channel. Additionally, ρ_n allows to correct scaling related baseline shifts.

Tail cancellation: This stage cancels the long tail of the signal due to the slow ion drift. The tail is approximated by the sum of two exponentials:

$$S(t) = 1_{(t \geq 0)} \cdot (\alpha_L \lambda_L^t + (1 - \alpha_L) \lambda_S \lambda_S^t)$$

This signal is subtracted from the original signal.

Crosstalk filter: The crosstalk filter allows to correct for correlations between the signals of neighbouring channels. So far, there seems to be no need for this filter.

As these filters contain adjustable parameters, they require an appropriate configuration. Alternatively, the filters can be bypassed by configuration settings. The output of these filter stages is fed into an event buffer (up to 64 ADC values per channel) used for the further readout. In parallel, the data is fed to the preprocessor.

The adjustment of the above mentioned filters is crucial. The filtering cannot be done after the data taking since the corrected values are needed for the on-chip analysis, i. e. the cluster finding in the preprocessor. The filters strongly influence the quality of the found clusters with respect to position resolution and accumulated charge (which is needed for the PID calculation).

The clusters found by the preprocessor are used by the tracklet processor to apply a straight line fit and produce tracklets — track segments within one chamber. The tracklet calculation is described in more detail in section 5.2. The processing in one TRAP is shared between four CPUs in parallel which can have a different instruction set and operate on different data (MIMD: Multiple Instruction Multiple Data). The specific instructions for the processing are freely configurable.

Besides the tracklet calculation, the TRAP controls the raw data readout. Due to the large number of TRAPs on a chamber the data is not read out in a parallel fashion but serialized on the level of half-chambers. For this procedure the so-called network interface of the TRAPs is used. It allows the data transfer between different chips. In the readout process, first, the tracklets and, then, the raw data are transferred. On each half-chamber a dedicated Optical Readout Interface board (ORI) transmits the data via an optical fibre to the Global Tracking Unit (GTU) where they are further processed and forwarded to the Data Acquisition (DAQ) system.

Besides the network interface used for the data readout, the TRAPs have a Slow Control Serial Network (SCSN) interface used for their configuration and programming. This structure is based on a bus system organized in two daisy-chained rings per two Readout Boards (ROB) with opposite chain direction to achieve a redundant system which is still operational in case of a broken MCM. The SCSN protocol contains frames that have to be generated by a master. These frames are then transferred from one MCM to the next while each MCM can take an action if it finds itself addressed or just forward the frame. In any case a hop counter in the frame is increased. After being transferred through the complete ring the frame is received by the master again. This bus is accessible from the DCS boards.

2.4 DCS Board

For the control of the detector electronics a special Detector Control System (DCS) board is installed on every chamber as the single interface to the outside world besides the mono-directional readout connection. This board hosts an Altera EPXA1, comprising an ARM processor and a FPGA, the trigger interface TTCrx, ADCs and flash memory. The processor is used to run a specialized version of the Linux operating system and the FPGA is used to implement the required interface logic, such as Ethernet, JTAG⁵ and SCSN (Slow Control Serial Network). This allows a great flexibility in the use of the DCS board. On the other hand, it provides a standard interface for the operation, i. e. it can be controlled remotely by Linux commands in a secure shell session.

For the TRD a special firmware containing both the FPGA design and the software part including the Bootloader, the kernel, the root file system and the environment settings, is loaded. This contains a minimal software configuration which can be extended by further specialized tools for the control of the detector. These packages are managed and installed by the package management system `ipkg`⁶. One of these packages is the so-called `libTRD` which contains the tools necessary for the interaction with the chamber. The functions are implemented as library routines (so that they can be used in other programs). Additionally, a command-line interface

⁵Joint Test Action Group: A standardized protocol for low-level access to integrated circuits.

⁶The Itsy Package Management System

is provided for standalone use from a shell session during low-level checks.

One major task of the DCS board is the configuration of the front-end electronics. This is done via the SCSN for which an interface is also implemented in the libTRD. Either individual MCMs can be addressed as done for the upload of chip-specific configuration settings or broadcast commands can be issued, e. g. for the instruction upload.

Since it is not feasible to control each DCS board (540 for all TRD chambers) individually by shell commands an automizable interface is needed. Each DCS board runs a FEE-server (Front-End Electronics-server), a program which acts as a server with respect to the DIM⁷ protocol. This server publishes data values, such as the current state of the chamber and its temperature, and accepts commands on different DIM communication channels. The published information can be easily retrieved from other DIM-based programs running on the DCS machines. The command channel of this FEE-server is used to receive the configuration command including the full instruction list for the MCMs.

2.5 Readout scheme

Being a trigger detector, the TRD has to transfer data at two stages: The tracklets have to be read out for the trigger decisions where latency considerations are extremely important. The raw data has to be fully readout in case the event was accepted by the Central Trigger Processor. The same readout interfaces are used for the readout of the trigger information and the raw data.

The readout follows a tree-like structure with the following aspects being valid for both the tracklet and raw data readout. The information accumulated on each MCM is locally stored (in FIFOs). Each MCM then sends its information to its corresponding column-merger (within the ROB), s. Fig. 12. The mergers ensure the data output according to a configured readout order. The end of data of individual MCMs is indicated by the sending of special endmarkers. The column merger locally caches the incoming information and sends it to the Board Merger, which acts in the same way as the column merger but on a higher level. Each readout board has one Board Merger. The next level is the half-chamber merger which collects the data from the Board Mergers of the four (three in stack 2) Readout-Boards. At this level the half-chamber merger holds the full information of a half-chamber and forwards it to the optical readout interface (ORI). This communication utilizes the TRAP network interface.

From there the data is shipped to the GTU via optical fibres. The GTU contains Track Matching Units (TMU) each of which accepts the optical input from the 12 half-chambers of a stack. Each unit hosts an FPGA for the processing of the arriving data. The tracklets are used as basis of a fast tracking algorithm combining tracklets to longer tracks (s. section 5.1). These tracks shall be used for a trigger

⁷Distributed Information Management

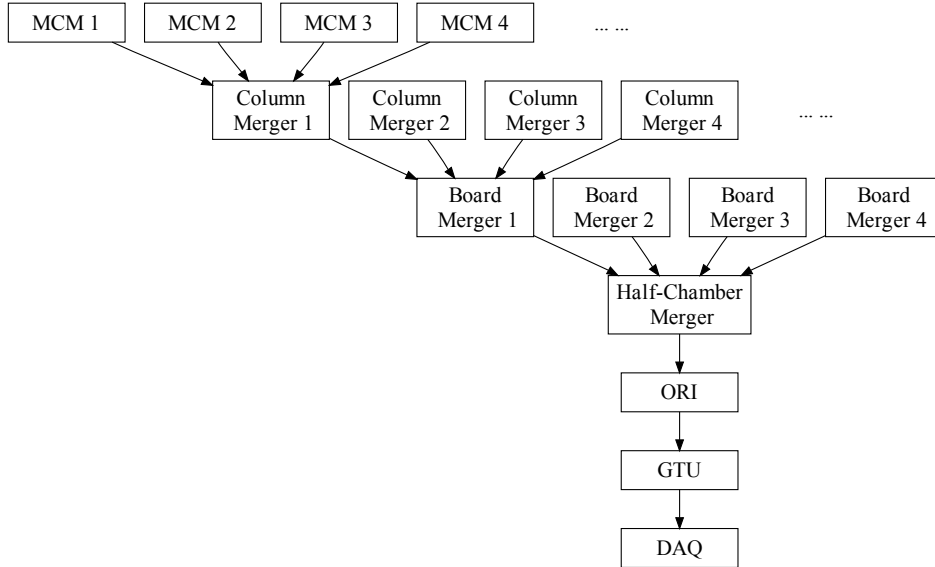


Figure 12: This figure shows how the data from all MCMs is merged and finally transferred to the data acquisition system. The dots indicate that all mergers have the same structure lower in hierarchy as the first ones.

decision at the L1 time. One SuperModule Unit (SMU) merges the tracks of all stacks of a supermodule and produces a trigger contribution from them. The arriving raw data from the supermodule is buffered and (in case of a trigger accept) sent to the Data Acquisition system. This transfer over Detector Data Links (DDL) [15] is controlled by the SMU.

2.6 Services

As discussed before the TRD is organized in chambers, each of which has to be supplied with electrical power, cooling, gas and the communication interface connections.

The DCS boards have individual power connections which can be switched separately. This is realized by a dedicated Power Distribution Box (PDB) in each supermodule. It is connected to one power supply channel with the required voltage from there the individual DCS boards are supplied by switchable lines.

For the switching operation of the channels another interface unit (outside of the supermodule), the Power Control Unit (PCU), is used. It hosts a DCS board accessible via Ethernet. From there the PDB is controlled via a special serial protocol. The communication to the PCU is realized via DIM.

The DCS boards also need an Ethernet connection to be accessible. For this patch-panels are installed in the front-panels of the supermodule. Adaptor cards allow to use one standard Ethernet cable with 4 twisted pairs for two DCS boards

(since they host 10 Mb/s interfaces only using two pairs of cables).

The DCS board components have a JTAG interface which allows their programming. Additionally, the FPGA fabric holds JTAG master implementations which allow to build a JTAG loop within the supermodule by connecting the master port of each DCS board to the slave port of the next one. This gives in-situ programming capabilities to the DCS board in case of problems in the Ethernet connections.

Since the DCS boards can be used for the control on the chamber level, the other connections are not individual. Instead the low-voltage supplies are grouped for pairs of two layers and distributed via power bus bars running along the side of the supermodule. The readout boards are connected to the power bus bars. The voltage regulators on the readout boards providing the supplies for the MCMs are controllable from the DCS board. The lack of direct connections facilitates the power distribution since each readout board requires multiple voltages for different parts of the electronics. The digital and analog parts of the circuits are separated for noise reduction.

From each chamber two optical fibres for the readout are connected to a patch-panel that can be accessed from outside.

The gas connections to the chamber are also grouped in pairs of layers reducing the number of necessary connections.

The cooling of the electronics is achieved by cooling panels on the MCMs and lines in φ -direction, which are supplied from cooling bars installed next to the Power Bus Bars. The water-cooling is operated at under-pressure.

2.7 Trigger

Usually the interaction rate in particle or heavy-ion physics experiments is much higher than the feasible rate of data acquisition. Therefore a trigger system is needed to decide in which cases a measurement should be started and eventually read out. For ALICE a multi-level trigger scheme is used.

The Level-0 (L0) trigger effects the initial activation of the detectors. This trigger is issued by the Central Trigger Processor (CTP) based on the fulfilment of conditions of its L0 inputs. The detectors contributing such an input are fast detectors which do not need a startup signal and are continuously sensitive to new physics events. The L0 trigger is sent to the involved detectors (the set can depend on which L0 inputs actually fired) and initiates the local data recording on the affected detectors.

The next stage is the Level-1 trigger which can follow any L0. If it is not issued the event is aborted and the electronics has to become ready for the next L0. The time interval between L0 and L1 should be short to reduce the time during which no other L0 can be issued. The inputs on which the L1 trigger is based have to be contributed about 6 μ s after the L0. The decision is based on the information acquired after the L0 trigger. In the case of the TRD, the MCMs start the tracklet calculation with the L0 and send them to the GTU where tracks are calculated.

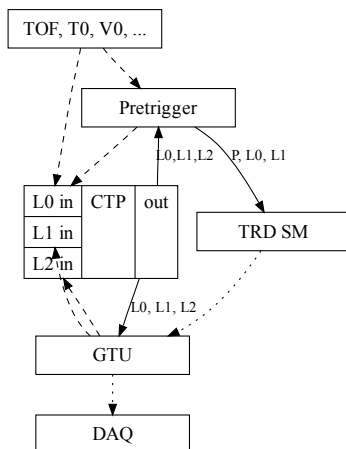


Figure 13: The signal from fast detectors, such as TOF, V0 and T0, is split to the CTP and the TRD pretrigger system. The latter produces a wakeup signal for the TRD electronics and sends a L0 contribution to the CTP itself. The later triggers issued from the CTP are forwarded to the supermodule.

Based on these tracks the GTU can send a L1 contribution to the CTP. If the TRD receives a L1 trigger (not necessarily due to its own contribution) the raw data readout to the GTU is started where the data is buffered for subsequent readout in case of a L2 accept.

The L2 trigger is issued about $100 \mu\text{s}$ after the L0 — this time is determined by the TPC drift time. It can be based on more involved calculations for which the L0-L1 time is not sufficient or the data is not even sampled. A L2 accept causes the shipping of the data to the DAQ whereas in case of a L2 reject the data are discarded.

For the TRD the situation is more complicated because the L0 trigger is too late after the interaction to see the full signal of the drift chamber. Since the TRAP chip is put into a sleep mode for power-saving and noise reduction, the pretrigger is needed as wake-up signal for the electronics prior to the L0. This signal is issued by the pretrigger system based on the input from the fast detectors contributing a L0 but without the additional latency of the intermediate CTP — the pretrigger system is installed inside the magnet. In the optimal case the same trigger condition as in the CTP is achieved and every L0 trigger is preceded by a pretrigger pulse.

This leads to a special scheme of trigger distribution for the TRD. The supermodules are not directly linked to the Central Trigger Processor but are connected to the Pretrigger system. This system has inputs for the fast detectors and is connected to the CTP. It is responsible for the generation of the wake-up signal for the TRD and the forwarding of the CTP L0/L1 signals if they are issued.

The trigger signals from the CTP are distributed via optical fibres using the

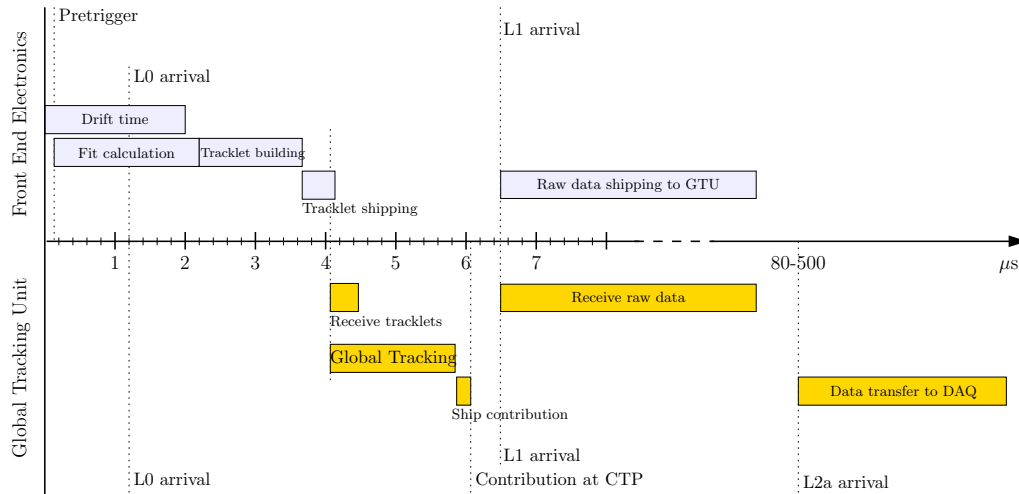


Figure 14: Time sequence diagram for trigger and data transfer of the TRD, adapted from [21].

LHC-wide TTC protocol [35]. Not only trigger pulses but also interaction IDs and the trigger class are transmitted. Such TTC connections are also used between the pretrigger system and the supermodules. The trigger contributions to the CTP are electrical LVDS signals.

2.8 Status

During the 2008 run 4 out of 18 supermodules were installed. The supermodules are numbered by a serial number (in roman numerals) reflecting the production order. Fig. 15 shows the position of the installed supermodules. The following installations are planned to symmetrically fill the positions from the horizontal positions. The completion of the TRD with the full acceptance is planned for the shutdown period of 2009.

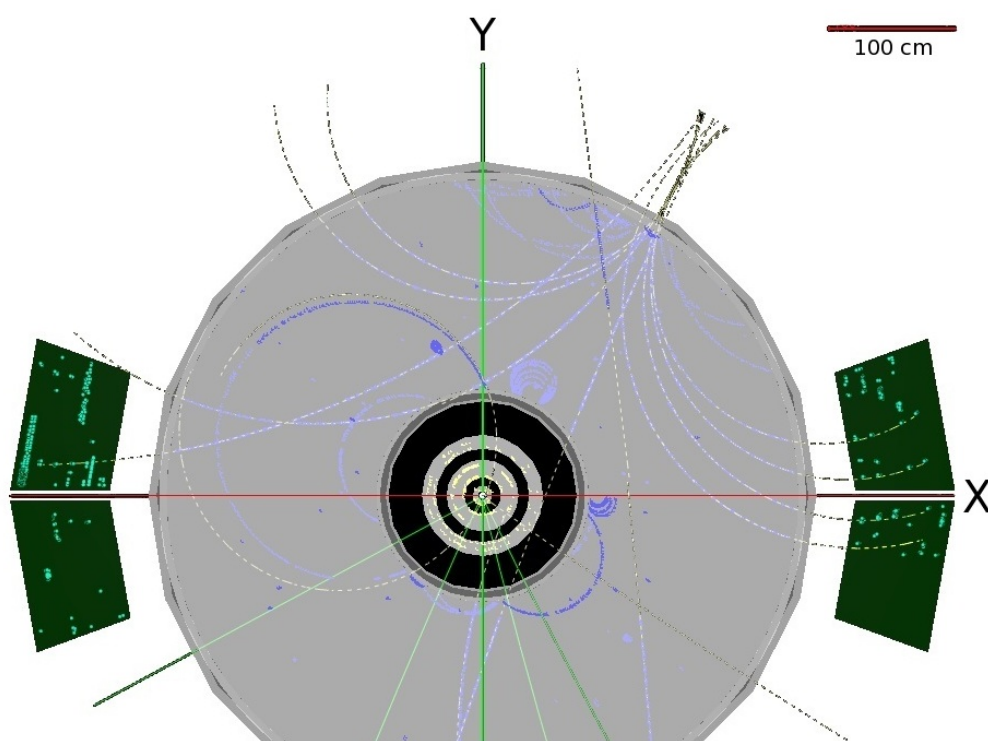


Figure 15: During the 2008 run the 4 TRD Supermodules were installed in the horizontal position. View along the beam axis.

3 Surface testing

As was discussed in the previous section, the TRD is a large-scale detector which relies on the mass production of its components. This requires means of quality assurance to guarantee a fully operational detector system.

The assembly of the chambers is done in several sites: GSI (Darmstadt), Heidelberg, Dubna, Bukarest and Frankfurt. Here they are already tested with respect to gas tightness and high voltage stability. The integration of the Front-End Electronics is done in GSI (Darmstadt) and Frankfurt where the electronic operation is also tested. When the chambers are fully equipped and tested they are transported to Münster where the supermodule integration takes place. This includes the assembly of the supermodule hull and structure as well as the installation of the chambers. The completed supermodules are then transported from Münster to CERN for their final installation.

This leads to a need for testing also at CERN to ensure that the detector is working before its installation. During the assembly and transport of a supermodule, it is carried by a special steel support structure, the so-called blue-frame, which guarantees the mechanical stability. At CERN the supermodule is moved into a rotator, a steel structure holding the supermodule as in the spaceframe. It provides the possibility to turn the supermodule along its z -axis. This allows the testing of the supermodule in the final orientation. The supermodule in the rotator is moved to a cleanroom, next to the shaft to the cavern hosting the experiment. Here, extensive tests can be performed with a minimum of interventions between the tests and the final installation.

The careful checks prior to the installation are very important since severe problems inside a supermodule, found after the installation, are difficult to resolve due to the limited access. They may require the uninstallation of the full supermodule.

The rotator is also used for the installation when the supermodule has to be pulled into the spaceframe in the proper orientation.

3.1 Testing setup

The cleanroom is equipped with all the necessary infrastructure for the operation and testing of a supermodule as well as for its repair. The conditions of the supermodule during the tests should be as similar as possible to the final installation. In the following, the necessary systems for the operation of the supermodule, summarized as services, are shortly described. An overview of the connections is shown in Fig. 16.

Low Voltage: For the electrical supply a set of power supply units of the same type as in the experimental cavern (Wiener PL 512) are installed in a rack. They provide enough power for the operation of all DCS boards and the read-out electronics on up to 12 chambers. The required voltages and typical currents

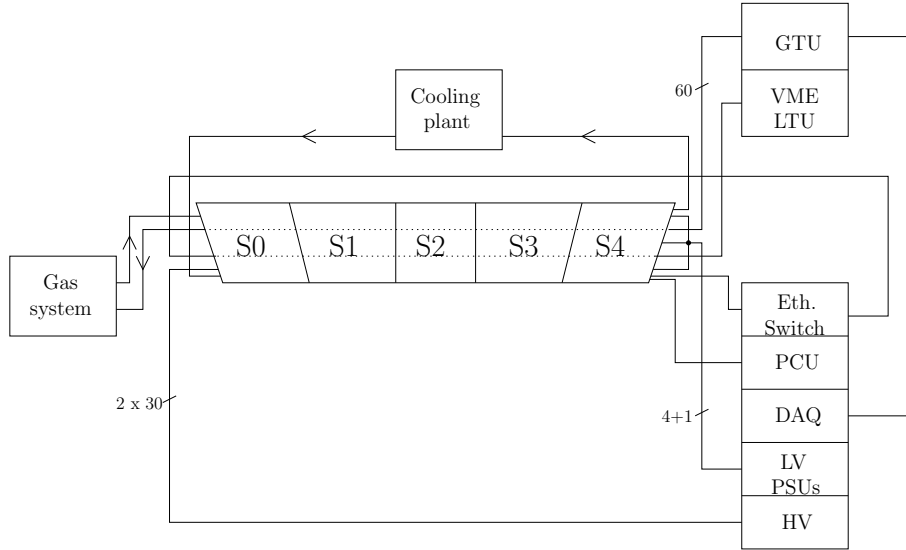


Figure 16: Overview of the connections to the supermodule in the cleanroom.

Channel	Voltage	Usage	Current
A3V3	4.0 V	PASA	110 A
A1V8	2.5 V	ADC	125 A
D1V8	2.5 V	TRAP	90 A
D3V3	4.0 V	TRAP	40 A
DCS	4.0 V	DCS boards	30 A

Table 2: The low voltage channels are used for a double-layer, i. e. 10 chambers. The currents are meant as rough reference for typical operation but might be different depending on the rate. The D3V3 channel is normally used for a full supermodule.

are shown in Table 2. The power supplies are operated via SNMP-commands over their Ethernet interface.

Cooling: For the long term operation of the supermodule cooling is necessary. It is provided by a cooling plant operated at underpressure, i. e. the cooling circuit is evacuated and the pressure difference between inlet and outlet is adjusted such that no overpressure occurs at any position.

Ethernet: As within all of ALICE, Ethernet is the main communication interface to the supermodule by the DCS board. The MAC address of each DCS board encodes its serial number allowing the identification of the DCS board. With the information from the so-called GateDB, a database containing the information about the installation position of the DCS board within the supermodules, a DHCP- and Nameserver is fed; thus, the DCS boards automatically retrieve their IP address and hostname from which they derive the position of their installation. The network is separated from the General Public Network at CERN and provides the same structure as in the final experiment.

High Voltage: The high voltage required for the operation of the TRD chambers is provided chamber-wise. For this purpose special HV-modules (Iseg) are used providing the necessary number of channels. These modules are hosted in a crate and can be controlled from a PC via their CAN-bus interface. For the tests a simple tool has been used to set the voltages on individual channels and measure the currents.

Gas: The operation of the detector requires to flush the drift chambers with a suitable gas. Since a mixture of Xe/CO₂ has to be used for the transition radiation detection — Xenon being very expensive — the tightness of the system is crucial. The extensive tests use Ar/CO₂ as it is much cheaper. The gas system in the cleanroom provides several independent lines of gas flow for tests in parallel. This is necessary since they are very time-consuming.

Trigger: A VME crate hosts the modules necessary to send triggers to the supermodule. This includes a Crate PC, a Local Trigger Unit (LTU), TTC modules for the encoding of the signal and the optical output (TTCvi and TTCex) [35].

Monitoring and Control: For the monitoring and control of the supermodule several PCs and virtual machines are used. They run the administrative network services such as DHCP, DNS and DIM-DNS. The latter is used for the registration of DIM-servers, such as the FEE-server on the DCS board. Furthermore, the tools for the configuration of the Front-End electronics, such as the configuration database and the InterComLayer, are hosted on these machines.

Power Control Unit: For the control of the Power Distribution Box a Power Control Unit is needed. It switches the power to individual DCS boards.

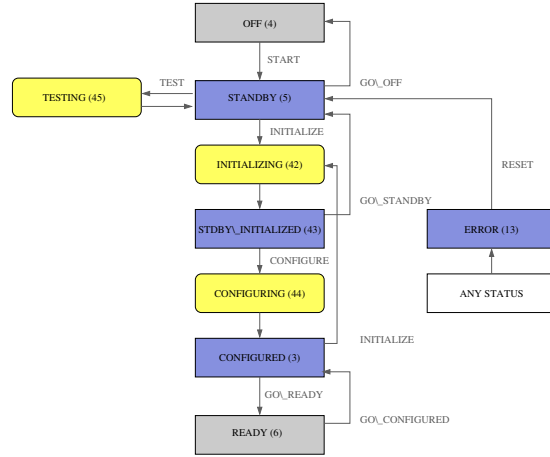


Figure 17: Front-End Electronics finite state machine diagram [36]

GTU and DAQ: For the data readout a GTU segment for a full supermodule is available. A dedicated PC runs the DAQ software to receive the data via the Detector Data Link (DDL) from the GTU.

3.2 Testing procedure

This section describes the various tests that are performed on the supermodule. The procedure consists of many steps and is not always linear since parts of it are relatively independent of each other. Especially, in case of problems deviations from the described sequence are unavoidable.

After the arrival of the supermodule in the cleanroom, the first step is to establish the essential connections for the operation of the supermodule. When the low voltage for the Power Distribution Box (PDB) and the PCU-PDB line are connected the DCS boards can be powered. For communication the Ethernet connections are necessary. The network settings (DHCP, nameserver etc.) emulate the circumstances in the final setup. If everything is working, the DCS boards boot and retrieve the necessary information from the DHCP server. From then on the DCS boards are accessible via Ethernet and provide further access to the chamber.

3.2.1 Detector Control System Board

If the booting of the DCS board was successful the FEE-server, a special DIM server for the interaction with the chamber, starts automatically. This server publishes status information as DIM services comprising the current state of the chamber within the state diagram (Fig. 17) as well as the temperature on the chamber surface and the voltages sensed at the power bus bars. The information available via DIM can be monitored by a set of tools continuously retrieving the published values.

Test	Description
DCS board	The first step is to power the DCS boards and establish the Ethernet connection. This is needed for the subsequent tests.
Front-End Electronics	The functionality of the readout electronics is tested and the access to the configuration bus is verified.
Cooling	The effectiveness of all cooling lines is checked by temperature measurements on the readout boards.
Gas	The tightness of the complete gas system is checked. This test takes ≥ 48 h.
High Voltage	The proper connections of the high voltage are tested and checked for leak currents.
Stress Test	The long term stability of the readout electronics is tested.
JTAG	The low-level access to the DCS boards is tested which might be needed in case of problems in the higher level access.

Table 3: Overview of tests done in the cleanroom

3.2.2 Front-end electronics

With the DCS boards providing the control over the chamber electronics and the relevant low voltage lines connected, the tests of the Front-End Electronics can be started. The first step is to switch on the readout boards. This action is normally performed by the FEE-server which represents the status of the electronics to the higher control levels by the implementation of a finite state machine (FSM, s. Fig. 17). The current state is published as DIM service and the transitions can be triggered by DIM commands. The above mentioned powering of the readout boards corresponds to the transition from `STANDBY` to `STANDBY_INITIALIZED` in which the MCMs are also initialized by a set of commands via the Slow Control Serial Network (SCSN). Due to the serial nature of this protocol in which a frame is passed through a ring of MCMs the success of this operation proves the SCSN operational. This implies that more basic functionality, such as power or clock distribution to the MCMs, is functional. Only in case of problems in this sequence, more detailed investigations are necessary.

At this stage the access to the MCMs has been proved and can be used to further interact with them. The configuration of the MCMs covers the upload of the instructions for the TRAP CPUs as well as the setting of control registers (mentioned in section 2.3) which are finally done by SCSN write commands to individual MCMs or as broadcast to all MCMs in a ring. Due to the complexity of these settings this procedure has to be automatized which is achieved by a multi-layered configuration scheme. The underlying information about the configuration is contained in scripts of configuration commands and an assembler program. These are translated into SCSN commands which are sent to the MCMs in the transition from `STANDBY_INITIALIZED` to `CONFIGURED`. Configurations can be built by combining such scripts. The configurations as well as the underlying scripts are uploaded to a database from where they can be accessed using a tag as reference. The process of configuration is triggered by the user by sending a command to the InterComLayer which calls a CommandCoder — combining the information from the database to a sequence of commands — and sends the configuration data to the FEE-server (s. Fig. 18). The FEE-server receives this configuration and the Control Engine (CE) which is part of the FEE-server issues the corresponding SCSN commands. Besides forwarding the write commands it translates special commands (which are not directly implemented in the SCSN bus) to perform special tasks, such as setting the correct half-chamber ID which is written to the header in the raw data stream.

The CE also implements test sequences. They include the test of the network interface as used for the readout, memory checks for the TRAPs and a test for the ORI. At the stage at CERN these tests are expected to be successful, but they may show improper connections and, therefore, should be part of the default test procedure. In case of broken network interface lines, spare connections can be activated by configuration settings.

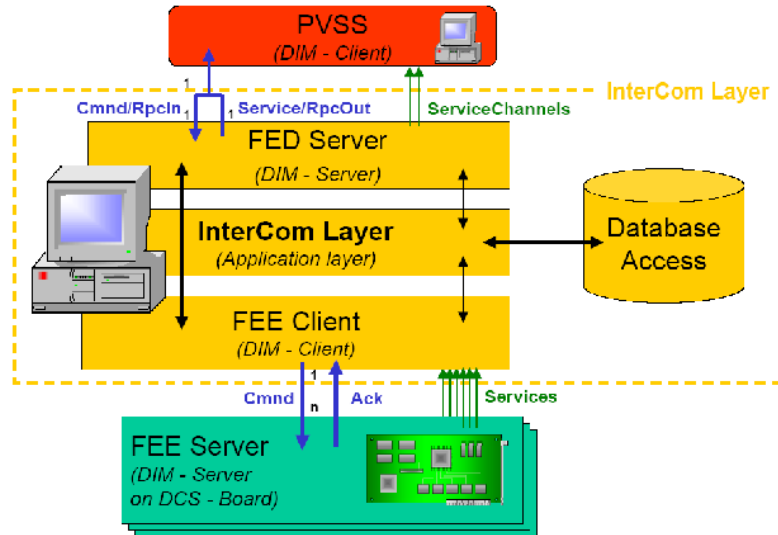


Figure 18: InterComLayer and FEE

Without cooling, the detector can be operated safely only for a short time (order of 5 min) with careful monitoring of the temperatures. On the other hand the basic operation of the electronics is needed for the verification of the cooling effectiveness as explained in the subsequent section. Therefore the steps described here might be interleaved by establishing the cooling. Additionally, these steps cannot be performed for the whole supermodule at once due to the limited power supplies.

With the readout electronics in operation, the optical output of the ORI boards can be checked. The comparison of the value as read from the monitoring diode on the ORI board and the optical power arriving at the GTU is a good indication of the quality of the interconnections. Since the ORI boards are normally not operated at their maximum power, a certain loss of power in the transmission can be compensated by adjustment. With the optical connections established, the supermodule is ready for full readout.

During surface testing the full readout is used for the acquisition of noise data which can be analyzed to check for either sources of high noise or dead channels (with less noise than expected). Furthermore, the full readout allows high statistic tests for transmission errors by using a special testpattern mode on the TRAP chips. Then the acquired data can be compared to the known pattern on the DAQ machine. This procedure is sensitive to errors in the full readout chain and is able to detect bitflips. The readout checks are described more detailed in section 4.4.

3.2.3 Cooling and temperature measurements

For the operation of the detector exceeding a few minutes, its cooling is essential and a failure would imply the loss of at least parts of the detector. Especially since

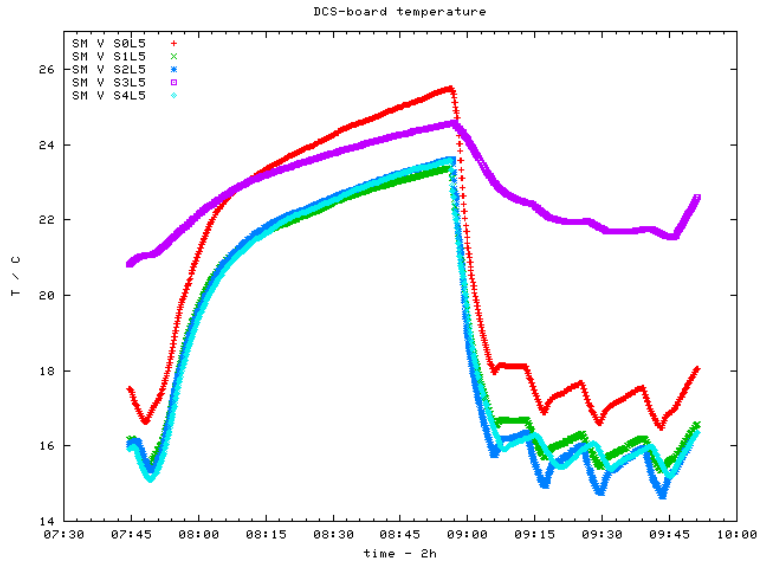


Figure 19: Chamber temperature as measured by the DCS board with cooling interruption and DCS boards powered only (Supermodule V, Layer 5, 29.04.2008)

problems have been experienced, careful tests are performed to verify and ensure the effective cooling.

After connecting the cooling plant the closed circuit is tested with respect to its vacuum tightness. The system is evacuated to about -650 mbar — the vacuum pump being part of the underpressure cooling plant. Then the supermodule is separated by closing the intermediate valves and the pressure increase is monitored. An increase of 100 mbar/h is tolerated. During the test of completed supermodules only problems in the external connections were found and fixed by improving the connections. Only after a successful vacuum test, the water circulation is started while monitoring the pressure at inlet and outlet to ensure that the pressure within the cooling circuit is always below the ambient pressure. This can be controlled by an adjustable bypass in parallel to the supermodule which effectively changes the flow through the supermodule.

After establishing the water flow, its effectiveness has to be verified. The cooling of the individual chips is achieved by mounted aluminium panels cooled by glued cooling pipes running in r - φ -direction (s. Fig. 20). The pipes are supplied in parallel from the cooling bars running along the side of the supermodule. When the DCS boards are powered, the temperatures are measured by the attached NTC resistors and monitored. Since the DCS boards dissipate heat (about 4 W each) a stable temperature (around the adjusted value of the cooling system) indicates at least a minimal operation of the cooling. Furthermore, the cooling system as used in the cleanroom provides a continuous water circulation with intermittent active cooling intervals. This is reflected in temperature fluctuations on the chambers. The amplitude of these fluctuations can be used to judge the effectiveness of the cooling. In

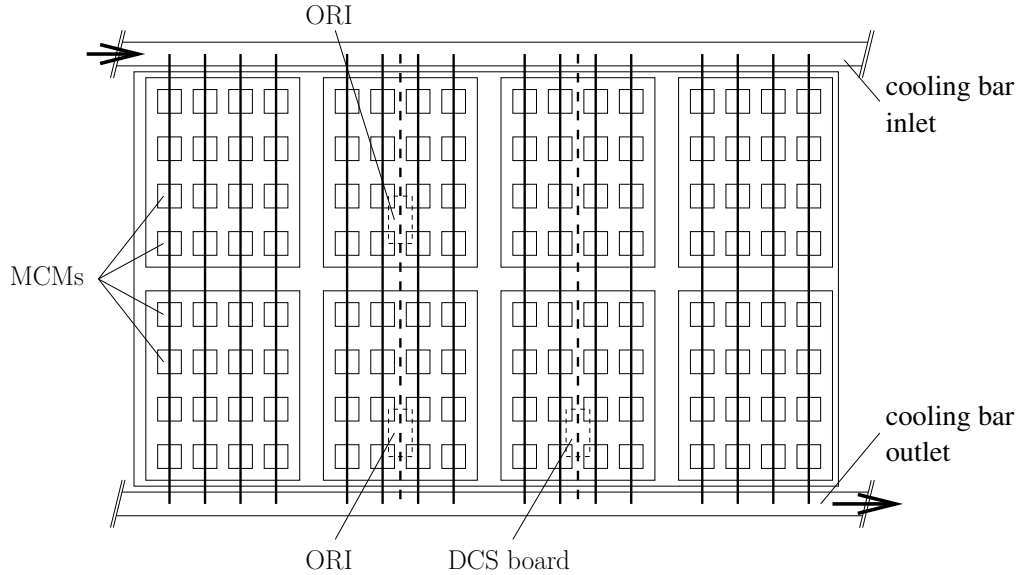


Figure 20: Sketch of the cooling connections

case of no or reduced water flow the fluctuation is nearly suppressed but still visible due to the influence of the adjacent cooling lines. Fig. 19 shows the temperature evolution during a test of 5 chambers within one layer of a supermodule with only the DCS boards powered. The steep rise in temperature is induced by switching off the cooling. Before the saturation of the temperature — which would still be at a tolerable level since it is a top layer — the cooling was turned on again. In the chambers with a fully working cooling line on the DCS board the temperature drops rapidly and shows the typical fluctuations. The purple curve shows the behaviour of a chamber without efficient cooling leading to a slower temperature drop and a reduced fluctuation amplitude. Invisible in the plot is the fact that the temperatures on all chambers after a sufficiently long shutdown are the same so that the effect is not due to miscalibration of the temperature sensor. With only the DCS boards powered this test is only sensitive to problems in the cooling line used for the DCS board.

The further tests require the operationability of the Front-End electronics dissipating much more heat during operation. If the temperature is still stable the cooling is sufficient to avoid high temperatures above the chamber in the region of the DCS boards, where the temperature sensor is located. But it does not prove the operationability of the individual cooling lines. For this a more detailed monitoring is necessary which involves the readout of the core temperature within the TRAP. This provides, even without calibration, the information about the operation of the cooling plant.

To conclude on the cooling efficiency the following sequence is executed while recording the MCM temperature values (assuming access via DCS boards):

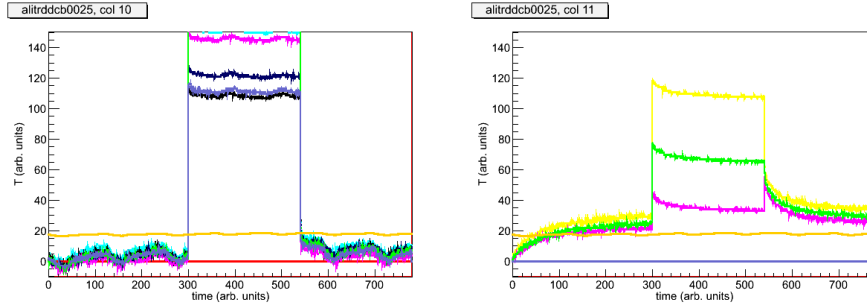


Figure 21: Temperature as measured by the TRAP temperature sensors during a test cycle (Supermodule V, Layer 5, 29.04.2008). The left plot shows the temperature curves from a series of MCMs in a row with working cooling line. The right plot shows a row without cooling.

1. The readout boards with the MCMs are powered.
2. A set of initialization commands is sent to the MCMs which keeps the power consumption and, thus, the heat dissipation rather low.
3. After a while the MCMs are sent a configuration which results in the activity of the CPUs leading to an increased heat dissipation.
4. The MCMs are put back to the state as in item 2.

Examples of such measurements are shown in Fig. 21. Each of the diagrams shows the values as delivered by the MCMs within one row. Due to intrinsic problems in the MCMs not all of them can be used for the temperature measurement. Due to the serial connection in each row the measurement on at least one MCM is sufficient to judge the cooling effectiveness of all lines from the development of the values in time without referring to the absolute scale. The left graph shows the evolution as observed for a working cooling line, characterized by the fluctuations and a steep rise and fall when the MCMs are configured or unconfigured, respectively. In contrast, the right graph differs by the lack of the fluctuations and a long tail in the temperature decrease. A detailed measurement like this identifies problematic cooling lines and is unavoidable for a reliable check.

3.2.4 Gas system

As the TRD relies on the use of the very expensive Xenon gas for the transition radiation detection, the leak tightness is extremely important because a leaking supermodule would be unaffordable to operate. Since problems have been observed which had not been discovered in previous tests this has to be checked extremely carefully prior to installation. The relevant tests are independent of the previously

described ones and can, therefore, be done in parallel or started before since they require long term observations.

With the gas system as available in the cleanroom a first check showing large leaks can be done by flushing the supermodule with gas, usually Ar/CO₂ at a slight overpressure of $\Delta p \approx 0.5$ mbar. Then the connections are closed such that an overpressure is kept which is visible on the liquid level in the bubbler. By observing the decrease of the pressure within the chambers an estimate on the leak rate can be made. Assuming a leak through which the flow Φ is proportional to the pressure difference Δp it can be characterized by the leak conductance σ :

$$\sigma = \frac{\Phi}{\Delta p} \quad (1)$$

with the gas flow referring to the amount of gas per time interval t passing through the leak. At constant temperature T this is given by:

$$\Phi = \frac{NkT}{t} = \frac{p \cdot V}{t} \quad (2)$$

resulting in the unit $\frac{\text{lbar}}{\text{h}}$ for the gas flow and $\frac{1}{\text{h}}$ for the leak conductance. Under these assumptions, a leak with leak conductance σ in a volume V under overpressure Δp leads to a flow:

$$\Phi = \sigma \cdot \Delta p \quad (3)$$

which induces a pressure decrease approximated by the ideal gas equation:

$$p \cdot V = NkT \quad (4)$$

leading to:

$$\frac{dp}{dt} = \frac{kT}{V} \frac{dN}{dt} = \frac{kT}{V} \sigma \Delta p . \quad (5)$$

This implies an exponential approach of the pressure difference to 0. Thus, by the comparison of the pressure difference at two times the leak conductance can be estimated:

$$\sigma = -\frac{V}{t} \ln \left(\frac{\Delta p(t)}{\Delta p(0)} \right) . \quad (6)$$

With a gas volume of about 500 l per double-layer and an observable change in the pressure difference of $\frac{0.4 \text{ mbar}}{0.5 \text{ mbar}}$ this method is only suitable for the detection of sufficiently large leaks. For a leak with the target conductance of $3 \frac{1}{\text{h}}$ one would have to wait about 40 hours. On this time-scale atmospheric pressure variations become significant. On the other hand, large leaks are quickly amenable to this method.

For smaller leaks a more involved method has been used. By flushing the chambers with Ar/CO₂ at underpressure, generated by fans, the effect of a leak is reversed with the gas streaming inwards. This makes it possible to estimate the leak rate by the measurement of the oxygen contamination in the chamber gas. As the following

calculation shows this method is suited for the detection of leaks in the target leak rate range.

Assuming a chamber at underpressure of Δp with respect to the ambient pressure a leak conductance of σ leads to an airflow into the chamber:

$$\Phi = \Delta p \cdot \sigma \quad (7)$$

resulting in an oxygen flow of:

$$\Phi_{O_2} = c_{O_2}^{\text{amb}} \cdot \Phi \quad (8)$$

with the ambient oxygen concentration $c_{O_2}^{\text{amb}} \approx 21\%$. With a flow of clean Ar/CO₂ through the chamber this results in an O₂ concentration of:

$$c_{O_2} = \frac{\Phi_{O_2}}{\Phi_{Ar/CO_2}} = \Delta p \cdot \sigma \cdot c_{O_2}^{\text{amb}} \cdot \frac{1}{\Phi_{Ar/CO_2}} \quad (9)$$

Therefore, the O₂ concentration measurement can be used to estimate the leak conductance according to:

$$\sigma = \frac{c_{O_2}}{c_{O_2}^{\text{amb}}} \cdot \underbrace{\Phi_{Ar/CO_2}}_{\text{in } \frac{\text{l}\cdot\text{bar}}{\text{h}}} \cdot \frac{1}{\Delta p} \quad (10)$$

With a typical input gas flow of $20 \frac{\text{l}\cdot\text{bar}}{\text{h}}$ the oxygen contamination listed in Table 4 are the thresholds corresponding to the accepted leak conductance of $3 \frac{\text{l}}{\text{h}}$ and $10 \frac{\text{l}}{\text{h}}$, respectively.

Δp (mbar)	$\sigma = 3 \frac{\text{l}}{\text{h}}$	$\sigma = 10 \frac{\text{l}}{\text{h}}$
0.1	3 ppm	10 ppm
0.2	6 ppm	20 ppm
0.3	9 ppm	30 ppm
0.4	12 ppm	40 ppm
0.5	15 ppm	50 ppm

Table 4: Oxygen contamination corresponding to maximum leak conductance at a flow of $20 \frac{\text{l}\cdot\text{bar}}{\text{h}}$

3.2.5 High Voltage

The main purpose of the high voltage tests at CERN has been to detect transportation damages, e. g. broken wires. For long term observations the time was lacking. Therefore, the high voltage test for both, drift and anode voltage, comprises the ramping to some voltage, keeping it for some time and then ramping down. By

resistance drift voltage	12.7 M Ω
capacitance of HV-cables	167 pF/m

Table 5: Electric properties of the high voltage system

this procedure several things can be checked. During the ramping of the voltage a charging current should be seen due to the capacitance of the filter capacitors (depends on the used filter-box) and the high voltage cables themselves. The lack of this current indicates a disconnected cable. When a stable voltage is reached, the current on the anode channel is expected to be negligible ($< 1\text{nA}$) while the drift current should correspond to the resistance of the voltage divider chain used in the field cage.

From the measurements both the capacitance and the resistance can be calculated on a chamber by chamber basis and compared to their nominal values. In case of a broken wire inside the chamber due to the transportation a short-circuit is expected. Table 5 shows the corresponding capacitance and resistance for the channels from which the currents can be calculated.

3.2.6 Front-End Electronics stress tests

Due to the complexity of the readout electronics it is quite susceptible to misconfiguration and improper connections resulting in crashes during the data-taking. Such crashes can lead to the loss of the affected half-chamber until reconfiguration. Since the TRAPs do not go to the sleep mode any more, their power consumption is increased. This can result in a low voltage trip and, thus, the loss of the complete double-layer. In the end most of the crashes are generated by an MCM receiving a trigger signal at a time where none is expected.

For long term data-taking the stable operation of the detector is extremely important. An easy test for it can be performed by applying a trigger rate of 1 kHz to the electronics without busy protection for a long time ($\geq 12\text{ h}$). These tests are called stress tests. Since accumulated crashes of MCMs may lead to a trip of the low voltage, which prevents the tracing of the problems, an intermediate readout of the status is done in specified time intervals. This procedure is automated following the sequence as shown in Fig. 22.

In case of observed problems after the end of the stress test the produced log-files can be used to find the initial reason for the crash. Furthermore, this procedure also tests the reliable trigger distribution since the number of received triggers on each MCM can be checked and should be the same within the whole supermodule.

These tests have proved to be extremely sensitive to any electronics problems and should be repeated after any possible modification of the electronics. Crashes may arise from different reasons, s. a.:

- bad network interface connection

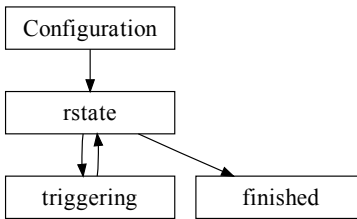


Figure 22: Stress test

- unstable low voltage supply
- unstable trigger timing

The effect is that the state machine of the TRAP stays in a wrong state.

3.2.7 JTAG tests

The JTAG interface of the DCS boards provides low-level access to its hardware components which can be used in case of Ethernet failures. Since an external JTAG connection to the boards in the supermodules is not available each DCS board has a JTAG master implemented in the on-board FPGA. In this way, an internal loop can be built with each board connected to one of its neighbours as slave and to the other one as master. Thus, JTAG access to every DCS board is given from one of its neighbours.

With the JTAG master implemented in the FPGA, it is susceptible to bugs in the firmware or interruptions of its programming process. Due to the importance of this interface an automated test procedure is needed which can be run before or during the procedure of a firmware upgrade — which is done in two steps such that all boards being flashed can be accessed by JTAG as shown in Fig. 23.

For the automated test a procedure is used that checks the integrity of the JTAG loop. It runs on a machine in the DCS network and starts by logging on to a specified DCS board. From there it tries to detect the slaves on the JTAG chain by using the JTAG connection — the chain contains the flash memory, the ARM processor and the FPGA part. If successful it reads back the serial number of the next board from its memory. With this information it retrieves the IP address of the next board from the database containing the mapping between serial number and installation position. After rebooting the next board — which is necessary due to the fatal consequences of the external memory access — it logs on to the next board. The test proceeds in this way until either the first board is reached again or an unexpected JTAG chain is found. If the loop is closed by reaching again the initial board JTAG can be considered as working with the detection of the chain and data transmission as verified.

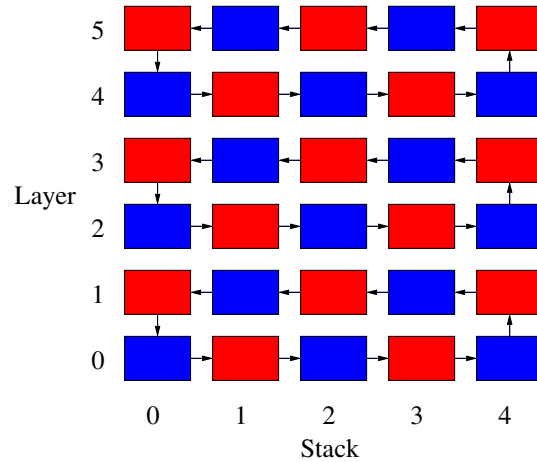


Figure 23: The DCS boards are connected to form three JTAG loops. Firmware updates are done in two steps. First the red group is updated. In case of failures during the flashing process the boards are still accessible from the ones of the blue group. In the next step the other DCS boards are updated.

3.3 Supermodule repairs

The above described tests are appropriate for the test of completed supermodules for which no major problems are expected. Besides these routine tests the facilities at CERN have been used for the repair of faulty supermodules in which case the tests are expected to fail frequently and must be used for the detection of problems during the ongoing work.

3.3.1 Observed issues

The following repair work has been performed in the cleanroom:

SM III: This supermodule was used for a testbeam in November 2007 for which it was operated with the final Xe/CO₂ gas mixture in order to take reference data for the TRD PID reconstruction. During this test a major gas leak was detected which could not be identified during the operation of the detector. For the detailed investigations the supermodule had to be opened and partially disassembled. In the end it was completely disassembled due to major gas leaks also in lower layers. After the full dis-assembly of the supermodule the components were shipped back to Münster and GSI, respectively, for the re-assembly.

SM IV: Also supermodule IV suffered from gas leaks distributed over all layers. Therefore this supermodule had to be completely disassembled and repaired. This repair was done at CERN.

SM V: A cooling problem in layer 5 was detected in supermodule V during the tests in the cleanroom (s. section 3.2.3). This required the removal of the top panel of the supermodule for the investigation. The problem was caused by squeezed silicon cooling hoses in the connection to the cooling bars. It could be fixed by replacing these connections. Nevertheless, more detailed tests of the electronics were needed after these modifications.

Since the individual chambers are only accessible by the removal of the layers on top, the above mentioned problems required the dis-assembly of the supermodules. Once the access to the chambers is given the repair of the individual chambers can be done.

3.3.2 Supermodule Re-Assembly

During the re-assembly even more careful tests are necessary and they have to be repeated at different stages of the re-assembly because the insertion of further chambers can introduce new problems.

The re-assembly of the supermodule has to happen layer-wise, starting from layer 0, whereby the sequence for each layer is as follows:

- The first step is the insertion of the chambers in the supermodule hull. This must start from stack 2 which is most difficult to access. The chamber is roughly aligned along the supermodule hull and then fixed by screws which also connect the ground cables. Afterwards the chambers around the middle stack are inserted and pushed towards stack 2. This establishes the gas interconnections. For this procedure it is extremely important not to forget the additional beams needed for the stability of the supermodule hull as well as to check the alignment of the chambers such that they mechanically fit.

For this work 4 people are needed for about 2 hours.

- During the insertion the gas interconnections must be checked carefully. It was found that they are quite robust against small movements of the chambers but dirt on the O-rings used for the interconnection can lead to significant leaks.
- Once all chambers of a layer are inserted and the gas interconnections are established it should be connected to the gas system and flushed with Ar/CO₂. This should happen as early as possible since the gas tests require a lot of time (on the order of days).

For the fastest progress, the chambers should be flushed with Ar/CO₂ at overpressure until the oxygen level is in the ppm range. This lasts about 24 hours. Afterwards, the chambers can be brought to underpressure. When the oxygen contamination stabilized (after another 24 hours) it can be used to calculate the leak conductance as described in section 3.2.4.

- When the gas test is started the routing of the cables along the side of the supermodule can be started. This includes the connections needed for the low voltage, high voltage and Ethernet. The routing of these cables has to be done rather carefully due to the limited space available.

The routing of the cables can be done in about an hour.

- After the routing of the cables, the connections of the power cables for the DCS boards as well as the readout boards can be connected. This blocks the free access to the cables along the side and therefore this should only be done when all routing is finished. In this procedure it should also be taken care of the path of the cables. For the function of the detector the routing of the cables, s. a. low voltage for the DCS boards, JTAG etc., are quite important. From Fig. 24 it can be seen that the wrong routing of the cables, i. e. close to the pad plane cables, leads to increased noise in the affected pads.
- The next step is to connect the silicon hoses of the cooling pipes to the cooling bars running along the side of the supermodule. In this step one should check on the optimal length of the hoses so that they cannot be squeezed while inserting the layer or panel on top.
- Once the high voltage cables are soldered to the patch-panel in the front of the supermodule the individual high voltage channels can be checked.
- Then one should try to power the DCS boards and get access to the chamber. After switching on the readout boards the configuration of the chambers should be tested to detect missing or improper connections between the readout boards.
- If the steps so far have been successful, the preparations for the full test of the readout electronics can proceed: The trigger fibres must be pulled from the splitting box in the front of the supermodule to each DCS board. This single trigger connection for each chamber must be routed carefully such that it cannot be damaged during further work. The same holds for the readout fibres from each half-chamber to the patch-panel in the front of the supermodule.
- With the optical fibres connected the readout tests can be started. For these tests random or periodic triggers are used and the data is recorded. During this stage it can be helpful to run the electronics in the testpattern mode to check for bitflips. This can indicate problematic network interface interconnections between readout boards.
- When the readout is established the data taken can be analysed with respect to the noise level. If the noise of some channels (or groups of channels) is too low, it hints at a missing connection to the pad plane. This can easily happen if the pad plane cables had been disconnected. If the noise is very

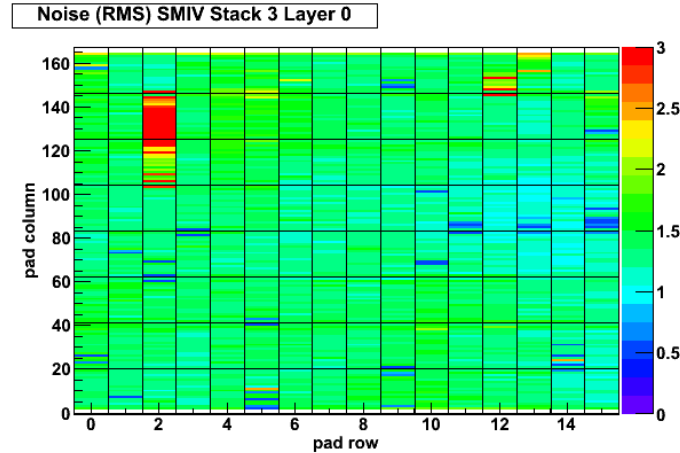


Figure 24: Noise distribution on a chamber as can be induced by badly routed cable. The black lines indicate the MCM boundaries and the shared channels are plotted twice.

high, this can be caused by cables routed close to the PASA input. This has to be avoided.

- If the readout is operational and the layer is finalized the final check of the electronics can be done, i. e. the stress test. The long term stability of the electronics is a good indicator for problems in the connections.

Also the cooling connections have to be checked regularly, both for vacuum tightness and water flow. The latter can be easily checked by touching the cooling panels on the MCMs as long as they are still accessible. After the insertion of the next layer, the cooling can only be monitored by the temperature measurements as described in a previous section.

The high voltage connections are quite sensitive and can easily break during mechanical manipulations on the chambers. They also have to be checked regularly with monitoring the currents.

3.4 Conclusions

During the time of the supermodule repair at CERN some conclusions were drawn on the most efficient procedure. The clear organization of the sequence helps to save time and to avoid the doubling of activities. If tests are not passed it often showed dispensable to continue with actions that had to be repeated anyway after fixing the original problem.

Some problems were observed with rather high frequency. On the other hand, once known, they are quite easy to avoid. These problems include the bad routing of

cables along the readout boards resulting in extremely high noise. Another problematic item is the connection of the pad plane cables to the connector on the readout board. It can be hard to judge by eye whether a connection is good or not; but the problem can be easily identified from the noise plot for the chamber. Therefore it is highly recommended to analyse the noise plots not only with respect to regions of high noise but also to low noise. A crucial problem are the cooling connections which have been found to be very susceptible to squeezing during the further assembly. Therefore, the test of the cooling efficiency as described in a previous section should be repeated after the insertion of the next layer or the installation of the top panel, respectively.

In total it was found that the re-assembly of a full supermodule can be very time-consuming. The most critical part in it are the gas tests which unavoidably need a long time to give a significant result.

4 Installation and Commissioning

This chapter describes the supermodule installation in the experimental cavern and the following steps to bring it to full operation. First, a general overview of the procedure is given. In section 4.2 the preparations are discussed which should precede the installation in order to facilitate the connections afterwards. Subsequently, the basic tests after the installation are described. They should verify the operation of the supermodule quickly after the installation. The last sections describe some achievements during the 2008 run.

4.1 Installation procedure

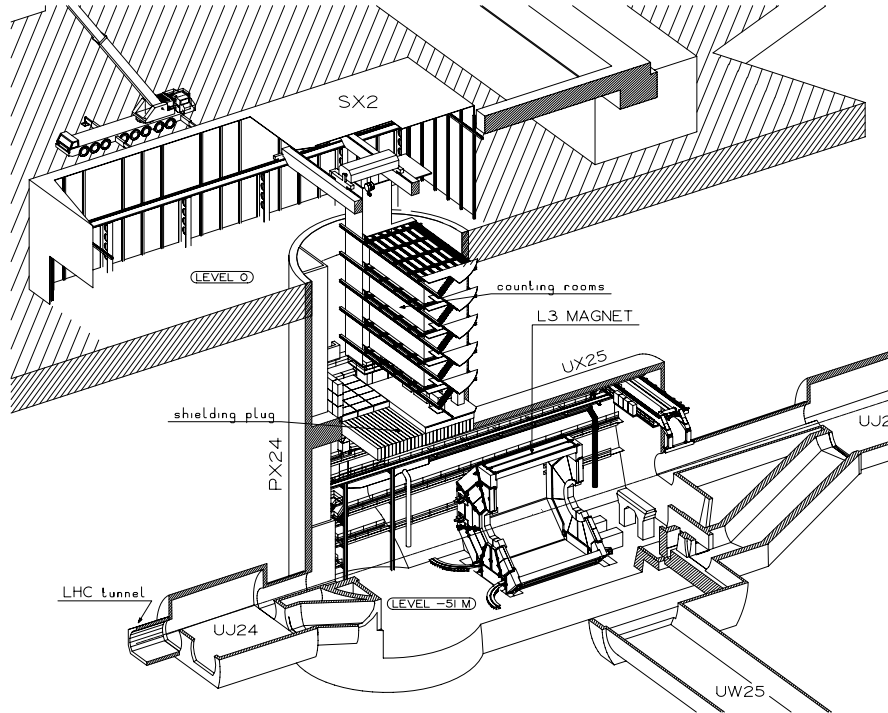


Figure 25: Overview of the experimental area [14]: The experiment is hosted in the cavern UX25 where the magnet is shown. The material has to be brought in through the shaft from the experimental hall SX2. The sides of the magnet pointing in clockwise (right in the drawing) and anti-clockwise beam direction are named C- and A-side, respectively. The inner and outer side of the ring are named I- and O-side.

Having passed the tests in the cleanroom successfully, the supermodule is transported in the rotator to the experimental hall SX2 (s. Fig. 25). From there it is lowered by a crane to the experimental cavern UX25. To insert the supermodule

into the spaceframe, which holds the barrel detectors in the magnet, an installation platform is setup in order to position the supermodule exactly in front of the slot within the spaceframe. Once it is well aligned it can be pulled in by a winch.

In the spaceframe the access to the supermodule is very limited. Therefore, as many connections as possible should be prepared and well routed in advance.

4.2 Services and Infrastructure

On the supermodule side, the service connections in the final installation are essentially the same as in the cleanroom. But the infrastructure cannot be placed close to it and is quite distributed. This results in complications compared to the cleanroom setup.

Low Voltage: The low voltage power supplies are installed in racks on the galleries on the I- and O-side of the cavern. From there copper cables are connected to patch panels at the supermodule installation positions in the magnet. In addition, there are sense wires in parallel to the cables to allow the power supplies to compensate for the voltage drop. This is significant with a typical resistance of the low voltage cables of 5 m Ω and currents of about 100 A.

During the installations, incorrect mappings of the individual cables were found. These are difficult to correct after the supermodule installation due to the limited access. It is highly recommendable to perform appropriate tests before. Besides basic connectivity tests, a shunt resistor can be attached to the terminals of the patch panels instead of the supermodule. Then the measured terminal- and sense-voltages on the power supply can be checked. This procedure is sensitive to mistakes in the cabling, also of the sense-wires, as a voltage drop has to be observed (the sense-wires have a 1 k Ω pull-up resistor to the terminal voltage inside the power supply such that the power supply can also be operated with disconnected sense-wires).

Cooling: The cooling plant is placed on the A-side of the experiment from where separately controllable lines are routed to each supermodule. They have to be tested for tightness before the installation of the supermodule since tests afterwards can be very time-consuming. This can be done by connecting a bypass instead of the supermodule. Then, the full operation of the cooling can be tested and leaks in the connection lines up to the supermodule become apparent.

Ethernet: The switches for the Ethernet connections are installed in racks on the galleries on the I-, O-side and C-side of the cavern. The outlets of the supermodule on the A-side are split to the I- and O-side switches depending on their installation position. The C-side connections are common.

Many mapping problems in these cables, such as the swapping of pairs, have been found which would be automatically corrected by modern Fast-Ethernet cards. Due to the sharing of the cables for two Ethernet connections the swapping leads to an uncorrectable mixing of the signals between different DCS boards.

High Voltage: The high voltage power supplies are placed in a counting room in the shaft down to the experiment. From there, cables are routed to the racks on the I- and O-side of the cavern where they are patched to the cables into the magnet.

Gas: The gas system is rather involved due to the necessity for Xenon recovery. It is placed in a building on the surface. From there lines to the supermodule are routed to the cavern via the gas control system. It is installed just above the shielding plug (s. Fig. 25) and allows the individual control of the lines.

Trigger: The trigger distribution in the final installation is different from the one in the cleanroom by the additional pretrigger system. As only the connection from the pretrigger box in the magnet to the supermodule is individual, only this part has to be tested for each sector.

GTU and DAQ: For the readout of the detector the Global Tracking Unit (GTU) is installed in the racks in the C-side of the experiment. From there the connection to the Data Acquisition (DAQ) system is established via Detector Data Links (DDL).

Monitoring and Control: The monitoring and control are done remotely since the access to the cavern is impossible during beam-time. The necessary software is hosted on a series of PCs (workernodes) in one of the counting rooms.

All connections should be checked up to the supermodule before the installation. The checks prior to the installation are summarized in a checklist in appendix B.2. With all connections working the supermodule can be made operational very quickly after its installation. This might become important for future installations in the limited time of the accelerator shutdowns.

4.3 After the insertion of the supermodule

After the supermodule is pulled into the spaceframe all the service connections must be established. A certain order in the steps proved most convenient, mainly determined by the space limitations. At the current installation stage, access is only possible to the front-panels of the supermodule from the radially inner side.

- The connection of the stiff cooling pipes requires access to the supermodule involving heavy tools. Therefore, these connections should be done first and

checked with respect to leak tightness as long as the access to the connections is still easy. A few hours should be planned for this step.

- Afterwards, the low voltage can be connected. The short patch-cables from the patch-panel in the backframe to the supermodule patch-panel are also very stiff. It was found that the stress, mainly caused by the elastic insulation, can be reduced by temporarily heating the cables in their final position.
- The next step is the connection of the 15 Ethernet and 2 redundant PDB control cables which is quick.
- As one of the last steps requiring physical access the 60 optical readout fibres should be connected (C-side). They must be routed from the supermodule to a patch-panel in the back-frame. The two trigger fibres must be connected as well. Because of their fragility, this step should only be done in the very end.
- Finally, the gas pipes can also be connected (A-side). This includes the installation of the fragile glass-made bubbler as overpressure protection and all subsequent interventions must be done carefully.

With the supermodule fully connected basic checks can be done to verify the operation as quickly as possible. These tests are mainly a repetition of those in the cleanroom:

- The voltage at the PDB should be checked with respect to its value and polarity prior to switching on the DCS boards. Then, the voltage should be stable and the current should be about 1 A per DCS board.
- The DCS boards now provide further information, such as the temperature on the surface of the chamber. Thus, the basic operation of the cooling system can be checked.
- The ADC chip on the DCS board is used to measure the voltages on the power bus bars for the supply of the readout boards. This can be used continuously to monitor that the proper voltages really reach the power bus bar and is helpful during the first checks.
- If no problems are found, the Front-End Electronics can be switched on. Due to the high currents problematic contacts might induce significant voltage drops. This should be checked from the measured voltages on the power bus bars.
- Subsequently, the configuration of the Front-End Electronics and the JTAG loops should be fully operational. After ensuring sufficient cooling the detector is ready for operation.

- The application of a random trigger should lead to the same event count on all chambers in the supermodule. Additionally, the error counters of the TTCrx chip can be read out.
- If the optical connections are operational, the detector can be read out. Noise data can be used again to identify problematic regions within the detector.
- When no further access to the supermodule is necessary, the high voltage can be tested.
- Independently, the gas system can be operated to detect possible leaks.

In addition to the tests as done in the cleanroom the optical damping on the readout fibres has to be checked since long distances and many interconnections (on patch panels) have to be overcome. This can be checked by the comparison of the measurements from the monitoring diode on the ORI board and the received optical power in the GTU receiver modules. Furthermore, the cooling efficiency has to be checked again since the behaviour of the cooling plant in the cavern and in the cleanroom is different.

4.4 Readout checks

During the commissioning of the detector it is essential to have a quick feedback on the integrity of the acquired data. A verification that the format specifications are fulfilled is needed to avoid corrupted data which cannot be analysed. It is favourable to run such a check already during the data taking without the requirement to wait for the data availability on the mass storage system. These needs can be fulfilled by using the data arriving on the DAQ machines. An interface is provided to retrieve the raw data giving full access also for low-level checks.

The data acquisition chain is shown in Fig. 26. The data from each supermodule is buffered in a GTU segment and transferred to a DAQ machine via a Detector Data Link (DDL), i. e. an optical fibre connection. Each Local Data Concentrator (LDC) receives the data of 6 TRD supermodules and forwards it to the Global Data Concentrators (GDC). They combine the data of all detectors for one event (eventbuilding). To cope with a high event and data rate the load on the GDC level can be shared by shipping each event to a different GDC. Both LDCs and GDCs make the raw data accessible for on-line checks. Thereby, the data can be checked on-line during normal data-taking. The routine checking of the supermodule data should be as robust to data corruption as possible and provide helpful output for the identification of problems. On the other hand, it must be sufficiently fast. It has proved feasible to analyse the data at a high rate down to the level of all ADC channels which are checked for reasonable values (in noise events).

A checking routine reads the data of a half-chamber, as shown in Fig. 6, sequentially. The data is organized in 32-bit words. The tracklets (s. section 5.2) appear

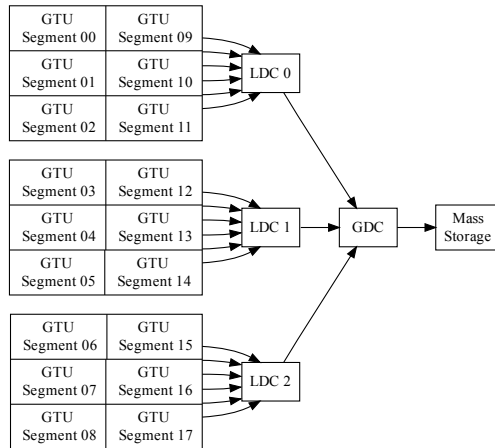


Figure 26: Data acquisition scheme as in the 2008 run

first in the data stream as they are needed for the trigger decision. Their transmission is terminated by the tracklet endmarkers `0x10001000`. It is continued by the raw data. This is started by two half-chamber header words encoding the position of the half-chamber in the detector, the event number and the type of data. The latter refers to (non-)zero-suppressed or a testpattern mode [27]. This information is needed and used for the interpretation of the following data.

In the case of the testpattern mode the data is checked against the known sequence of values, e. g. from a pseudorandom number generator with a known seed.

In the case of zero-suppressed data⁸ only those channels with ADC values exceeding a configurable threshold are transferred. The values can be assigned to a location from the MCM header which encodes the position within the chamber. It is followed by the ADC mask of active channels on this MCM. The number of active channels is additionally transferred as a cross-check. During the checking, the MCM header is used to verify the correct readout order. The ADC mask is needed to interpret the following data which is the ADC values. Three sampled ADC values (10 bit/sample) are packed into one word. The 2 additional bits are used for data integrity checks. If the number of timebins is N_{timebins} , the full data of one ADC channel consumes $\lceil \frac{N_{\text{timebins}}}{3} \rceil$. In case of a mismatch between the number of active channels encoded in the mask and the number sent, for all values between the minimum and the maximum of the two it is checked whether at the corresponding position an MCM header follows. This value is used for the further interpretation of the data. Thereby, an error-tolerant method is achieved and the checking does

⁸The description here holds for the mode with disabled empty headers. Otherwise the headers of all MCMs are sent even if they do not have active channels.

0x23abbd95	tracklet
0x10001000	tracklet endmarker
0x10001000	
0xd1004001	HC 0
0x7914aad5	HC 1
0x9c0006bc	MCM header
	ADC mask
	ADC data channel 0
	⋮
0x00000000	data endmarker
0x00000000	

Table 6: Raw data from one link (case of zs data)

not necessarily stop at the first occurrence of such a problem as it may arise from bitflips.

All detected errors are accumulated in a statistic module on different levels of readout hierarchy: If a problem is found e. g. in the half-chamber header it is registered on the link-level. This principle holds also for the levels of readout boards and MCMs. This accumulation of errors allows to quickly detect in which connection in the readout tree problems occur. Typically, the malfunctioning of individual lines between two chips is responsible for the observed problems. Normally, they can be fixed by the application of patches reconfiguring which connections to use for the network interface (there are two spare connections per MCM-MCM connection).

The above description of the checking principle holds for the data of one half-chamber as it reaches the GTU on one optical link. On the GTU the data from all links are concatenated and preceded by GTU headers a Common Data Header (CDH). As such they are sent to the LDC where another header is added before the data is forwarded to the GDC. Here, the data from all detectors read out in this specific event, i. e. not necessarily only TRD, are combined and another header is added.

Thus, it is necessary to extract the data of each half-chamber in the full raw data stream and pass it to the checking procedure. This extraction is not specific to the kind of data that is transferred to the DAQ and only depends on its format specification. Therefore, the supermodule data checking has been included in a common framework that is also used for GTU tests and encapsulating the extraction of the half-chamber data [22].

In addition to checking the data integrity during a physics run the software can also be used specifically to detect bitflips by analyzing testpattern data produced on the TRAP chip. This method is sensitive to errors within the whole readout chain and allows to quickly find problematic connections. There are different versions of the testpattern mode. Pseudorandom numbers can be generated on the TRAP chips

with a known seed and checked for equivalence in the checking module.

For tests of the proper mapping within the offline reading code another testpattern encodes the supermodule, chamber, readout board and MCM numbers in the ADC values. This allows that the data can be read and stored as ADC values in the structures used for the off-line reconstruction. From the stored ADC values the origin can be deduced.

4.5 Noise measurements

During the installation period at CERN investigations into the electronics noise have been made. The expected noise level was estimated at the time of design, taking into account the electrical properties. This well-studied noise is caused by detector-intrinsic sources, s. a. the capacity of the pad plane, the connection cables and the PASA and TRAP. The nominal noise level in RMS is about 1 ADC count. To detect additional external disturbances methods of noise monitoring are required.

In order to trace external noise sources it is necessary to observe a possible dependency on ambient conditions, to monitor the spatial distribution of the noise level and examine the temporal evolution. The latter requires the continuous sampling over a long time. Furthermore, the frequency composition of the noise can help to identify its source.

4.5.1 RMS plots

In an ideal noise run (without signal) the values of a single ADC channel are expected to follow a Gaussian distribution centred around the configured pedestal value. The width of this distribution can be obtained from a fit and characterizes the noise level. This method relies on the Gaussian shape. If the noise structure is not well-known a characterization which is less specific about the shape of the distribution is the RMS of all ADC values. The RMS can be calculated from the ADC values retrieved from recorded data. Alternatively, the relevant sums can be accumulated on the TRAP during the run and read out via the Slow Control interface after the run as the data volume is small. The latter method permits a fast noise measurement not relying on the full readout chain. This is advantageous during commissioning.

4.5.2 Frequency spectrum

For the understanding of the noise structure and the derivation of its frequency composition the number of continuous samples in the mode of normal operation (maximum 64 timebins) is insufficient. This limitation can be circumvented by using the TRAP in a special mode. Then, up to 24000 samples are acquired continuously and recorded by one or two CPUs into the instruction memory of the unused CPUs. After the sampling is finished, the data can be read out via SCSN from the DCS board and further analyzed. This gives the possibility to check the time evolution

of the signal. The necessary configuration of the TRAP has been included in the libTRD.

Further conclusions can be drawn from the frequency spectrum as obtainable by the application of a Discrete Fourier Transform (DFT) to the sampled values. The frequency composition reveals if there are contributions of specific frequencies and can help to identify the noise source.

The DFT is analogous to the Fourier transform applied to continuous waveforms. Instead of the integration, finite sums have to be used leading to some drawbacks. The relevance of these influences shall be discussed in the following.

Physical signals can only be acquired in discrete samples over a finite time interval. Although the interval can be very long and the sampling frequency very high, the continuous integration over infinite time as in the Fourier transform is not achievable. But a similar transformation adapted to the discreteness of the data can be applied and the calculation of:

$$X(k) = \sum_{n=1}^N x(n) \exp\left(-i\frac{2\pi}{N}nk\right) \quad (11)$$

results in a spectrum of discrete frequency components. The discreteness of the transformation imposes some limitations. A signal containing frequencies above half the sampling frequency will erroneously contribute to frequency components between 0 and $\frac{f_s}{2}$ in the calculated spectrum. This cannot be distinguished in the sampled data. This effect is known as aliasing. Therefore, only signals without frequency components above $\frac{f_s}{2}$ can be analyzed meaningfully. In the case of the TRD electronics, this is guaranteed by the analogue stages before the digital sampling.

Another problem arises from the finiteness of the sampling window. If this window corresponds to a multiple of the period of the signal the calculated frequency composition is correct. Otherwise, a single true frequency (in a continuous signal which is then sampled) will contribute to more than one component in the frequency spectrum. This effect is known as leakage.

Technically, the calculation of the DFT can be done by fast algorithms, also known as Fast Fourier Transform (FFT). In such an analysis the results as shown in Fig. 30 were found. It clearly shows a time structure in the noise and a non-flat frequency distribution.

4.5.3 Common mode current noise

Besides the measurements on the level of the detector itself there have been external measurements. It was found that the noise as seen in the detector depends on the used power supplies, as is shown in Fig. 28. Therefore, common mode current noise studies have been performed, i. e. the measurement of the current difference between the two terminal lines — the two currents should be opposite and exactly equal⁹.

⁹The power supplies are built to be floating with respect to ground.

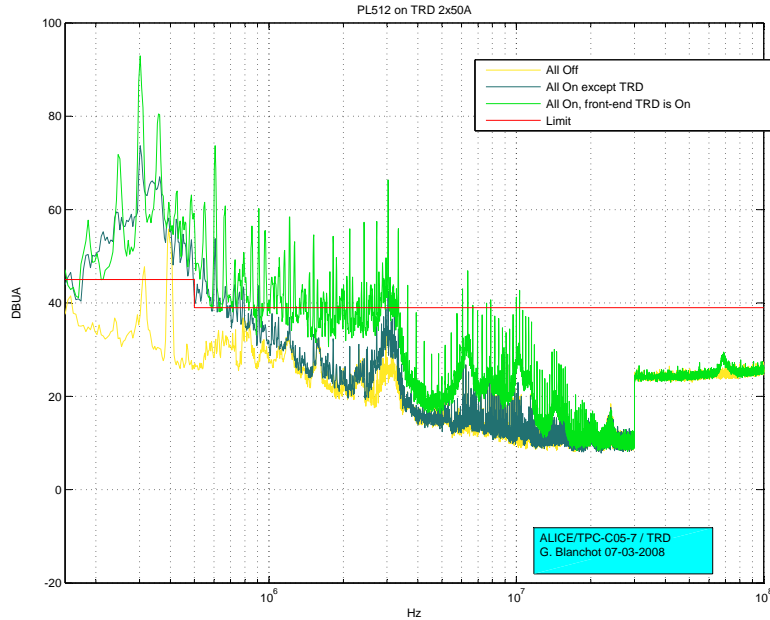


Figure 27: Common mode noise observed on PASA power supply for SM 00

Fig. 27 shows the frequency decomposed result of such a measurement.

4.5.4 Results

The measurements have been used to observe and identify a noise problem arising from the used low-voltage power supplies. The histograms (Fig. 28) show a comparison of the spatial noise distribution within one chamber with two different sets of power supplies. Due to these observations and similar results from the integration at Münster it was decided to modify the full set of the TRD power supplies by the addition of ferrites. This resulted in a significant decrease of the noise level as can be seen in Fig. 29.

4.6 Detector Control

The operation of the detector requires the remote control of many devices. As the Detector Control System (DCS) was evolving during the commissioning further needs became apparent and were included.

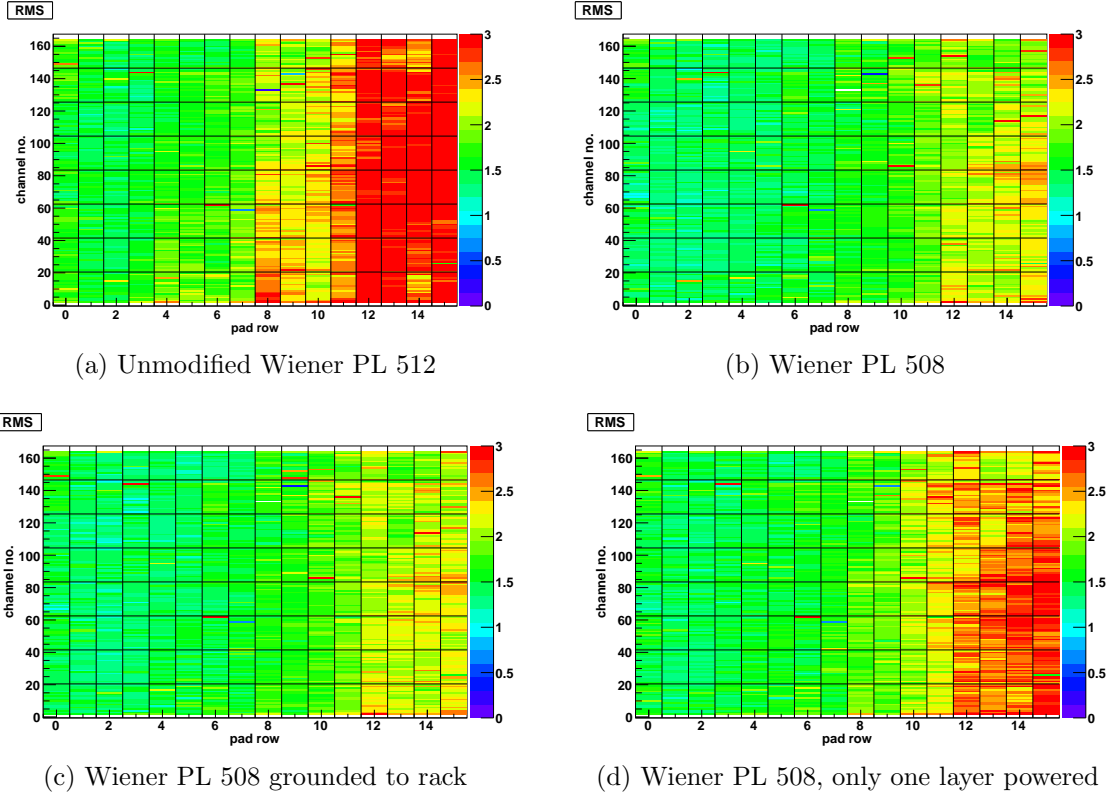


Figure 28: Noise comparison with Wiener power supplies PL 512 and PL 508

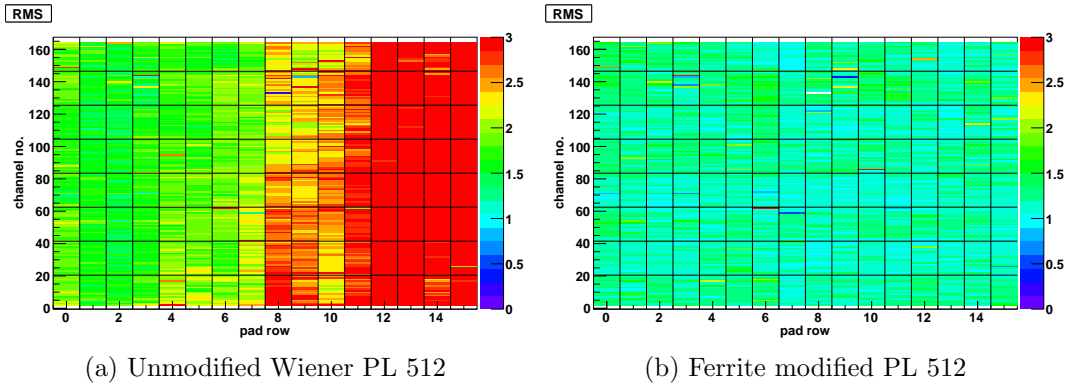


Figure 29: Noise using Wiener PL 512 without and with ferrite added.

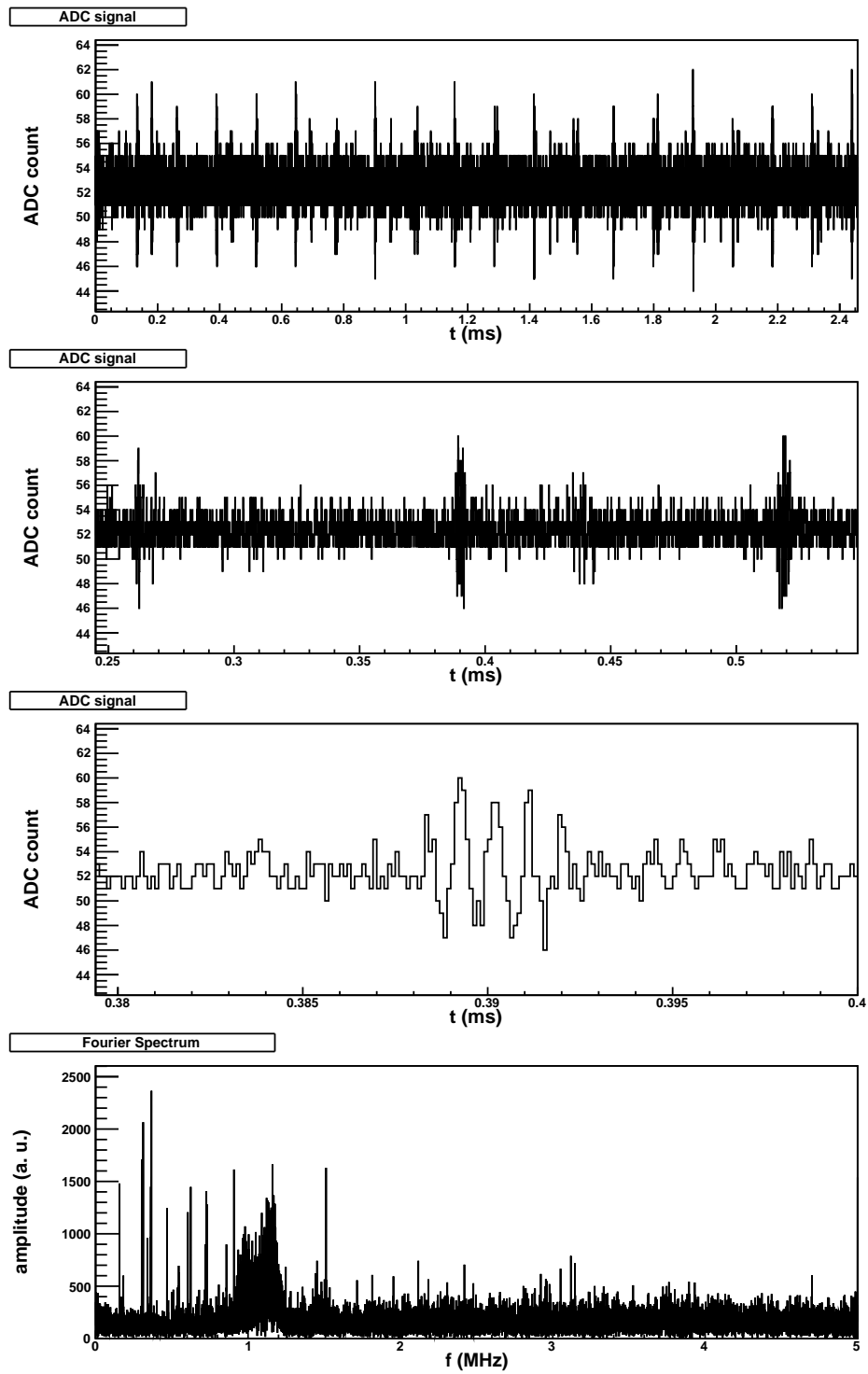


Figure 30: FFT spectrum as observed in the installed supermodules

4.6.1 PCU DIM-server

As described in section 2.6 the Power Control Unit (PCU) is the interface between the high level control software and the Power Distribution Control boards (PDC) in the Power Distribution Box (PDB). The PCU hosts a DCS board as an interface board. The latter contains the communication elements, such as line drivers etc. used for the control of the PDB. The communication logic is programmed into the FPGA on the DCS board. It is visible to the Linux operating system running on the ARM processor through a device driver. It holds a set of registers representing the requested state for the DCS boards in each supermodule which is transferred to the PDB by a serial point-to-point connection and is settable from the software.

This low-level interface should be completely hidden to the DCS. A DIM server which runs on the PCU DCS board was implemented to publish the current status of the connection to each supermodule and the status of the DCS boards via DIM.

For safety reasons the PCU features a timeout counter which switches off all DCS boards if it is not reset within a configurable time interval. The counter is realized in the FPGA and cleared by every write or read access to the status registers. The published states are updated only on request. This ensures that the detector is powered off if the control software does not run continuously. Since this is implemented as an autonomous system on the FPGA it does not rely on software stability. The state of this timeout counter as well as its configuration is published via DIM. If the timeout counter fired it has to be reset by a special command before any switching transitions are possible.

The source code of this server is available in the TRD subversion repository [34] as package `pcudim`.

4.6.2 Remote command execution via DIM

Based on the fact that all DCS boards are running a Linux operating system and are connected by Ethernet many settings can be easily configured or checked from the commandline interface of a secure shell session. All the features contained in the `libTRD` (the library containing TRD-specific control software) are made available to commandline tools. Sequences of commands can easily be combined to scripts. This allows a very fast and flexible control during the commissioning. On the other hand, the normal operation of the detector should be via the control software and completely transparent to a (non-expert) operator. Thus the need for a flexible way (that can be adapted to spontaneous needs) arose. This requirements can be fulfilled by a DIM server running on a DCS Workernode which is a PC running a Linux operating system.

For this purpose a DIM server has been implemented which makes scripts on the workernode available via DIM. It features a DIM RPC (Remote Procedure Call) accepting the name of a script as input, executing the specified script with the given parameters on the workernode and publishing its output on the output channel.

A special script can be used to retrieve the available scripts since for security reasons only those scripts placed in a special directory are accessible in this way.

The source code of this server is available in the TRD subversion repository [34] as package dim2shell.

4.7 Developments during cosmic runs

As part of the commissioning of the experiment with all detectors there have been several cosmic runs which were dedicated to data-taking with as many detectors combined as possible. Besides the proof of combined operation, these runs are used to gather reference data for alignment and calibration from traversing cosmic particles.

Due to the trigger setup for cosmic tracks in ALICE (ACORDE on top of the magnet) the number of useful events in the TRD with such a trigger is rather low. Thus a special trigger had to be used for these runs. The use of TOF as trigger has the advantage that it can be included in the final trigger scheme including the TRD pretrigger.

Such a trigger decision is based on coincident hits in TOF supermodules such that a track can pass the TRD at a small deflection angle. This trigger decision is produced in the TRD pretrigger system which receives the signals of all TOF supermodules. In case of a positive trigger decision the pretrigger wakes up the TRD electronics and sends the trigger as L0 input to the Central Trigger Processor (CTP). With some latency the CTP issues a L0 to all participating detectors. The pretrigger system forwards this trigger to the supermodule which starts the tracklet calculation and sends the tracklets to the GTU.

Due to the background rate (caused by the noise of the TOF modules) the fraction of events containing useful TRD tracks is rather small (on the percent level). Empty events could be suppressed by the use of a L1 decision based on the data taken after the L0. For the cosmic data taking the TRAPs were used in a special mode not calculating tracklets to be used for tracking but calculating charge sums within all their channels. If the accumulated charge is above a configurable threshold this information is shipped to the GTU. In the GTU a L1 decision is made based on the coincident occurrence of sufficiently high charges in at least 4 layers which indicates a traversing track [29].

The trigger decision has to be available at the L1 contribution time after the L0 of the CTP (which is now 236 clock cycles (25 ns)). Since the calculation is based on the information shipped as tracklets the crucial time is when the tracklets are shipped compared to the L0 trigger. The parameters entering here are the time between the pretrigger, being the relevant time reference for the calculations in the TRAP, and the L0 as well as the number of timebins. Since the tracklets are only shipped when the data is fully acquired on the TRAP the number of timebins limits the earliest possible time of shipping. As can be seen in Fig. 32 the time between the L0 and the first tracklet arriving at the GTU scales linearly with the number of

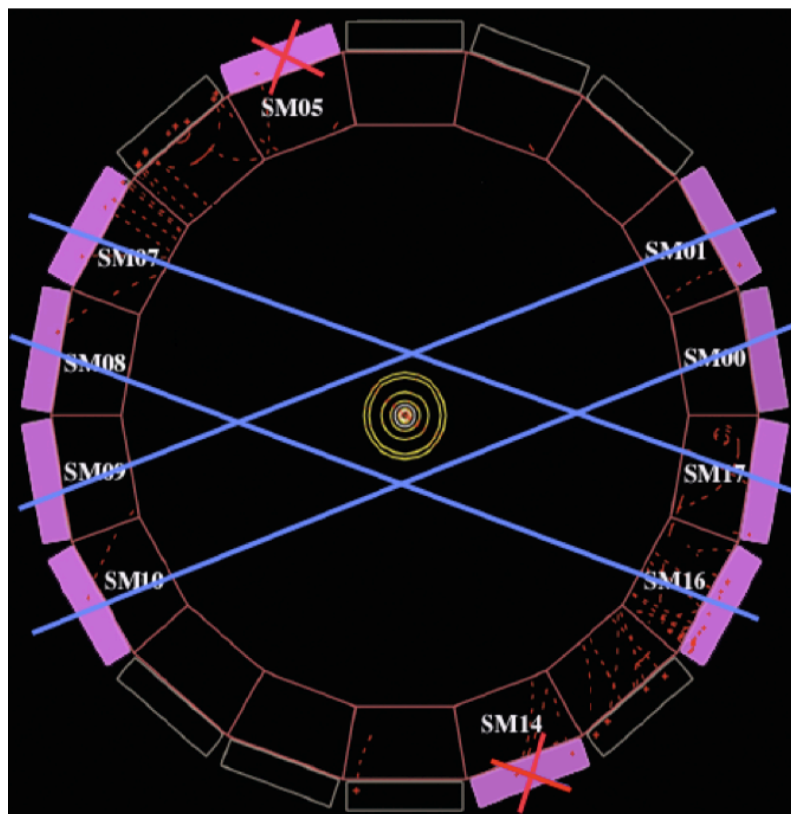


Figure 31: Coincidence condition as implemented in the pretrigger system used in the cosmic runs 2008. [24]

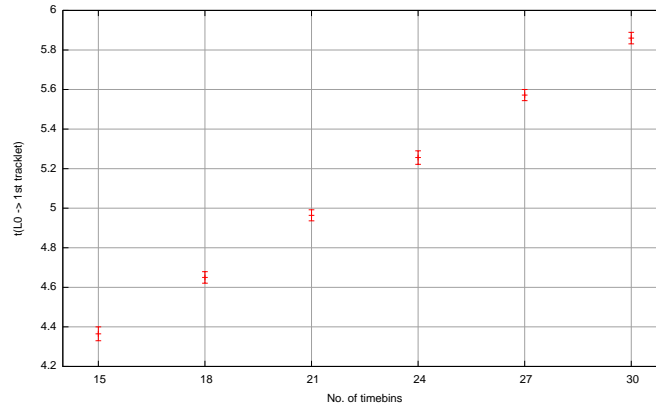


Figure 32: Dependency of the time between the first tracklet arrival at the GTU and the L0 on the number of timebins

timebins.

With this decision being based on the TRD data itself, a high purity could be achieved and this setup was used during the recent cosmic runs after the tuning of the relevant parameters.

With the above described setup the supermodule electronics has to handle a set of different scenarios of trigger sequences. For this the appropriate configuration of the relevant timings in the TRAP are essential. Within the TRAP the relevant time reference is always the arrival of the pretrigger pulse. The decision whether to start the tracklet calculation is based on the arrival of a L0 trigger. A pulse arriving at the supermodule is interpreted as L0 trigger if it comes within a certain time window after the pretrigger. Since this time depends on latencies in the CTP and pretrigger it has to be properly adjusted. The used values can be found in Table 7. This setting has also to be done for the L1 trigger which results in the shipping of the raw data¹⁰.

For the cosmic trigger to work settings on different levels have to be adjusted. On the level of the TRAP a predecision is made based on the accumulated charge within a certain time window. It is configured to contain the plateau of the pulse height (s. Fig. 7). Within this time window the charge of all found clusters (s. section 5.2) is summed. For this calculation the minimum cluster charge enters as a parameter. If this calculated sum is above a configurable threshold and the number of hits is also above a threshold the summed charge and the number of hits is sent encoded in a tracklet word. Due to the limited bit width of this word the charge is not shipped with full resolution but is right-shifted by a configurable amount. The used parameters are summarized in table 8.

With the TRD sending a L0 trigger to the CTP there is another complication.

¹⁰In a special mode (autotrg) the absence of the L0/L1 triggers is ignored to allow running without a pretrigger system.

Time	Value	TRAP register	Setting
PT \rightarrow L0	1.108 μ s	SML0	0x85
PT \rightarrow L1	7.708 μ s	SML2	0x39d
Window	83 ns	SMMODE (3..0)	0xa

Table 7: TRAP trigger timing settings as used in the 2008 run. The L0 and L1 are expected at the specified time after the pretrigger. The values have to be set in TRAP clock cycles (120 MHz).

Parameter	TRAP register	value
start of charge accumulation	TPQS1	8
end of charge accumulation	TPQE1	25
cluster charge threshold	TPHT	$30 \cdot 4 + 3 \cdot 10 \cdot 4$
charge threshold	C10CPU3 (23..8)	350
hit threshold	C10CPU3 (7..3)	4
charge shift	C10CPU3 (2..0)	4

Table 8: TRAP settings for the use in the cosmic trigger during the cosmic runs in September 2008

The triggers received by the CTP must be all aligned such that the triggers belonging to one event arrive at the same time to the trigger logic. This requires the addition of delay lines to the fast detectors to align them with the slowest one. For the TRD pretrigger using the TOF inputs a delay of 3 LHC clock cycles had to be added to be in time with the signal generated by the TOF trigger logic.

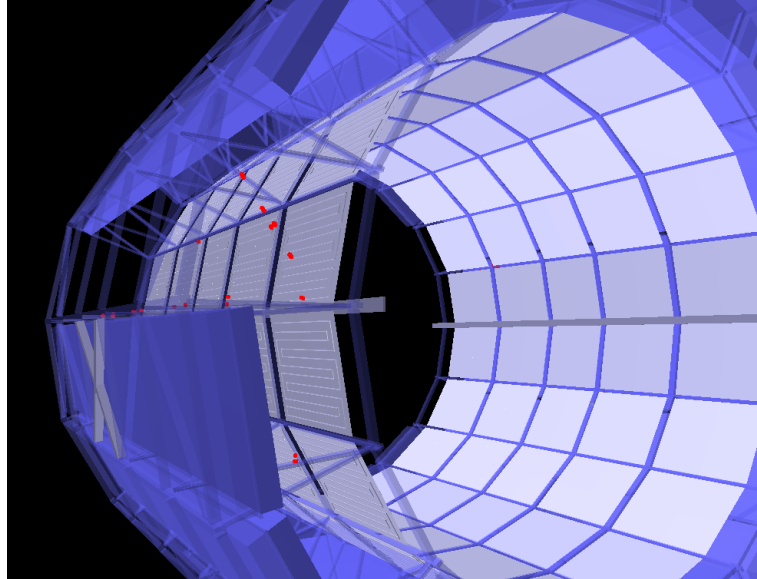


Figure 33: One of the first recorded cosmic events based on the TRD L1 trigger selected from a random L0 trigger of 10 kHz (Run 47750, event 8).

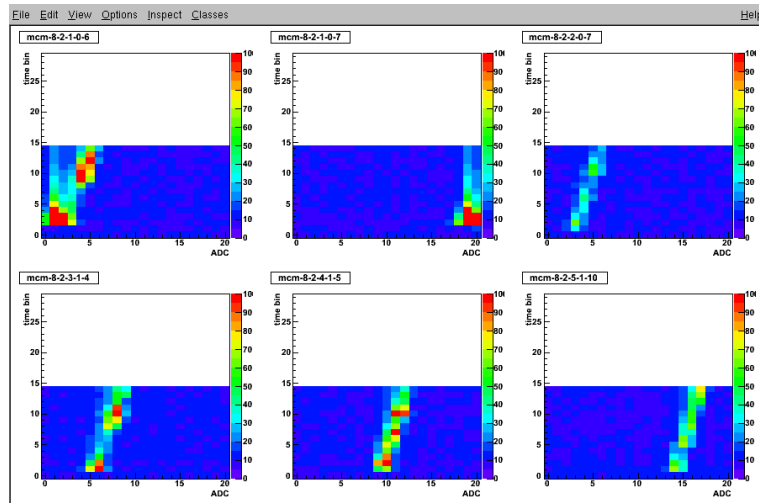


Figure 34: ADC values for a cosmic event in the affected MCMs of different layers. The track segments can be combined to make a full track (Run 47750, event 18).

5 Global tracking simulation

The design of the Transition Radiation Detector is driven by the goal to have p_T and electron identification of individual charged particles not only in the off-line reconstruction but also as input for a fast trigger logic. This allows to select events containing high p_T particles and/or electrons at an early stage of data-taking but imposes the need for time-critical data processing. Nevertheless, correlations between different tracks, such as the invariant mass of a pair of identified electrons, are planned to be used to trigger on events with leptonic decays of J/Ψ and Υ . Being based on tracks, the exact algorithm used for the trigger decision, which is implemented in re-programmable hardware, is flexible and can be adapted to arising needs. It is also foreseen to use the TRD as jet trigger based on charged particle tracks in the full central barrel acceptance.

The L1 trigger contribution based on the previously reconstructed tracks must be issued a few μs after the interaction. But reliable PID and sufficiently accurate p_T reconstruction are not possible with the local data of individual chambers. Thus, the trigger logic must combine and process the data from all layers. This need is reflected in the Front-End Electronics of the detector as well as the readout scheme with the Global Tracking Unit (GTU). To transfer the information for the trigger logic, the same interfaces as for the raw data readout are used.

The following section describes first the idea of the underlying track reconstruction as used for the trigger logic [17]. The subsequent sections explain the stages of the processing in more detail and discuss the integration of the tracking simulation into the ALICE off-line framework AliRoot.

5.1 Idea of the tracking algorithm

Due to the time constraints, the tracking cannot be based on the full raw data since its readout and processing would take too long. In order to reduce the latency due to computing and data transfer time all necessary calculations have to be as parallel and early in the readout chain as possible

The first stage of the calculation is performed by the Front-End Electronics, i. e. the MCMs. This comprises the cluster detection from the acquired ADC data and, subsequently, a straight line fit through the clusters of two neighbouring pads to describe the local track segment. Then, the information necessary to be transferred is only the resulting parameters, i. e. the y - and z -position as well as the deflection in the transverse plane. Additionally, PID information is calculated from the accumulated charge within two time windows. The information of the tracklet is encoded in a 32-bit word and, as soon as available, shipped via the optical readout to the Global Tracking Unit (GTU). To reduce the latency this transmission has no handshaking or flow control. The implementation of a fixed readout order allows a tracking algorithm which can start before the arrival of all tracklets.

In the GTU, the tracklets from different layers originating from the same particle

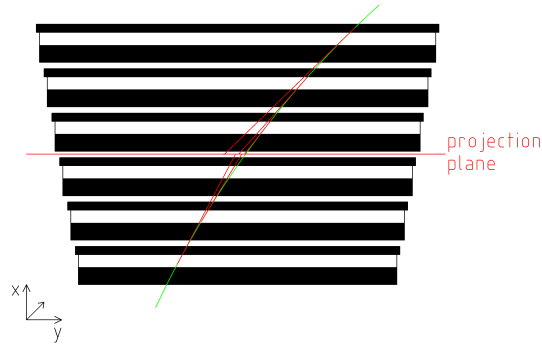


Figure 35: Trajectory of a particle through a stack of TRD chambers: The pieces in the drift volume of the chambers are detected as tracklets, characterized by their position and transverse deflection. These segments have to be recombined to a track in the tracking algorithm. They are prolonged as a straight line to the shown projection plane resulting in a projected y -coordinate.

trajectory must be matched (cmp. Fig. 35). A combinatorial approach testing all possible combinations of tracklets is not feasible for the expected multiplicities within the available time. The criterion for the tracklets to form a track is that they can be propagated to each other. The simplest assumption of a straight line is a good approximation for the desired high p_T tracks. Instead of checking the existence of other tracklets along the prolongation of a seeding tracklet, all tracklets are projected to a projection plane in the y - z -plane. The necessary calculations are independent of other tracklets. The projections of the tracklets belonging to one track will be within a small area in the projection plane. Thus, the track matching corresponds to the search of windows in the projection plane which contain more tracklets than a given threshold.

The projection is done separately in the transverse plane and the longitudinal direction. The former is realized by a unit in the GTU calculating the projected y -coordinate of the tracklets based on the deflection in the transverse plane immediately after their arrival.

In the z -direction the resolution is limited to the granularity of the 16 (12) padrows of a chamber. As the interest lies on primary tracks a vertex constraint is introduced. Based on this, the tracklets can be projected to a padrow z^{proj} in one layer chosen as reference (Layer 2 is used). Allowing a finite window around the primary vertex the projection is not unique but can result in up to three successive padrows in the reference layer for a vertex size of ± 20 cm. Thus, for every incoming tracklet up to three different z^{proj} can occur. For technical reasons, three z -channels are introduced. A tracklet is assigned to z -channel $z^{\text{proj}} \bmod 3$ with an index $z^{\text{proj}}/3 + 1$ for all possible values of z^{proj} ¹¹. Thus, a tracklet can occur in several z -channels,

¹¹Here an integer division is applied.

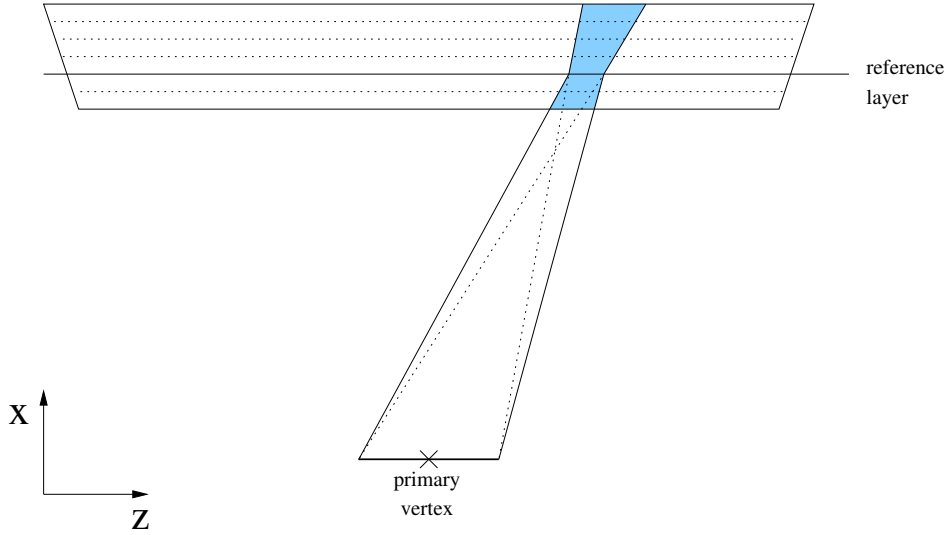


Figure 36: All tracklets potentially belonging to a track pointing to the primary vertex are grouped. The further matching is performed only within these groups. The figure is not to scale.

but only once in each.

The track matching is then limited to the groups of tracklets which can be prolonged to a specific padrow in the chosen reference layer (s. Fig. 36).

The tracklet words are part of the raw data stream and, thus, also available for off-line analysis. For the default off-line tracking the full raw data is used because it contains more information. The availability of the tracklets permits their comparison to off-line reconstructed tracklets and the simulation of the tracking algorithm as sketched above in software. This allows a full and reliable trigger simulation on the basis of real data.

5.2 Tracklets

This section reviews the tracklet calculation in the TRAPs as being the basis of the global tracking.

A particle traversing a TRD chamber can be detected by its energy deposition within the active volume of the detector as described in section 2.1. The pads of the cathode plane are connected to the PASA inputs.

As shown in Fig. 37, the signals of the 18 PASA-channels within one MCM and 2/1 channels connected from the neighbouring MCMs are digitized and digitally filtered. Subsequently, the data is processed timebin-wise in the tracklet preprocessor. First, the values are scanned for clusters by checking the following conditions:

$$Q_{i-1}(t) \leq Q_i(t), \quad (12)$$

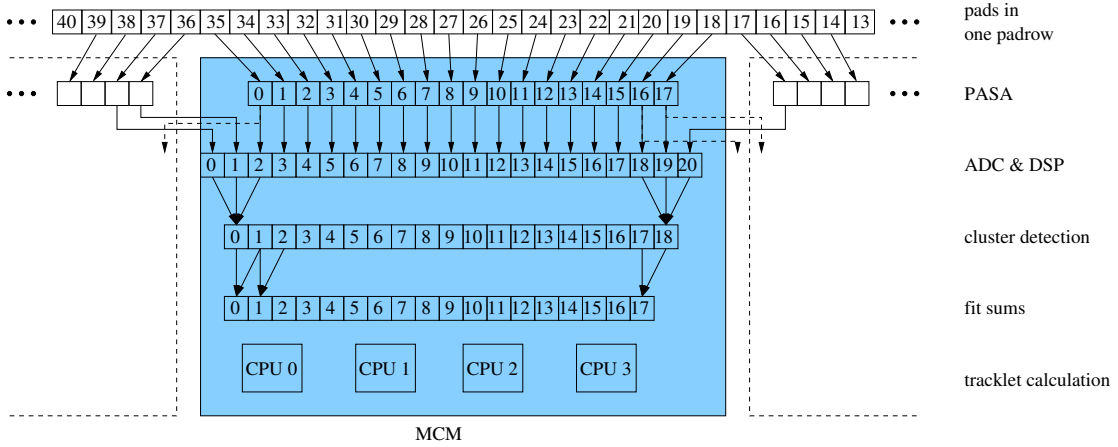


Figure 37: The signal from the pad plane is amplified and shaped. The PASA output is connected to the ADC whereby the border channels are shared with the neighbouring MCM such that also tracklets at the MCM borders can be found. The digitized data is searched for clusters. Subsequently, fit sums are calculated. Finally the four CPUs calculate the parameters for the four most promising tracklet candidates.

$$Q_i(t) > Q_{i+1}(t) , \quad (13)$$

$$Q_{i-1}(t) + Q_i(t) + Q_{i+1}(t) > T_{\text{Hit}} \quad (14)$$

where $Q_i(t)$ denotes the ADC value in channel i and timebin t (including the pedestal) which corresponds to the charge detected on the connected pad. Thus, a channel is marked as containing a cluster if it is a local maximum (Eqns. (12) and (13)) and the charge sum of the pad and its two neighbours is above the threshold T_{Hit} (Eqn. (14)). If more than four clusters are found for a timebin, they are sorted with respect to their total charge and only the four best are further processed. In case of more than 6 found clusters only the three leftmost and the three rightmost with respect to the channel number enter the sorting procedure. For the accepted clusters a shape cut can be applied where $\tilde{Q}_i(t)$ refers to the pedestal corrected charge:

$$\frac{\tilde{Q}_{i+1}(t) \cdot \tilde{Q}_{i-1}(t)}{\tilde{Q}_i(t)^2} < T_Q . \quad (15)$$

This should be used to suppress overlapping clusters. For the accepted clusters the estimated centroid position is calculated similar to the center of gravity:

$$\text{COG} = \frac{|\tilde{Q}_{i+1}(t) - \tilde{Q}_{i-1}(t)|}{\tilde{Q}_i(t)} . \quad (16)$$

This quantity is uniquely related to the cluster position by the pad response function $\text{PRF}(y)$:

$$\text{COG}(y) = \frac{|\text{PRF}(y+1) - \text{PRF}(y-1)|}{\text{PRF}(y)} . \quad (17)$$

Due to the symmetry of the pad response function the absolute value is sufficient to produce a lookup table from which the final y -position can be deduced:

$$y^{\text{rec}} = \frac{1}{2} \cdot \text{COG} + \text{LUT}(\text{COG}) . \quad (18)$$

The sign is added again in the end.

The tracklet calculation is based on positions of the clusters within two adjacent pads (s. 4th row in Fig. 37). For them a linear fit is calculated:

$$y(t) = a + b \cdot t \quad (19)$$

where the timebin is used instead of the x -coordinate. The relevant sums needed for the fit calculation:

$$\sum_t x(t) \quad (20)$$

$$\sum_t x(t)^2 \quad (21)$$

$$\sum_t y(t) \quad (22)$$

$$\sum_t y(t)^2 \quad (23)$$

$$\sum_t x(t)y(t) \quad (24)$$

$$\sum_t 1 \quad (25)$$

are accumulated for each tracklet candidate during scanning through the timebins within a given window $[t_s, t_e]$. This should be chosen to contain the plateau of the pulse (s. Fig. 7).

When all timebins have been processed, for up to four tracklet candidates (chosen by number of hits) the fit parameters that have passed the threshold for the number of hits:

$$N_i > T_{\text{CL}} , \quad (26)$$

$$N_i + N_{i+1} > T_{\text{CT}} \quad (27)$$

are calculated in the four CPUs of the TRAP which are then translated into the y -position and the deflection length d_y (s. Fig. 38). Because the deflection length as shipped in the tracklet word must correspond to a drift length of 3 cm, the drift velocity has to be known in this step and, thus, is part of the configuration settings. Table 9 gives an overview of relevant TRAP settings.

Since the tracklet calculation relies on the sub-pad resolution in the position calculation, the proper settings for the filter stages is quite important. Especially

5 GLOBAL TRACKING SIMULATION

Parameter	Variable	TRAP register	Setting
hit charge threshold	T_{Hit}	TPHT	$3 \cdot T_{\text{Hit}} \cdot 4 + P \cdot 4$
transformed pedestal	Q_{ped}	TPFP	$P \cdot 4$
cluster verification threshold	T_Q	TPVT	
first timebin for fit	t_s	TPFS	t_s
last timebin for fit	t_e	TPFE	$t_e + 1$
min. no. of clusters in left channel	T_{CL}	TPCL	T_{CL}
min. no. of total clusters	T_{CT}	TPCT	T_{CT}
first timebin for charge sum Q_0	$t_s^{Q_0}$	TPQS0	$t_s^{Q_0}$
last timebin for charge sum Q_0	$t_e^{Q_0}$	TPQE0	$t_e^{Q_0} + 1$
first timebin for charge sum Q_1	$t_s^{Q_1}$	TPQS1	$t_s^{Q_1}$
last timebin for charge sum Q_1	$t_e^{Q_1}$	TPQE1	$t_e^{Q_1} + 1$

Table 9: TRAP registers relevant for tracklet calculation. The multiplication by 4 is needed due to the internal extension of the values by two binary digits.

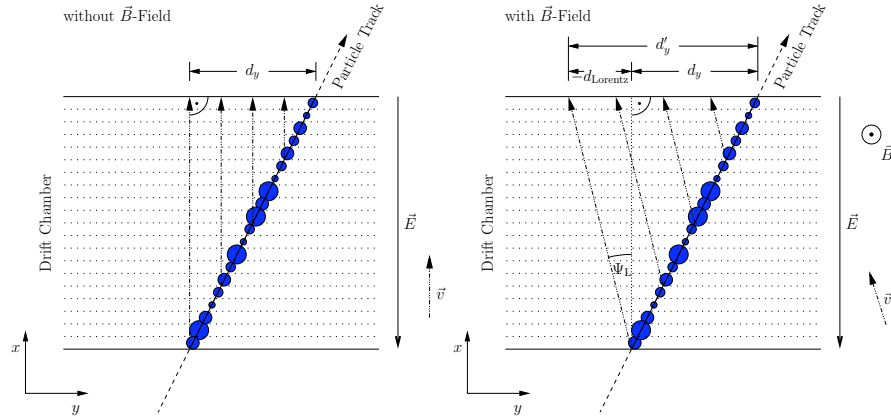


Figure 38: Tracklet without and with magnetic field

the tail cancellation filter is necessary to minimize the time correlation which leads to distortions of the cluster position for the later timebins.

The axial magnetic field leads to an angle between the drift direction and the chamber normal, the so-called Lorentz angle Ψ_L . Therefore the above calculated deflection length has to be corrected by a Lorentz length (s. Fig. 38). This has to be configured according to the actual magnetic field.

The tracklet information is encoded in a 32-bit word composed as shown in Table 10. As z -position the padrow is used, whereas y and the deflection length are calculated from the fit results. The PID information is generated from the accumulated charges in the two time windows $[t_s^{Q_0}, t_e^{Q_0}]$ and $[t_s^{Q_1}, t_e^{Q_1}]$.

As the above discussion shows, the tracklet calculation is limited to two adjacent pads and optimized for high- p_T tracks. An additional cut on the angle to the vertex

variable	integral range	granularity	physical range
y	-4096..4095	160 μm	-655.4..655.2 mm
d	-64..63	140 μm	-8.96..8.82 mm
z	0..15	1 row	0..15
PID	0..255	$\frac{1}{255}$	0..1

$$\underbrace{pppp : pppp}_{\text{PID}} : \underbrace{zzzz}_z : \underbrace{dddd : ddd}_{\text{deflection}} \underbrace{y : yyyy : yyyy : yyyy}_{\text{y-position}}$$

Table 10: Information in the 32-bit tracklet word

direction, corresponding to a p_T -cut of 2.3 GeV/c, is applied to reduce the number of tracklets to be shipped and further processed. Technically, this is a y -dependent cut on the deflection length (applied in the TRAP assembler program for the CPUs).

5.3 Tracking simulation

The aim of the tracking simulation is to reproduce the results of the hardware implementation in software. This is wanted as an easy and reproducible environment for the tuning and testing of the parameters relevant for the tracking and trigger decision on simulated and real data in an off-line analysis. A comparison of the results from the simulation and from the VHDL implementation for given input data is needed for the validation.

The data of each stack is processed by one Track Matching Unit (TMU). In the following the processing stages of the calculation are explained following the general idea presented in section 5.1. The structure of the hardware implementation for the track matching in the TMU is shown in Fig. 39: There is one input unit per layer which merges the tracklets from the two half-chambers and calculates the quantities needed for the tracking. The z -channel units assign the tracklets to the different z -classes with the proper index. In the track finder the tracklets are matched and combined to tracks. This is done in parallel for the three z -channels and different reference layers. Therefore, tracks may be found more than once and a merging unit is needed to reject multiple occurrences of the same track. For the resulting tracks the transverse momentum is calculated.

Instead of using floating point values, the simulation also uses a signed integer representation as in the hardware implementation. In all following discussions integral variables (as opposed to real ones expressed in physical units) are marked by a hat and, if relevant, the bit width is indicated in square brackets. Signed integers are expressed in the two's complement representation.

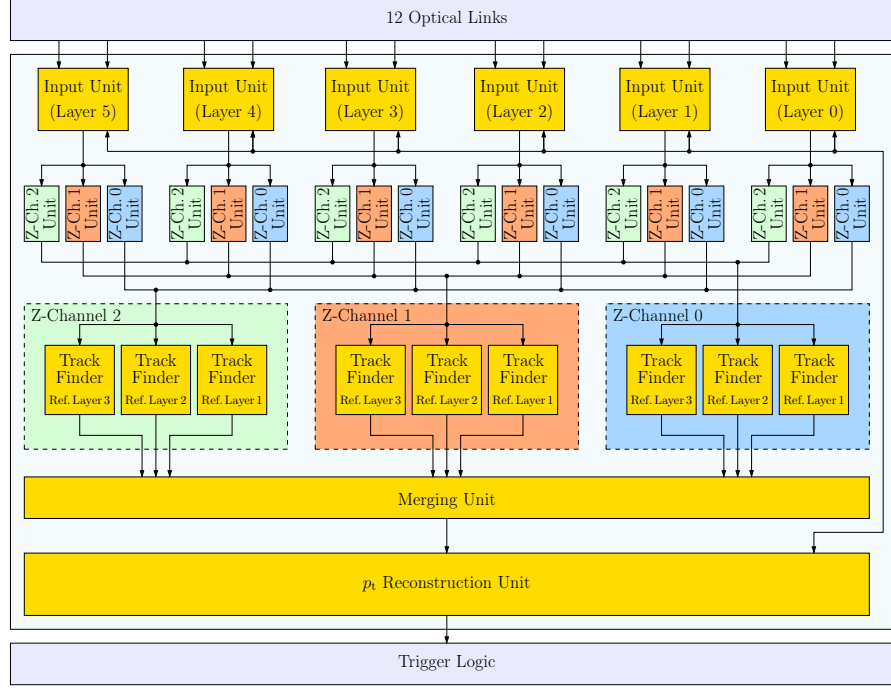


Figure 39: Overview of tracking stages [17]

5.3.1 Input units

The task of the input units is to perform all possible pre-calculations for the tracking immediately after the arrival of the tracklets. This comprises the projected y -coordinate y^{proj} , the angle to the vertex direction in the transverse plane and the tilted-pad aware y' .

The tracklets are prolonged in the x - y -plane to the projection plane (given by x_{mid}) assuming a straight line (s. Fig. 40) with the initial y -coordinate y and the deflection length d_y :

$$y^{\text{proj}} = y - (x_L - x_{\text{mid}}) \cdot \frac{d_y}{l_{\text{Drift}}} = y - d_y \cdot \underbrace{\frac{x_L - x_{\text{mid}}}{l_{\text{Drift}}}}_{C^{y_{\text{proj}}}} \quad (28)$$

where only y and d_y are tracklet-specific quantities. The constant $C^{y_{\text{proj}}}$ is statically pre-calculated depending only on the x -coordinate of the layer x_L and projection plane x_{mid} and the driftlength l_{Drift} which are fixed values in each input unit.

The resolution of the projected y -position is chosen to be lower due to the lower resolution of the deflection length. The following formula shows the above calculation as done on the integer level:

$$\hat{y}_L^{\text{proj}}[10] = \left(\left(\left(\hat{y}[13] + (\hat{d}_y[7] \cdot \hat{C}_L^{y_{\text{proj}}}[8]) \cdot \frac{1}{2^e} \right) \cdot \frac{1}{2^2} \right) + 1 \right) \cdot \frac{1}{2} \quad (29)$$

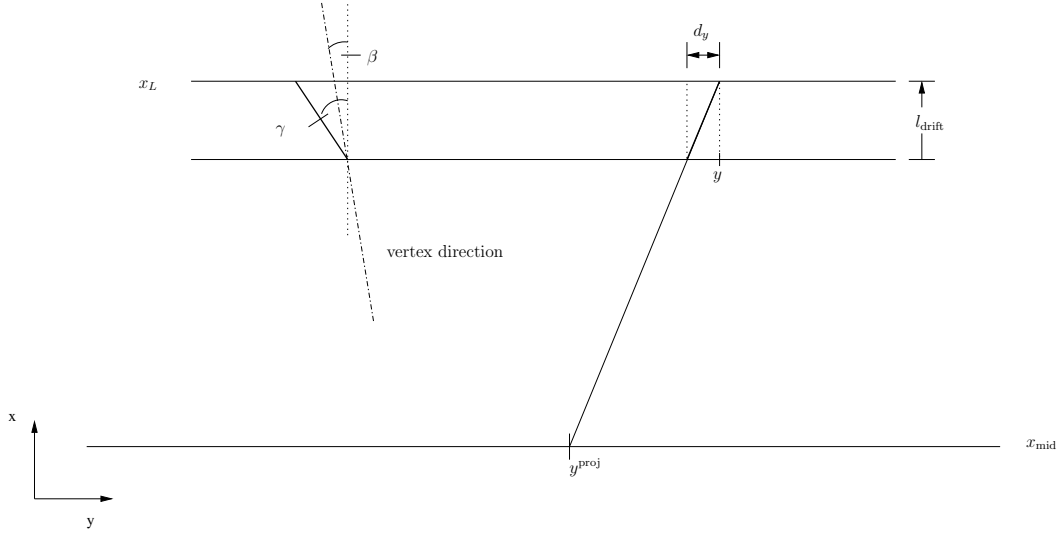


Figure 40: The tracklet is projected in the transverse plane assuming a straight line. Furthermore, the angle to the vertex direction is calculated.

Variable	Symbol	value
x of layer 5	x_5	363.6 cm
x of layer 4	x_4	351.0 cm
x of layer 3	x_3	338.5 cm
x of layer 2	x_2	325.9 cm
x of layer 1	x_1	313.3 cm
x of layer 0	x_0	300.6 cm
x of projection plane	x_{mid}	332.1 cm

Table 11: Supermodule measures used in the calculations (taken from the AliRoot geometry)

where $\hat{C}_L^{y_{\text{proj}}}$ is the constant $C^{y_{\text{proj}}}$ adapted to the integer values with the index L indicating the layer of the tracklet:

$$C_L^{y_{\text{proj}}} = \frac{d_{\text{res}}}{y_{\text{res}}} \cdot \frac{x(L) - x_{\text{mid}}}{l_{\text{Drift}}} \cdot 2^e \quad (30)$$

with e excess bits needed for the multiplication. d_{res} and y_{res} refer to the granularities of d_y and y , respectively, and are needed for the adaptation to the used integer representation.

Besides the projected y -coordinate, the input unit also calculates the angle of the tracklet with respect to the vertex direction. As can be seen in Fig. 40 this angle is given by:

$$\alpha = \gamma - \beta \quad (31)$$

$$= \arctan \frac{d_y}{l_{\text{Drift}}} - \arctan \frac{y}{x_L} \quad (32)$$

$$\approx \frac{d_y}{l_{\text{Drift}}} - \frac{y}{x_L} . \quad (33)$$

This shows that the natural unit for this angle is:

$$\alpha_{\text{res}} = \frac{d_{\text{res}}}{l_{\text{Drift}}} \approx 4.67 \cdot 10^{-3} \approx 0.267^\circ . \quad (34)$$

Thus, the integer-valued angle is calculated by:

$$\hat{\alpha}[7] = (((\hat{d}[7] \cdot 2) - ((\hat{y}[13] \cdot \frac{1}{24}) \cdot \hat{C}_L^\alpha[9]) \cdot \frac{1}{2^{10}}) + 1) \cdot \frac{1}{2} . \quad (35)$$

with the constant $\hat{C}_L^\alpha[9]$:

$$\hat{C}_L^\alpha[9] = \frac{l_{\text{Drift}}}{x_L} \cdot \frac{y_{\text{res}}}{d_{\text{res}}} \cdot 2^{15} \quad (36)$$

The third quantity calculated by the input unit is the tilted pad-aware y -position y' which is needed for the p_T -reconstruction of the found tracks. The following calculation will be justified in section 5.3.5:

$$y' = y - (-1)^l z_{l,\text{row}} \cdot \tan(\beta_{\text{tilt}}) \quad (37)$$

with the z -coordinate of the corresponding pad $z_{l,\text{row}}$ (middle of the pad). The integral expression is given by:

$$\hat{y}'[13] = \hat{y}[13] - (-1)^L \frac{z_{L,\text{row}} \cdot \tan(\beta_{\text{tilt}})}{y_{\text{res}}}[13] . \quad (38)$$

5.3.2 z -Channel-Units

In the z -channel units the tracklets are preselected according to their z position and grouped in sets possibly forming primary tracks. The prolongation of the tracklets in the longitudinal direction cannot be based on local tracking information but solely on the vertex constraint. The projection to padrows in one chosen reference layer is not unique when allowing a window around the interaction point. As discussed above, three different z -channels are introduced.

The range of padrows to which a tracklet can be projected follows from purely geometrical considerations (s. Fig. 36). A lookup table is produced which contains for each z -channel c_z , padrow z and layer L to which padrow in the reference layer z^{proj} it is prolonged. This mapping is unique within each z -channel. The further tracking requires a $z_{\text{idx}}-y^{\text{proj}}$ -sorted sequence of tracklets from all layers which can be achieved in each z -channel.

After the assignment of the tracklets to the z -channels they are fed to the next stage, in which tracks in each of the classes are searched for in parallel.

The map as generated by the simulation code based on the AliRoot geometry is partially shown in Fig. 41 and listed in the appendix.

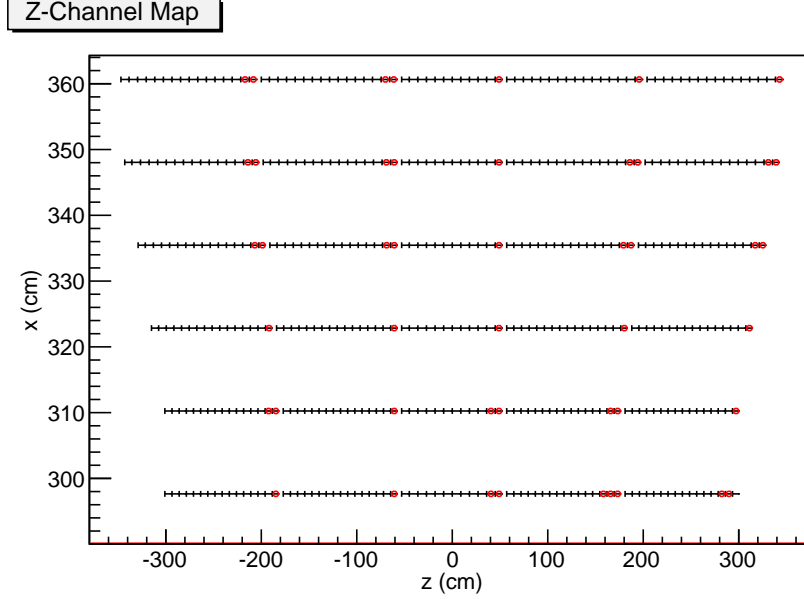


Figure 41: The z -channel map is calculated from the TRD geometry as implemented in AliRoot. The figure shows the position of the individual pads where the ones of z -channel 0 and subchannel 1 are marked by red circles. It can be seen that up to three successive rows can belong to one class.

5.3.3 Track matching

The track matching is designed to avoid combinatorial approaches. Starting from the ordered lists, two tracklets per layer (referred to as A and B) are checked in parallel. The first tracklet from a specified reference layer is used to calculate the range of y^{proj} and α in which the parameters of tracklets from other layers must lie to form a hit. The range is calculated using the configurable window sized Δy and $\Delta\alpha$:

$$y_A^- = y_{L_{\text{ref}},A}^{\text{proj}} - \Delta y \quad (39)$$

$$y_A^+ = y_{L_{\text{ref}},A}^{\text{proj}} + \Delta y \quad (40)$$

$$\alpha_A^- = \alpha_{L_{\text{ref}},A} - \Delta\alpha \quad (41)$$

$$\alpha_A^+ = \alpha_{L_{\text{ref}},A} + \Delta\alpha \quad (42)$$

$$y_B^- = y_{L_{\text{ref}},B}^{\text{proj}} - \Delta y \quad (43)$$

$$y_B^+ = y_{L_{\text{ref}},B}^{\text{proj}} + \Delta y . \quad (44)$$

For the other layers, only simple comparisons are needed:

$$\begin{aligned} \text{Hit}_{L,A} &= \neg(z_{L,A}^{\text{idx}} < z_{L_{\text{ref}},A}^{\text{idx}} \vee ((z_{L,A}^{\text{idx}} = z_{L_{\text{ref}},A}^{\text{idx}}) \wedge (y_{L,A}^{\text{proj}} \leq y^-))) \wedge \quad (45) \\ &\neg(z_{L,A}^{\text{idx}} \geq z_{L_{\text{ref}},A}^{\text{idx}} \vee ((z_{L,A}^{\text{idx}} = z_{L_{\text{ref}},A}^{\text{idx}}) \wedge (y_{L,A}^{\text{proj}} \geq y^+))) \wedge \end{aligned}$$

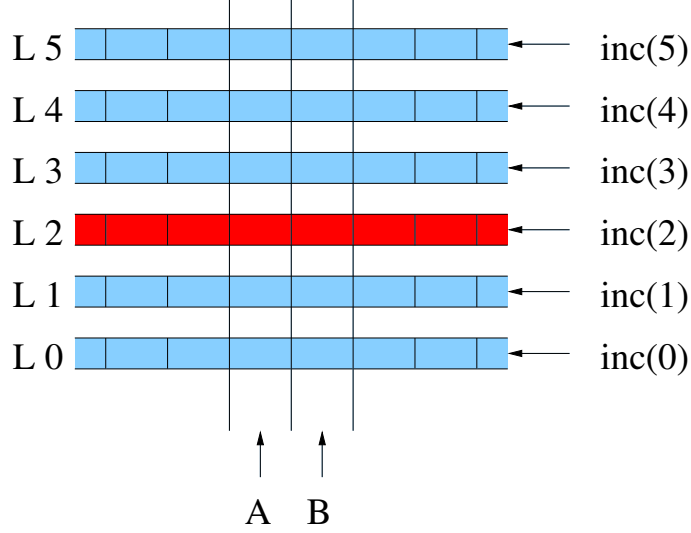


Figure 42: The ordered lists of tracklets are sequentially searched for tracks. In each layer two tracklets A and B are active and compared to the reference layer (red). In each step the lists are shifted such that in the end all tracklets are searched.

$$\begin{aligned}
 & \neg(\alpha_{L,A} < \alpha^-) \wedge \\
 & \neg(\alpha_{L,A} > \alpha^+) \\
 \text{Hit}_{L,B} = & \neg(z_{L,B}^{\text{idx}} < z_{L_{\text{ref}},A}^{\text{idx}} \vee (z_{L,B}^{\text{idx}} = z_{L_{\text{ref}},A}^{\text{idx}} \wedge y_{L,B}^{\text{proj}} \leq y^-)) \wedge \\
 & \neg(z_{L,B}^{\text{idx}} \geq z_{L_{\text{ref}},A}^{\text{idx}} \vee (z_{L,B}^{\text{idx}} = z_{L_{\text{ref}},A}^{\text{idx}} \wedge y_{L,B}^{\text{proj}} \geq y^+)) \wedge \\
 & \neg(\alpha_{L,B} < \alpha^-) \wedge \\
 & \neg(\alpha_{L,B} > \alpha^+)
 \end{aligned} \tag{46}$$

$$\text{Aligned}_{L,A} = \neg(z_{L,A}^{\text{idx}} < z_{L_{\text{ref}},A}^{\text{idx}} \vee (z_{L,A}^{\text{idx}} = z_{L_{\text{ref}},A}^{\text{idx}} \wedge y_{L,A}^{\text{proj}} \leq y^-)) \tag{47}$$

$$\text{WayBeyond}_L = \neg(z_{L,A}^{\text{idx}} > z_{L_{\text{ref}},B}^{\text{idx}} \vee (z_{L,A}^{\text{idx}} = z_{L_{\text{ref}},B}^{\text{idx}} \wedge y_{L,A}^{\text{proj}} > y_{L_{\text{ref}},B}^{\text{proj}} + \Delta y)) \tag{48}$$

where $\text{Hit}_{L,A}$ and $\text{Hit}_{L,B}$ indicate whether tracklet A and B, respectively, in layer L could belong to a track with the reference tracklet A, i. e. the parameters are within the feasible range. The comparison of the z_{idx} ensures that only tracklets of the same z_{idx} are matched.

The variable $\text{Aligned}_{L,A}$ shows whether the shifting of this layer is sufficiently progressed compared to the reference tracklets as the shifting is only one-directional.

The last variable tests whether the active tracklets in this layer are such that the current position of the reference layer cannot lead to a hit in this layer anymore.

From these quantities the following sums are calculated:

$$N_{\text{Hits}} = \# \{L \mid \text{Hit}_{L,A} = 1 \vee \text{Hit}_{L,B} = 1\} \tag{49}$$

$$N_{\text{uncertain}} = \# \{L \mid \text{Aligned} \neq 1\} \tag{50}$$

$$N_{\text{WayBeyond}} = \# \{L \mid \text{WayBeyond} = 1\} . \tag{51}$$

N_{Hits} indicates in how many layers a hit has been observed. If the number of mis-aligned layers $N_{\text{uncertain}}$ is non-zero, this implies that the shifting of some layers could bring other tracklets into visibility such that more hits are found. If there are no mis-aligned layers and the number of hits is at least four, a track is found and registered with the references to the contributing tracklets — if both the A and B tracklet are a hit, A is chosen.

In any case, the information about the alignment and the possibility of finding a track with the actual position of the reference layer is used to calculate the shift of each layer. If the number of misaligned layers is non-zero and a hit with this reference layer position is still possible, i. e.:

$$N_{\text{Hits}} + N_{\text{uncertain}} \geq 4 \quad (52)$$

the reference layer is kept. In this case the other layers are shifted such that they get aligned.

The procedure is finished when all layers are shifted to its end. In the above considerations a non-existing tracklet at the end of the list is considered to be larger than any other tracklet, such that it is always aligned and never leads to a hit.

As this method can only find such tracks with a tracklet in the reference layer, three instances of the Track Finder with different reference layers are needed to find all tracks with at least 4 contributing tracklets.

5.3.4 Merging and Unification

Due to the parallel search one track can be found up to nine times. Equal tracks, i. e. those with equal contributing tracklets, have to be discarded in order not to produce wrong results by counting tracks twice. This procedure is done in several steps. First, the tracks from the three reference layer matching units within each z -channel are merged. This is done by sorting the tracks from the three units in ascending order with respect to the following comparison:

$$a < b : \Leftrightarrow z_A^{\text{idx}} < z_B^{\text{idx}} \vee z_A^{\text{idx}} = z_B^{\text{idx}} \wedge y_A^{\text{approx}} < y_B^{\text{approx}} . \quad (53)$$

With this ordering the tracks from one trajectory will be in successive order. Thus, by placing a unification unit after the merging unit which checks for the equality of any two subsequent tracks and, in the case of two equal ones, discards the one with fewer hits, all double tracks from the three reference layers can be avoided.

The next stages remove multiple tracks from the three different z -channels. Here, it is not possible to find a sorting such that equal tracks are necessarily successive. This is caused by the fact that a tracklet can be projected to up to three successive padrows z^{proj} . Therefore the tracks are first sorted and merged with respect to (with z -channel c_z):

$$k = \left\lfloor \frac{z_{\text{ch}} + 3 \cdot z_{\text{idx}}}{2} \right\rfloor - 1 \quad (54)$$

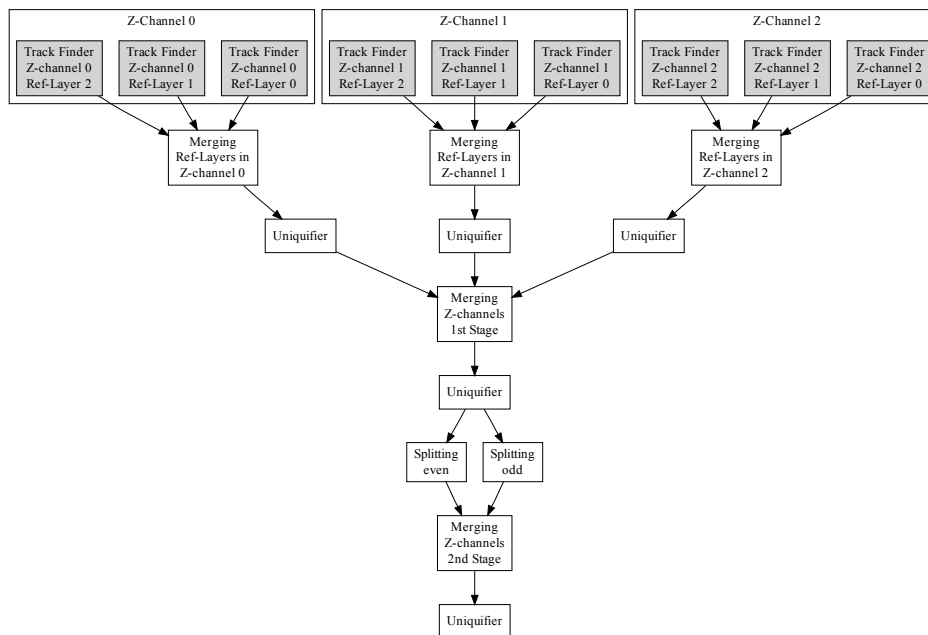


Figure 43: The tracks found in the parallel finding units are merged and unified in several stages.

and unquified. Subsequently, the tracks are split with respect to:

$$z_{\text{row}} \bmod 2 \quad (55)$$

and re-merged:

$$k_2 = \left\lfloor \frac{z_{\text{row}}}{2} \right\rfloor. \quad (56)$$

As Table 12 shows this leads to a situation in which equal tracks would end up successively in at least one of the two stages.

5.3.5 p_T -reconstruction

The transverse momentum p_T of a traversing particle can be calculated from the curvature of its trajectory in the axial magnetic field. The full reconstruction of a circle through all tracklets is too time-consuming. Instead, the computation is simplified and the track is considered a straight line within the TRD (as it has already been assumed for the track matching).

Thus, a straight line fit through all the contributing tracklets of a track has to be performed within the transverse plane. For this straight line fit the following parametrization could be anticipated:

$$y = a + b \cdot x \quad (57)$$

z^{proj}	z_{ch}	z_{idx}	k	k_2
0	0	1	0	0
1	1	1	1	0
2	2	1	1	1
3	0	2	2	1
4	1	2	2	2
5	2	2	3	2
6	0	3	3	3
7	1	3	4	3
8	2	3	4	4
9	0	4	5	4
10	1	4	5	5
11	2	4	6	5
12	0	5	6	6
13	1	5	7	6
14	2	5	7	7
15	0	6	8	7

Table 12: Sorting criteria for the z -channel track merging

with the parameters a and b . However, due to the pad tilting (see 2.1) which is not taken into account in the TRAP calculation a correction is needed here:

$$y = a + b \cdot x + (-1)^L \tan(\beta_{\text{tilt}}) \cdot (z - z_{\text{row}}^{\text{middle}}) . \quad (58)$$

With the additional vertex constraint $z = c \cdot x$ (parameter c) this leads to:

$$y = a + b \cdot x + (-1)^L \tan(\beta_{\text{tilt}}) \cdot (c \cdot x - z_{\text{row}}^{\text{middle}}) \quad (59)$$

and with y' as calculated in the input unit to:

$$y' = a + b \cdot x + (-1)^L \underbrace{\tan(\beta_{\text{tilt}})c}_{c'} \cdot x . \quad (60)$$

The optimal set of parameters has to be found to represent the position of the tracklets in all layers. The minimization of χ^2 :

$$\chi^2 = \sum_L (y'_L - (a + b \cdot x_L + c' \cdot (-1)^L x_L))^2 \quad (61)$$

corresponds to the optimization problem:

$$\|\mathbf{y}' - \mathbf{A} \cdot \mathbf{u}\|_2 \stackrel{!}{=} \min_{\tilde{\mathbf{u}} \in \mathbb{R}^3} \|\mathbf{y}' - \mathbf{A} \cdot \tilde{\mathbf{u}}\|_2 \quad (62)$$

where the vector \mathbf{y}' holds the values for the tracklets in all layers:

$$\mathbf{y}' = \begin{pmatrix} y'_0 \\ y'_1 \\ y'_2 \\ y'_3 \\ y'_4 \\ y'_5 \end{pmatrix}. \quad (63)$$

The vector \mathbf{u} holds the fit parameters

$$\mathbf{u} = \begin{pmatrix} a \\ b \\ c' \end{pmatrix} \quad (64)$$

and the matrix \mathbf{A} is given by (compare to (60)):

$$\mathbf{A} = \begin{pmatrix} 1 & x_0 & x_0 \\ 1 & x_1 & -x_1 \\ 1 & x_2 & x_2 \\ 1 & x_3 & -x_3 \\ 1 & x_4 & x_4 \\ 1 & x_5 & -x_5 \end{pmatrix} \quad (65)$$

\mathbf{A} only depends on the position of the layers, i. e. the static TRD geometry. The optimization problem (62) can be translated to the normal equation:

$$\mathbf{A}^T \mathbf{A} \mathbf{u} = \mathbf{A}^T \mathbf{y}' . \quad (66)$$

Since numerical robustness is not needed (only the specific case of the TRD geometry is considered which leads to a sufficiently well-behaved matrix A) this can be solved by:

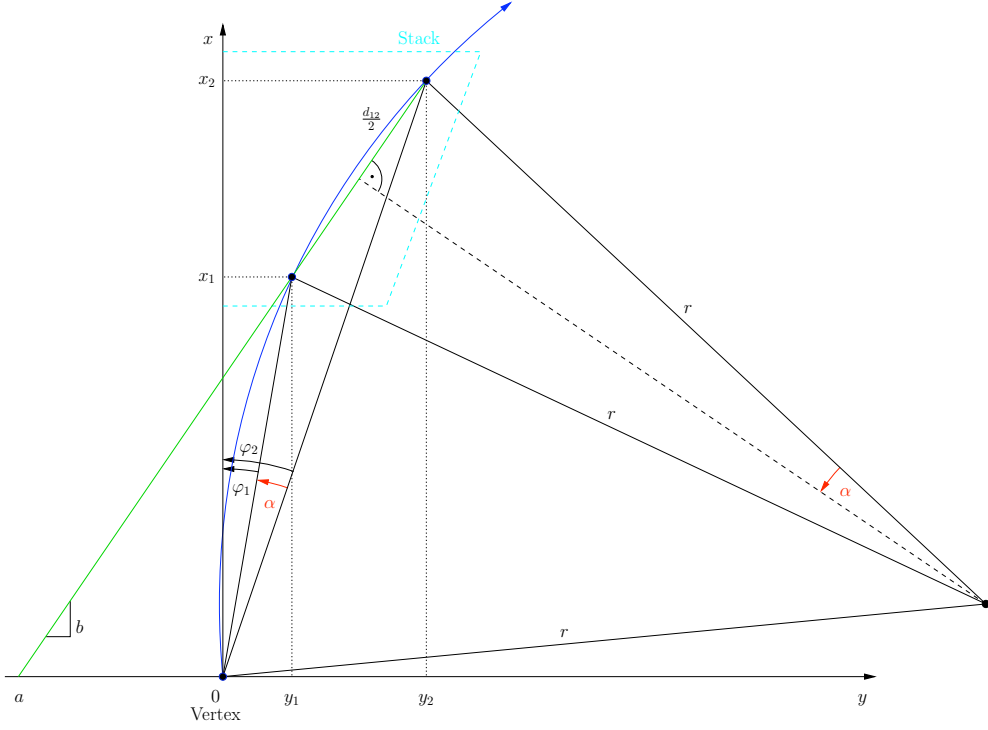
$$\mathbf{u} = \underbrace{(\mathbf{A}^T \mathbf{A})^{-1} \mathbf{A}^T}_{=: \mathbf{B}} \mathbf{y}' \quad (67)$$

where \mathbf{B} can be pre-calculated and statically stored in the hardware implementation. The calculation of the fit parameters then reduces to few multiplications and additions:

$$a = \sum_L B_{1,L}^k y'_L \quad (68)$$

$$b = \sum_L B_{2,L}^k y'_L \quad (69)$$

$$c' = \sum_L B_{3,L}^k y'_L \quad (70)$$


 Figure 44: p_T reconstruction from the straight line fit [17]

which must be calculated for every track. The index k reflects the fact that not necessarily tracklets from all layers contribute. For layers without tracklet the corresponding row in \mathbf{A} is filled with zeroes. The coefficients for the fit parameter calculation are stored for all tracklet masks with at least four tracklets.

After the parameters of the straight line are found the curvature in the magnetic field has to be deduced. As shown in Fig. 44, the particle trajectory is assumed to be a circle with constant curvature. It is intersected by the calculated straight line but the intersection points are unknown. The assumption of certain intersection points depending on the tracklet mask leads to good results [17]:

$$x_1 = x_{\text{inner}} + x_d \cdot \frac{N_{\text{Hits}} - 1}{6} \quad (71)$$

$$x_2 = x_{\text{outer}} - x_d \cdot \frac{N_{\text{Hits}} - 1}{6} \quad (72)$$

$$(73)$$

where x_1 and x_2 are the x -coordinates of the inner and outer intersection point, respectively, depending on the number of contributing tracklets N_{Hits} and the layer of the inner and outer tracklet x_{inner} and x_{outer} .

As can be seen from Fig. 44 the following calculations can be used to find the

radius [17]:

$$r = \frac{d_{12}}{2 \sin \alpha} \quad (74)$$

$$\alpha = \varphi_2 - \varphi_1 = \arctan \frac{y_2}{x_2} - \arctan \frac{y_1}{x_1} \quad (75)$$

$$y_1 = a + b \cdot x_1 \quad (76)$$

$$y_2 = a + b \cdot x_2 \quad (77)$$

$$d_{12} = \sqrt{1 + b^2}(x_2 - x_1) \approx \underbrace{\left(1 + \frac{1}{2}b^2\right)}_{=:d'_{12}}(x_2 - x_1) . \quad (78)$$

In the first stage of simplification, the radius would be calculated approximately from:

$$r' = \frac{d'_{12}}{2 \cdot (\varphi_2 - \varphi_1)} . \quad (79)$$

A Taylor expansion of α leads to:

$$\alpha = \varphi_2 - \varphi_1 = a(b^2 - 1) \cdot \frac{x_2 - x_1}{x_1 x_2} + a^2 b \cdot \frac{x_2^2 - x_1^2}{x_1^2 x_2^2} + \dots . \quad (80)$$

This results in a further simplification of the calculation:

$$r'' = c_1 \cdot \frac{\frac{b^2}{2} + 1}{a(b^2 - 1) + a^2 b c_2} \quad (81)$$

with:

$$c_1 = \frac{x_1 x_2}{2} \text{ and } c_2 = \frac{x_1 + x_2}{x_1 x_2} . \quad (82)$$

Since the values of b are small this can be written as:

$$r''' = -\frac{c_1}{a} . \quad (83)$$

5.4 Integration to Off-line Framework

The tracking simulation implements the algorithm as in the on-line electronics to combine tracklets to tracks and calculate their p_T . It shall be used for detailed studies of trigger efficiencies, purities and biases. It has been implemented in a general way such that it can be run on tracklets, i. e. track segments in individual chambers, from different sources, e. g. also off-line reconstructed tracklets.

The AliRoot off-line framework is based on ROOT [31] and comprises both simulation and reconstruction for ALICE. The latter has to run on either simulated data, in which case additional Monte-Carlo information is available and must be kept, or on real data from the detector (s. Fig. 45). The simulation of events starts

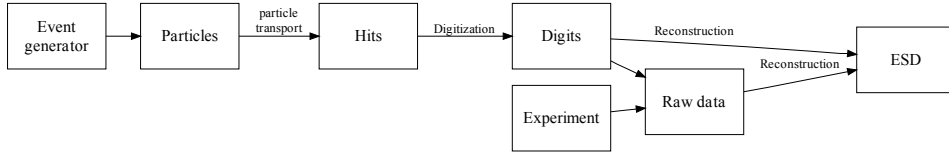


Figure 45: Simulation and Reconstruction in AliRoot

with the particles from the primary collision as generated by a Monte-Carlo event generator. Afterwards, the particles are transported through the detector geometry (using GEANT 3/4 or Fluka). In this step hits, i. e. deposited energy in the active detector volumes, are registered. They are used to calculate digitized values (digits) using the detector response. These digits are stored together with the Monte-Carlo information on their creation. This allows to deduce from which particle a certain hit was produced. The reconstruction can then either run on the digits directly or they can be translated to raw data first. In the latter case the real data format is used, such that the reconstruction is identical.

The need to run on different input data is reflected in the implementation of the tracking simulation as well. It has been added to the TRD section of AliRoot as several C++-classes:

AliTRDgtuSim: This class provides the interface to the GTU simulation and steers the other classes.

AliTRDgtuTMU: The track matching unit accepts tracklets of one stack as input and produces tracks as output.

AliTRDgtuParam: All parameters used within the tracking are centrally managed by this class.

AliTRDtrackletBase: An abstract tracklet base class is used as minimal interface for any tracklet. All deriving classes can be used as input to the tracking simulation.

AliTRDtrackletWord: This class contains only the information as available in a 32-bit tracklet word from the TRAP.

AliTRDtrackletMCM: For the tracklets produced in the TRAP simulation, additional Monte-Carlo information is stored, such as the label of the producing particle.

AliTRDtrackletGTU: This tracklet is used internally during the tracking to store intermediate results, such as the projected y -coordinate.

AliTRDtrackGTU: This track is used for the output. It contains references to the contributing tracklets and the reconstructed track information, i. e. p_T and the PID.

The abstract base class **AliTRDtrackletBase** defines the most general interface to a tracklet. Necessary information is the position of the tracklet, its deflection and its PID information which is available in integer and real representations.

In case of real data, the tracklets are calculated on the TRAP and shipped as 32-bit word before the raw data. This is the case of minimal information and is implemented as **AliTRDtrackletWord**.

During the simulation of events the tracklets can also be calculated in a TRAP model. This is done in **AliTRDmcmSim** which implements a routine to produce the tracklets from the incoming ADC data following the same steps as in the TRAP [20] (s. section 5.2). This class has been extended to produce also the Monte-Carlo labels for the tracklets and store the output as **AliTRDtrackletMCM** for further usage in a dedicated file.

The tracking simulation framework has been implemented such that it can be run on any tracklets derived from **AliTRDtrackletBase**. This allows to separate the tracklet calculation and the global tracking simulation in trigger studies. Furthermore, a comparison between on-line and off-line tracklets is possible. The tracklets are read from an intermediate storage file that is either produced during the simulation or during the reading of raw data.

The tracking simulation is controlled by one class **AliTRDgtuSim** which steers all lower level activities. This class provides several methods. *RunGTU(AliLoader*)* is used to initiate the tracking simulation. The tracklets are first loaded by *LoadTracklets(AliLoader*)* automatically from the intermediate storage file for the current event using the AliRoot data loader implementations. Subsequently, the tracking is run stack-wise. The output can either be written to a dedicated file by *WriteTreesToFile()* or added to the Event Summary Data (ESD) by *WriteTracksToESD()*. The latter version allows to run the tracking after the reconstruction and to just add the TRD tracks which reduces the turn-around times. In the first case, the tracks are stored as **AliTRDtrackGTU** which contains the full information used during the tracking. This is mainly for debugging purposes.

AliTRDgtuSim acts as interface to **AliTRDgtuTMU** in which the actual tracking for a stack is performed. This class contains all the steps described in the previous section. First the tracklets loaded in **AliTRDgtuSim** are added to the proper link of the TMU by the method *AddTracklet(AliTRDtrackletBase*, Int_t link)* where the link specifies the half-chamber in which the tracklet was found. Any tracklet deriving from **AliTRDtrackletBase** can be passed. In this step an **AliTRDtrackletGTU** is created which contains a pointer to the passed tracklet and can hold all the information that occurs during the further stages in the TMU.

After all tracklets of one stack have been added, *RunTMU(TList*)* is called. Inside the TMU class, first *RunInputUnit(Int_t layer)* is executed to perform all

precalculations. The results of these calculations are stored in the **AliTRDtrackletGTU**. Additionally, the tracklets from the two links of each layer are merged and sorted with respect to the z -row and the y -position. The next step is *RunZChannelUnit(Int_t layer)* in which the tracklets are assigned to the different z -channels by adding them to the corresponding list. The sub-channel for each z -channel in which the tracklet occurs is stored in **AliTRDtrackletGTU**. The track finding is done in *RunTrackFinder(Int_t zchannel)* for each z -channel and three reference layers. The resulting tracks are stored internally and then merged in *RunTrackMerging(TList* ListOfTracks)*. For the final list of tracks the reconstruction is called *RunTrackReconstruction(TList* ListOfTracks)* in which the p_T is assigned. By then a list of **AliTRDtrackGTU** has been produced. These tracks can now be temporarily stored and the same procedure can be repeated for further stacks. In the end the tracks can be written to disk and/or added to the Event Summary Data (ESD).

All the parameters needed in the tracking algorithm are taken from **AliTRDgtuParam** which is implemented as singleton.

The realization of the trigger within TRD is that the information the decision is based on is fully available in off-line. This makes a full trigger simulation on real events possible which is the best way to check for the appropriate trigger decisions.

5.5 Hardware Comparison

To have a full simulation of the hardware-implemented tracking is advantageous for many reasons. It allows reliable trigger studies and the tuning of the used parameters, such as trigger thresholds. But it also allows a cross-check of the results obtained on-line during the data taking. To make these comparisons as easy and significant as possible the simulation should lead to bit-equivalent results.

For first comparisons the same set of data was used as during VHDL implementation development [16]. This data originated from run 454 taken during a testbeam in 2007 at the Proton Synchrotron (PS) at CERN. Due to an improper TRAP-configuration at that time, the tracklets do not fully fulfil the specified format. To avoid changes in the tracking code which are specific to these data, the tracklets from the testbeam are pre-processed and converted to the desired format. This is done during the extraction of the tracklets from the raw data after which they are stored in a special format (ASCII file) that can be read by a testbench for the VHDL implementation and the software model (this file format is different from the above described root-file). This testbench [16] is a special interface unit which can be run in a VHDL simulation environment. It is also implemented in VHDL but not part of the code that is synthesized for the FPGAs. For these tests a functional simulation was done using ModelSim¹². The software model was extended to also read this ASCII file format and output the reconstructed tracks in the same way.

The software model has been built very close to the hardware implementation.

¹²Xilinx Edition

5 GLOBAL TRACKING SIMULATION

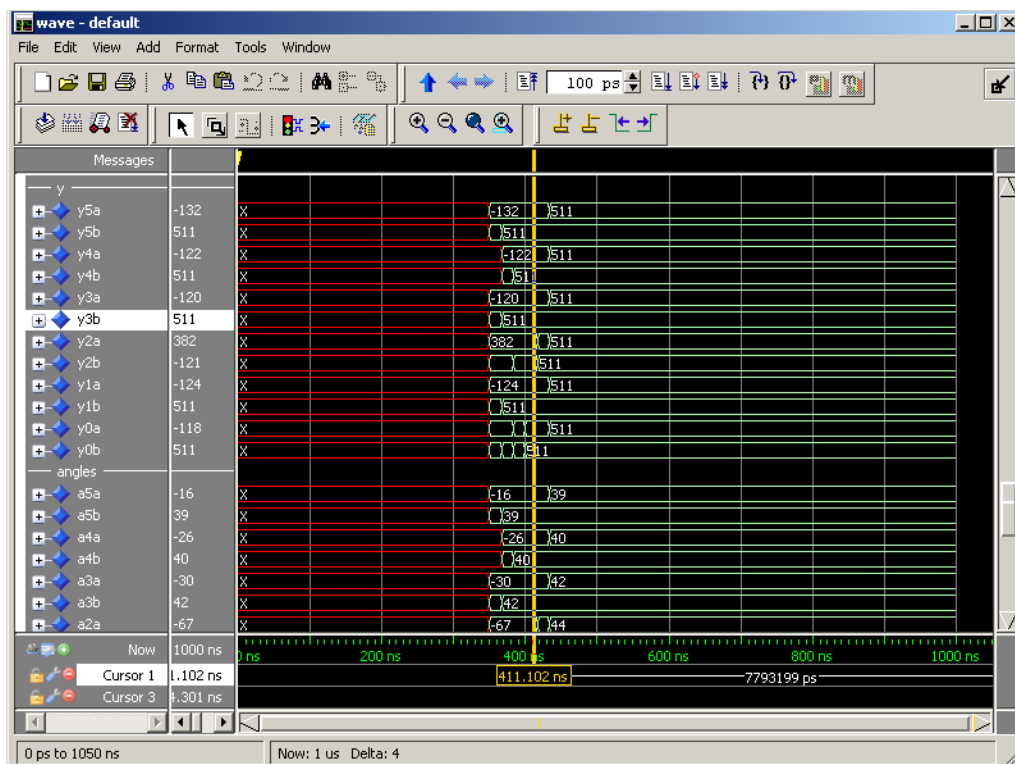


Figure 46: ModelSim Environment for comparison of the tracking simulation

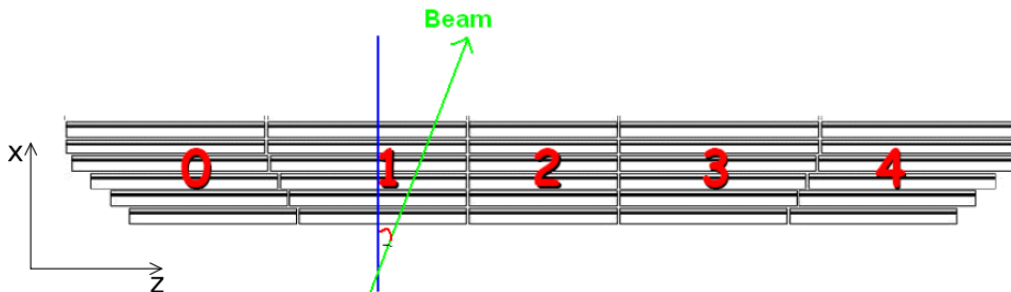


Figure 47: Incident beam on the supermodule during the 2007 testbeam. The supermodule was tilted along its z -axis resulting in the incident angle as shown in Fig. 50. For the tracking the tracklets were moved to stack 3 in order to pass the vertex constraint.

Therefore, it is not only possible to compare the final output of the two tracking implementations but also their intermediate results. This has proved extremely helpful in debugging the tracking and understanding the behaviour in special circumstances.

The output file contains the information of the found tracks (references to contributing tracklets and reconstructed quantities). This allows comparisons of the results of the two implementations.

During the implementation the results at intermediate stages, such as the output of the input units, were compared and found to be in agreement.

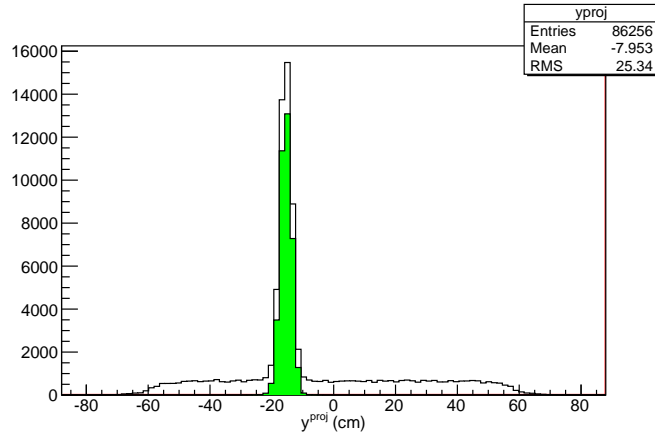
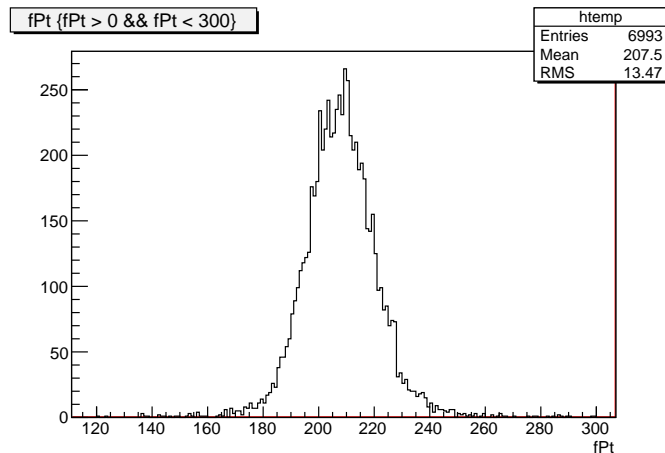
In the set of fully reconstructed tracks sometimes small deviations (on the percent level) were found in the final p_T . They arise from differences in the quantities calculated from the detector geometry. Within the simulation, the geometrical measures from the AliRoot implementation are used. The used values must be adapted for the future use.

5.6 Results

The simulation code has been included in the ALICE off-line framework, AliRoot, which is available from the official software repository [3].

The above described simulation was run on the data taken in the testbeam of Nov. 2007. A special run (r454_n12) prepared for the VHDL development [16] has been analyzed. This was used as a test for its operation although it cannot be used for optimal position resolution studies since the filter settings in these runs were not tuned. In this run random tracklets were added to check the proper tracking including the rejection of noise tracklets. Fig. 48 shows the distribution of the projected y -position for all tracklets. The green area shows the distribution of the tracklets which have been assigned to tracks. From this it can be seen that the noise tracklet are not assigned to tracks and for the real tracklets the number of non-assigned tracklets is small.

In Fig. 49 the p_T -distribution from this tracking is plotted. It was calculated

Figure 48: Projected y -position of trackletsFigure 49: p_T -distribution of tracks from the testbeam data in units of $\frac{1}{128}$ GeV/ c

under the (wrong) assumption of an axial magnetic field of 0.5 T. Considering the experimental setup with the incident beam focused to one position on the supermodule, it fulfils the expectation of a peaked shape with a finite width arising from the spread of the incoming particles (s. Fig. 47). As there was no magnetic field in the testbeam, the more meaningful quantity under these circumstances is the angle against the supermodule normal in the transverse plane. Its distribution is shown in Fig. 50.

The data taken during the cosmic runs in 2008 is not usable for this tracking analysis because the TRAPs were operated in a special mode for the cosmic trigger (s. section 4.7).

With the Monte-Carlo output from the TRAP simulation more detailed studies are possible. It allows the comparison of the reconstructed p_T to the one known from Monte-Carlo information. This requires the production of many tracks and a

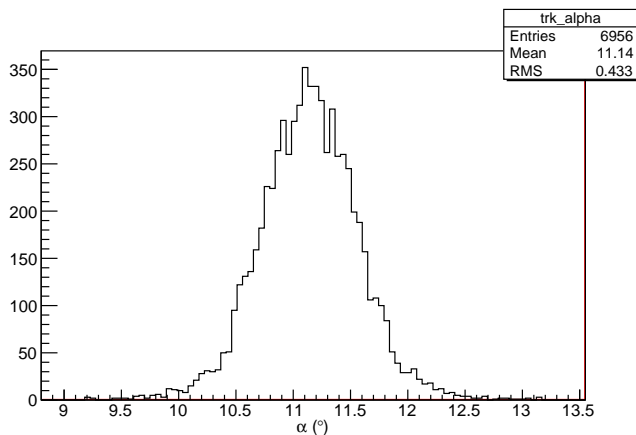


Figure 50: Track angle as reconstructed from the tracking simulation

sufficient tracklet efficiency which is not given at the moment. This requires further validations.

5.7 Open issues

A major goal of the TRD trigger is to have PID information available for the trigger decision. The PID calculation on the TRAP can be based on the charge sums in two time intervals. The production and absorption of transition radiation leads to a rise in the pulse height in the late timebins (s. Fig. 7). Thus, besides on the value of the pulse height, the electron identification can be based on the ratio of the summed charges in two time intervals. The optimal procedure is under study within the TRD collaboration. Also an algorithm for the combination of the PID information from the different layers has to be evaluated for the GTU.

A major issue is the proper setting of the TRAP filter and tracking settings as they heavily influence the later results. The optimal settings have to be found and analyzed. With the above described framework it should be possible to compare the on-line calculated tracklets to the tracklets produced during the off-line tracking. This is supposed to help in the understanding of the possible tracklet resolution and other properties.

6 Jets in TRD

The production and scattering of partons, i. e. quarks and gluons, in particle collisions can be explained on the basis of fundamental processes in QED and QCD. However, due to confinement the partons cannot be directly observed and the relevant processes can only be studied indirectly.

In experiments of e^+e^- -collisions the fundamental process:

$$e^+e^- \rightarrow \gamma^*/Z^0 \rightarrow q\bar{q} \quad (84)$$

was studied by the observation of two collimated jets of hadrons emerging from the primary vertex. The connection between the fundamental process and the detectable particles is explained as a consequence of confinement. As the emerging quarks move apart energy is stored in the intermediate colour flux tube. Eventually, it is converted in the production of particle pairs. As this process continues until only colour-neutral hadrons are left, it is called hadronization. In the end, the initial parton momentum is shared among the created hadrons (fragmentation). This leads to the experimental observation that the total momentum of the two jets (the sum of the individual momenta of the contributing particles) is balanced. Here, also the neutral particles have to be taken into account, e. g. by the detection in a calorimeter. But the full jet reconstruction which assigns the individual particles to jets is necessary to conclude on the kinematics of the initial interaction.

For quantitative analyses, the pictorial view of a jet as collimated bunch of particles is insufficient and, instead, a precise definition is needed. This is usually given by the specification of the algorithm which assigns the detected particles to jets in an iterative procedure. Thus, the algorithm is not only used for the jet finding from experimental data but also provides the definition of a jet.

The e^+e^- -reaction in Eqn. (84) provides the simplest case of jet production. In a more complicated event, a hard gluon emitted by one of the quarks leads to the evolution of a third jet. The observation of 3-jet events and their angular distribution was interpreted as evidence for the gluon as spin-1 particle [8].

In hadron collisions at LHC the events are further complicated. The initial conditions are not as clean as in e^+e^- reactions. Already for pp -collisions, the description is separated in several stages. The proton is considered to consist of a dynamical sea of partons carrying fractions of its total momentum. The valence quarks appear as the difference of quarks and antiquarks. The probability to observe a parton p with longitudinal momentum fraction x in an interaction with momentum transfer Q^2 is characterized by the parton distribution function $f_p(x, Q^2)$. The partons interact with each other according to the cross-sections of the fundamental processes.

In heavy-ion collisions, such as PbPb, the situation is even more complicated due to the many participating nucleons. Models have evolved to describe the outcome of such reactions.

If hard quarks are produced in the initial interaction their fragmentation will result in observable jets. For the hard interaction cross sections can be calculated perturbatively. The non-perturbative process of hadronization is characterized by fragmentation functions $D_p^h(z)$ specifying the probability of the creation of a hadron h with a fraction of the momentum z from an initial parton p . The fragmentation functions are subject to phenomenological models and experimental studies. They contain information on the conditions in which the system undergoes the hadronization. For heavy-ion collisions, in which a medium is created by soft interactions, a softening of the fragmentation is expected due to the medium traversal of the partons prior to fragmentation.

6.1 Expectations for ALICE

ALICE aims at the observation of jet events as they can provide access to in-medium effects and the medium properties. Both, the total energy of the jet and the fragmentation function should be affected by the presence of a medium. Thus, they should differ in pp - and PbPb-collisions.

In a heavy-ion collision the partons created in a hard interaction propagate through a volume of high particle density. During the passage through the medium the hard partons scatter and, thus, loose energy. The details of the energy loss, e. g. the mass dependency, should contain information on the medium properties. It is believed that the effects are still visible on the level of jets, i. e. the fragmented products of the initial partons. Therefore, jets are considered as valuable probes for the in-medium modifications. The measurements are based on comparisons between jet observables in pp - and PbPb-collisions.

Assuming the above explained separation of the jet creation in different stages which are treated independently, the cross section for jet creation can be calculated from the fundamental parton-parton cross-sections and the parton distribution functions:

$$\frac{d\sigma^{NN}}{d^3p} = K \sum_{a,b,c,d} \int dx_a \int dx_b f_{a/p}(x_a, Q_a^2) f_{b/p}(x_b, Q_b^2) \frac{d\sigma^{(ab \rightarrow cd)}}{d\hat{t}} \delta(\hat{s} + \hat{u} + \hat{t}) . \quad (85)$$

The sum is taken over all underlying hard processes with emerging partons. Hereby, it is assumed that all such reactions result in jet events.

With a target luminosity of $5 \cdot 10^{26} \text{cm}^{-2} \text{s}^{-1}$ for PbPb-collisions at the LHC, the number of jets to be expected within the the central barrel and EMCAL acceptance can be estimated [2], as shown in Table 13.

Due to the low fraction of high momentum jet events in the total cross section they have to be enhanced by a dedicated trigger in order to acquire a sufficiently large sample of jet events in the available recording bandwidth.

$E_{t,min}(GeV)$	within central barrel	within EMCAL
20	$2.0 \cdot 10^9$	$2.4 \cdot 10^8$
50	$4.8 \cdot 10^7$	$5.8 \cdot 10^6$
100	$2.6 \cdot 10^6$	$3.1 \cdot 10^5$
150	$4.0 \cdot 10^5$	$4.8 \cdot 10^4$
200	$1.0 \cdot 10^5$	$1.2 \cdot 10^4$
250	$2.5 \cdot 10^4$	$3.0 \cdot 10^3$

Table 13: Expected number of jets above a given $E_{T,min}$ in the ALICE central barrel and EMCAL acceptance in one month PbPb running at the target luminosity of the LHC [2]

6.2 Jet trigger

To enhance the sample of acquired jet events a trigger is needed. It has to judge at an early stage of data-taking whether the event is worth to continue its further readout. This requires simple yet sensitive variables as basis for the decision.

Characteristically, a jet leads to a high energy content within a relatively small area in the $\eta - \varphi$ -plane. For a 50 GeV jet a cone of radius $R_c = 0.2$, i. e. an area determined by $\Delta\eta^2 + \Delta\varphi^2 < R_c^2$, contains more than 40 % of the energy[2], and higher jet energies result in a stronger collimation. This cone area corresponds approximately to the area covered by a TRD stack.

The simplest decision for jet finding would just require a single charged high- p_T particle above a threshold p_T^{cut} . Such a particle can result from the fragmentation and indicate the existence of a jet. On the other hand, this method biases the decision towards jets with hard fragmentation.

A more moderate decision can be achieved by basing it on the deposited energy in an area of certain size, typically a cone of given radius R_c within the detector. Such triggers are often implemented in calorimeters as they are also sensitive to neutral particles, e. g. EMCAL in ALICE. This has the advantage that they are resilient to charged-neutral fluctuations. Nevertheless, a similar approach is foreseen for the TRD. Here the decision can be based on the p_T instead of energy of the tracks reconstructed in the GTU (s. chapter 5).

To study the reconstruction and triggering of jets simulated events can be used. To analyze the dependency on the jet energy the events are grouped in bins of transverse energy in the initial hard interaction. For comparability, within ALICE usually the same set of bins is used as in the Physics Performance Report [2]. The values are listed in Table 14.

In the following, simulated events from pp -collisions, generated by PYTHIA within the AliRoot framework, are used to discuss possible trigger scenarios of the TRD. The same event generator settings have been used as for the simulations for the Physics Performance Report studies. The jet energy range of 104 – 125 GeV/c

Jet energy range
20 - 24 GeV
24 - 29 GeV
29 - 35 GeV
35 - 42 GeV
42 - 50 GeV
50 - 60 GeV
60 - 72 GeV
72 - 86 GeV
86 - 104 GeV
104 - 125 GeV
125 - 150 GeV
150 - 180 GeV

Table 14: Binning of jet energies as used in ALICE [2]

has been chosen. For this discussion, only 100 events have been simulated as the aim is only to sketch the idea of a possible trigger. Quantitative estimates are outside the scope of this thesis.

As mentioned before, the simplest implementation of a jet trigger would require a single charged particle with a p_T above a given threshold. To study the efficiency of such a trigger, for every event the highest p_T of any charged particle is filled into a one-dimensional histogram. If this is done for a set of events, the histogram can be used to see which fraction of the events would pass a specific threshold.

For the study of a more moderate decision, the p_T of all charged particles in η - φ -regions corresponding to TRD stacks is summed in a two-dimensional histogram (s. Fig. 51), separately for every event. To study a trigger based on the abundance of a p_T -sum above a threshold, the maximum value in this two-dimensional histogram is filled into a histogram corresponding to the one for the single-particle p_T . This can be used to derive the efficiency of a cut on the summed p_T .

Starting from full Monte-Carlo information, further constraints are added and finally only the tracks as available at the L1 time are used for the analysis.

6.2.1 Full Monte-Carlo information

In the first step, events are analyzed based on the full Monte-Carlo information in order to check for the limitations and as best case reference.

Fig. 51 shows the summed p_T of all primary charged particles where the binning of the histogram corresponds to the TRD geometry. The maximum entry is used to fill the histogram for the summed p_T cut study.

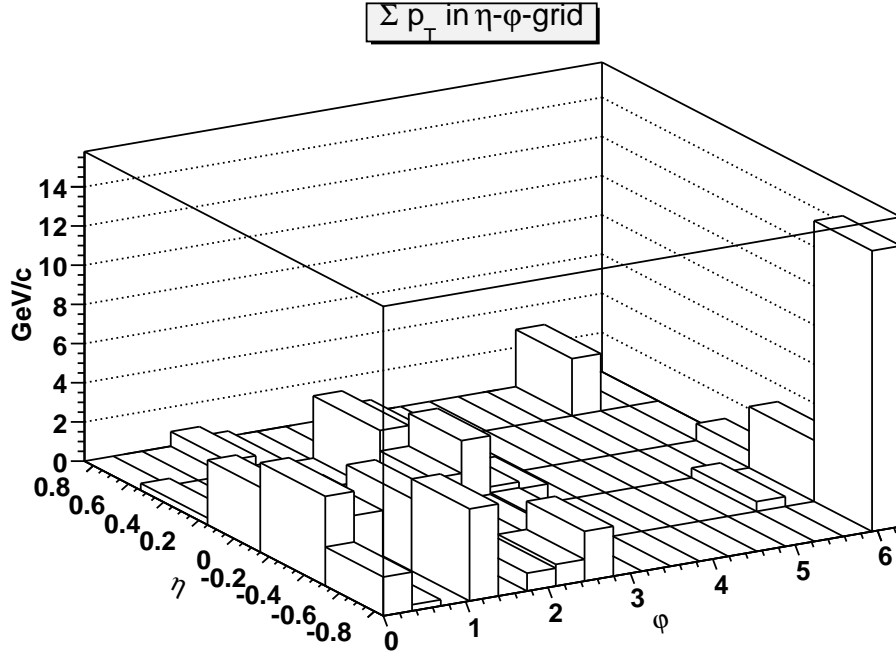


Figure 51: Transverse momentum in η - ϕ of one jet event. All primary Monte-Carlo tracks of charged particles within the acceptance are included.

6.2.2 Monte-Carlo tracks in the TRD

An important limitation is to take into account that only tracks traversing at least 4 layers of the TRD within one stack are trackable.

During the particle transport in the simulation, track references are stored. They contain the information on the parts of the detector which each particle traversed. From this information it is checked how many layers of the detector are traversed. The analysis uses only those tracks which pass through at least four layers in the TRD. Additionally, to get closer to the trigger situation the histograms are filled according to the stack and sector in which a track was detected. This leads to a smearing as the tracks are bent in the magnetic field.

6.2.3 Reconstructed tracks

To see the signatures which are amenable to an off-line analysis the above procedure is also performed for reconstructed tracks, i. e. all tracks contained in the ESD from the global reconstruction (i. e. including the TPC) which have passed at least 4 TRD layers. The resulting plots show how the data would be seen in an off-line analysis.

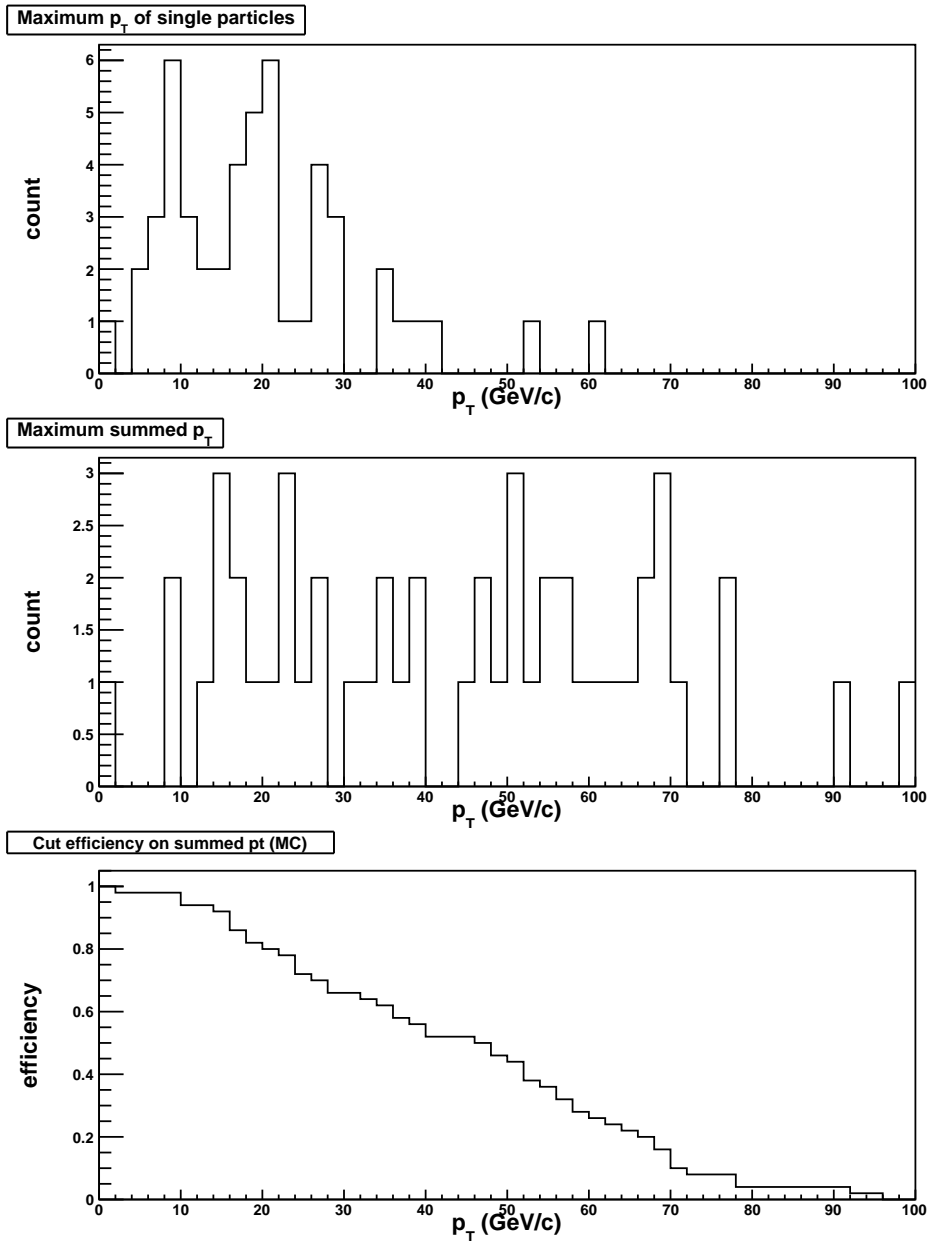


Figure 52: The upper two plots show the maximum single and summed p_T for a jet event based on Monte-Carlo tracks. The lower plot shows the efficiency of a p_T -cut.

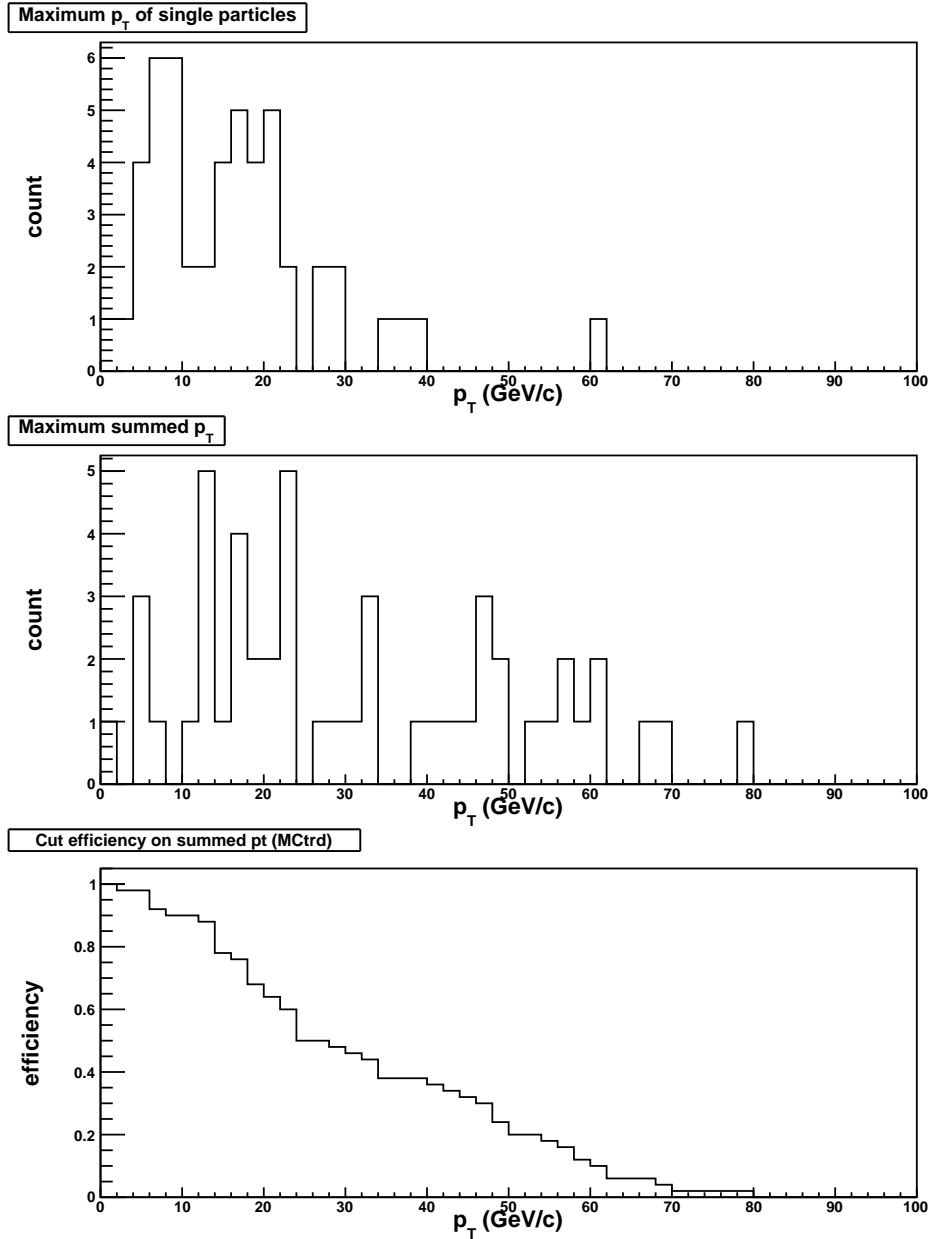


Figure 53: The upper two plots show the maximum single and summed p_T for a jet event based on Monte-Carlo tracks which traverse at least 4 TRD layers. The lower plot shows the efficiency of a p_T -cut.

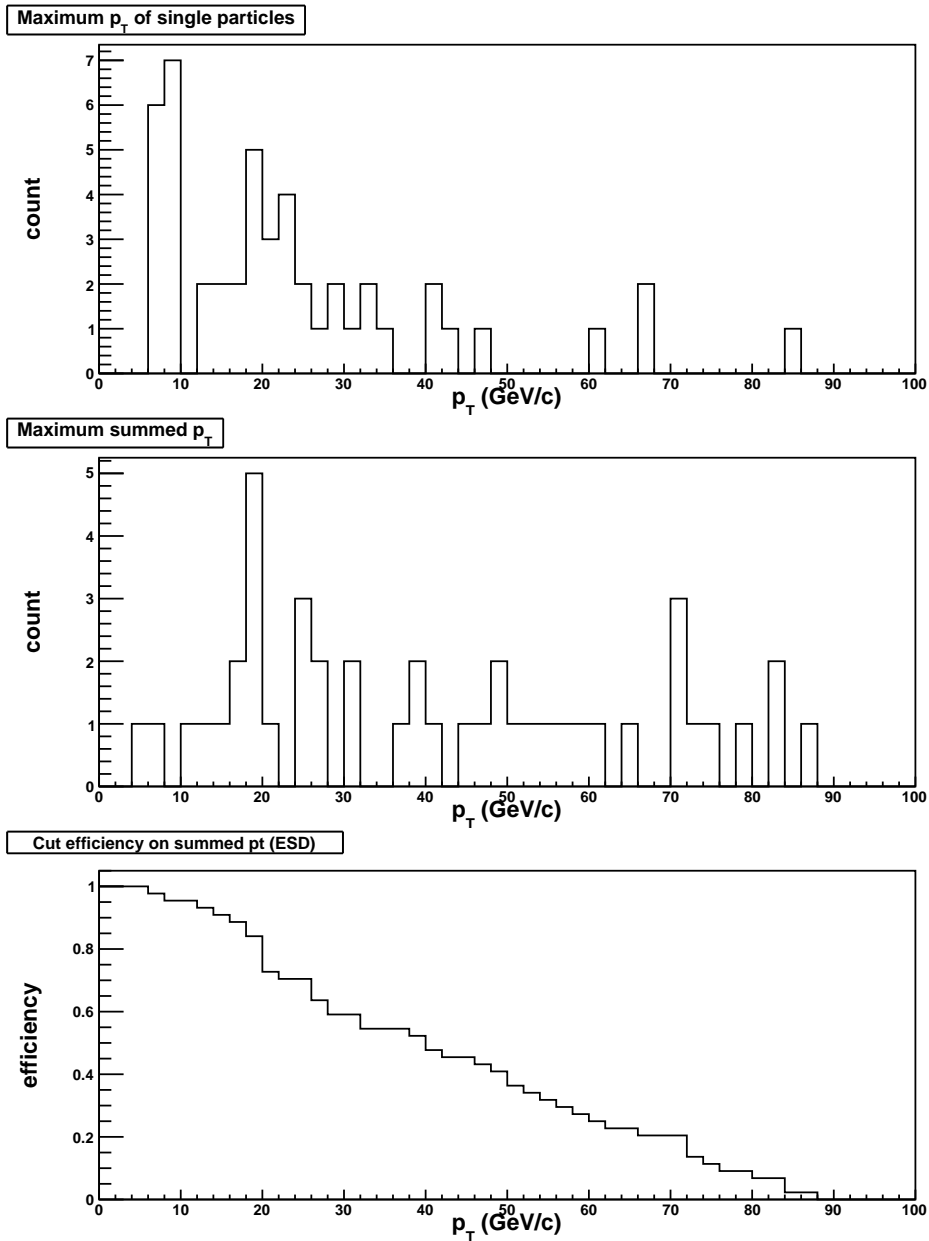


Figure 54: The upper two plots show the maximum single and summed p_T for a jet event based on reconstructed tracks. The lower plot shows the efficiency of a p_T -cut.

6.2.4 L1-reconstructed tracks

The final step is to simulate the information available for the trigger decision, i. e. at the GTU. Here, less information is reconstructed compared to the off-line tracking. Besides the known stack of the track, only the transverse momentum is reconstructed. Furthermore, the on-line tracking can only reconstruct tracks above a minimum p_T threshold of about 2.3 GeV/c.

6.3 Results and Outlook

The analysis described here has been implemented as AliAnalysisTask such that it can be run within the official analysis framework. At the moment it does not give quantitative results. For reliable statements on the possible trigger efficiencies more elaborate studies are needed. Some of the issues are discussed in the following.

A more precise track selection of the TRD relevant tracks (as discussed in section 6.2.2) is needed to take into account only such tracks which can be potentially found in the on-line tracking. So far only the requirement of at least four TRD layers has been used.

The generation of the tracklets required for the GTU tracking in a Monte-Carlo production is based on simulation of the TRAP processing. Studies on the efficiency of the tracklet production and the quality of the tracklet parameters are needed, including a comparison to the real hardware. By now, the TRAP simulation has been extended by the production of Monte-Carlo labels such that comparisons results become possible. In the simulation used for this discussion, the p_T -cut on the tracklet level was disabled as it appeared malfunctioning.

For reliable simulations it is important to keep the software model close to the hardware implementation such that the output of the two tracking algorithms is identical.

For reliable statements on trigger efficiencies, biases etc. more detailed studies are needed. With the availability of the GTU tracks within the analysis framework this comes into reach. On the other hand, it has to be kept in mind that ideas for the trigger implementations have to be feasible for the hardware implementation.

Furthermore, it will be necessary to analyze the influence of the high background multiplicity in PbPb-collisions. As the TRD only detects the charged part of the jet, charged-neutral fluctuations have to be considered as well.

As discussed above these analysis could also be done on real data — without any simulation uncertainties — once the data-taking has started.

This discussion is intended to show the study of a jet trigger in principle without leading to any quantitative result. This is due to uncertainties in the simulation chain that relies on the proper simulation of the hits, the local tracklet calculation in the TRAPs and the final tracking in the GTU.

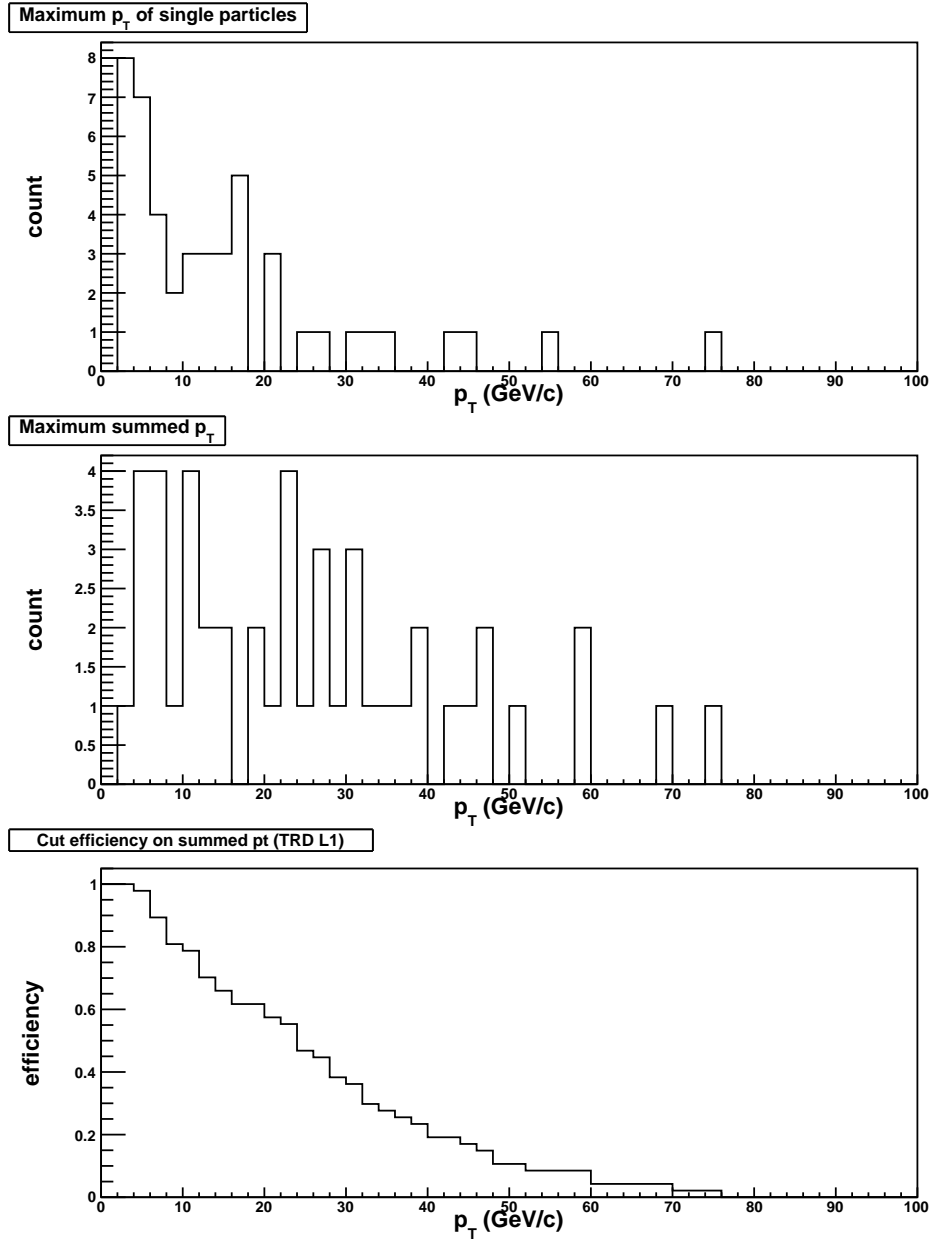


Figure 55: The upper two plots show the maximum single and summed p_T for a jet event based on tracks from the GTU tracking. The lower plot shows the efficiency of a p_T -cut.

7 Summary

During the time of this thesis, LHC and ALICE have reached their start-up phase. Within ALICE the Transition Radiation Detector plays an important role for the separation of electrons from a large pion background. Furthermore, these capabilities can be used as basis for a fast L1 trigger contribution.

With the TRD supermodules being built at the University of Münster and transported to CERN, an additional testing setup is needed at the experimental site. This was used for extensive tests of new supermodules during which experience was gathered on especially critical parts. Optimal procedures with respect to the consumed time have been established for the testing routines.

In two supermodules fundamental issues in the gas system were found and prevented the installation. The investigation required the disassembly of the supermodules after which the problems could be understood and fixed. In the end, the detectors were reassembled and made ready for installation.

During the installation and commissioning of the first supermodules in the experimental cavern experience was gathered on critical items and the helpful preparations prior to the installation. A well-prepared supermodule installation can be finished within a few days up to first data-taking. Most of the preparations for the installation of the next supermodules have already been done.

During the 2008 cosmic runs, the four installed supermodules were included in ALICE-wide data-taking and the TRD could participate stably in several cosmic runs.

As was discussed in the second part of the thesis, the off-line code of the TRD in the ALICE framework AliRoot has been extended by the simulation of the Global Tracking Unit. The simulation was designed to reproduce the output of the tracking algorithm as used on the FPGA-based trigger electronics bit-equivalently. Furthermore, it can accept tracklets from different sources to allow comparisons and understand possible inefficiencies. The output of this tracking simulation can be automatically added to the ALICE Event Summary Data. From there it can be accessed within the Analysis framework such that the information can be easily retrieved. This simulation shall be used in detailed studies for TRD trigger implementations as has been sketched for the case of a TRD jet trigger.

In order to produce reliable statements on trigger efficiencies and biases from simulated data, the input to the tracking algorithm, i. e. the tracklets, needs further studies. The tracklet calculation in the TRAP depends crucially on the settings of the filters and parameters, such as the drift velocity. These dependencies have to be studied and taken into account in the detector configuration.

As the TRD tracklets are part of the raw-data, they can be analyzed off-line. Additionally, the tracking and trigger algorithm can be tuned off-line on the basis of real events. In this way the simulation uncertainties from signal creation etc. can be avoided.

ACKNOWLEDGMENTS First of all, I would like to thank Prof. Dr. Johanna Stachel for the great opportunity to work on the interesting and versatile topic during a lively time at CERN.

My special gratitude goes to Dr. Ken Oyama for his support and many enlightening discussions.

Furthermore, I am very grateful to Jan de Cuveland, Stefan Kirsch and Felix Rettig for the close collaboration in many occasions.

Also, I want to express my gratitude to Dr. Tom Dietel for many instructive discussions.

For the detailed review of my thesis, I am indebted to Stefan Kirsch, Jochen Thaeder, Dr. Ken Oyama, Dr. Kai Schweda and Dr. Tom Dietel.

And I want to express my gratitude to many people from the group and the whole collaboration.

Last but not least, I thank my parents who supported me during my studies.

A Technical Data and Specifications

A.1 Tracking parameters

Parameter	Symbol	Value
resolution of deflection length	d_{res}	140 μm
resolution of y position	y_{res}	160 μm
projection plane	x_{mid}	332.1 cm
drift length	l_{Drift}	3 cm
x of layer 5	x_5	363.6 cm
x of layer 4	x_4	351.0 cm
x of layer 3	x_3	338.5 cm
x of layer 2	x_2	325.9 cm
x of layer 1	x_1	313.3 cm
x of layer 0	x_0	300.6 cm

Table 15: Tracking parameters which enter in the tracking simulation

k	$i = 0$	$i = 1$	$i = 2$	$i = 3$	$i = 4$	$i = 5$
15	6.72	6.45	-6.20	-5.97	0.00	0.00
23	6.80	0.00	0.33	0.00	-6.13	0.00
27	5.57	2.70	0.00	-2.50	-4.77	0.00
29	6.80	0.00	0.33	0.00	-6.13	0.00
30	0.00	6.97	6.70	-6.45	-6.22	0.00
31	5.44	2.69	0.27	-2.49	-4.90	0.00
39	2.93	5.58	-2.70	0.00	0.00	-4.81
43	0.00	7.05	0.00	0.33	0.00	-6.38
45	7.20	0.00	-6.64	6.40	0.00	-5.95
46	0.00	7.05	0.00	0.33	0.00	-6.38
47	2.93	5.45	-2.70	0.26	0.00	-4.94
51	3.61	3.47	0.00	0.00	-3.10	-2.99
53	6.80	0.00	0.33	0.00	-6.13	0.00
54	0.00	5.77	2.80	0.00	-2.59	-4.97
55	3.53	3.47	0.17	0.00	-3.18	-2.99
57	5.73	0.00	0.00	2.57	-4.90	-2.39
58	0.00	7.05	0.00	0.33	0.00	-6.38
59	3.61	3.39	0.00	0.16	-3.09	-3.07
60	0.00	0.00	7.22	6.95	-6.70	-6.47
61	5.59	0.00	0.27	2.56	-5.04	-2.39
62	0.00	5.64	2.79	0.27	-2.59	-5.10
63	3.53	3.39	0.17	0.16	-3.18	-3.07

Table 16: Values of $A_{k,i}$

Layer	z_{ch}	$z = 0$	1	2	3	4	5	6	7	8	9	10	11	12	13	14	15
0	0	0	1	1	0	2	2	0	3	3	4	4	4	5	5	5	6
0	1	0	0	1	1	0	2	2	0	3	3	4	4	4	5	5	5
0	2	0	0	0	1	1	0	2	2	3	3	3	4	4	4	5	5
1	0	1	0	2	2	0	3	3	0	4	4	4	5	5	5	6	6
1	1	1	1	0	2	2	0	3	3	3	4	4	4	5	5	5	0
1	2	0	1	1	0	2	2	0	3	3	3	4	4	4	5	5	5
2	0	1	0	0	2	0	0	3	0	0	4	0	0	5	0	0	6
2	1	0	1	0	0	2	0	0	3	0	0	4	0	0	5	0	0
2	2	0	0	1	0	0	2	0	0	3	0	0	4	0	0	5	0
3	0	1	1	0	2	2	0	3	3	4	4	4	5	5	5	6	6
3	1	0	1	1	0	2	2	0	3	3	4	4	4	5	5	5	0
3	2	0	0	1	1	0	2	2	3	3	3	4	4	4	5	5	5
4	0	1	1	0	2	2	0	3	3	4	4	4	5	5	5	6	6
4	1	0	1	1	0	2	2	0	3	3	4	4	4	5	5	5	0
4	2	0	0	1	1	0	2	2	3	3	3	4	4	4	5	5	5
5	0	1	0	2	2	0	3	3	0	4	4	0	5	5	0	6	6
5	1	1	1	0	2	2	0	3	3	0	4	4	0	5	5	0	0
5	2	0	1	1	0	2	2	0	3	3	0	4	4	0	5	5	0

Table 17: Listing of the z -channel map for Stack 0: The resulting z_{idx} for different layers and z_{ch} are shown. A vaule of 0 indicates that the tracklet does not belong to this z -channel.

B Checklists

B.1 Surface testing checklist

	✓
Low voltage connections tight	
PDB connectivity	
Powering up	
PDB redundancy	
Ethernet to DCS boards	
FEE configuration	
Cooling tightness and operation	
Optical ORI output (GTU : monitor)	
Trigger	
Gas system tightness	
High voltage	
Stress test	
JTAG test	

B.2 Pre-Installation checklist

	✓
DCS-power sharing with neighbouring sector installed and checked	
LV for FEE checked	
PSU reachable via Ethernet and integrated to PVSS	
Optical fibres installed and routed from patch-panel to back-frame and GTU to C-rack patch-panel	
Cooling lines tested and properly routed	
Cooling emergency drain with safety valve properly routed	
Ethernet cables tested and routed	
HV cables tested and routed	
Gas connections prepared	

Some of the tests have already been done for all sectors and it only has to be verified that no damages during later work occurred.

B.3 Commissioning checklist

	✓
Low voltage properly connected, voltages and polarity verified	
DCS boards working	
Sufficient cooling	
Voltage sensing on the power bus bars	
Front-End Electronics configuration	
Trigger distribution	
Readout and mapping	
Noise readout	
High voltage	
Gas system	

C Observed problems

C.1 Supermodule I (Sector 8)

- non-configurable chambers:
 - S2L0 (from the beginning)
 - S0L1
 - S0L4
 - S1L2 (since 2008, Sep. 15th)
 - S3L0
- power bus bar sensing wrongly connected
- gas leaks

C.2 Supermodule II (Sector 0)

- no cooling in S2L5, S3L5
- no optical output in:
 - S0L2A
 - S3L2 weak
 - S4L4
 - S4L5B
- dead DCS board: S2L5
- gas leaks

C.3 Supermodule V (Sector 17)

- S2L0 sometimes high temperature

References

- [1] John Adams et al. Experimental and theoretical challenges in the search for the quark gluon plasma: The STAR collaboration's critical assessment of the evidence from RHIC collisions. *Nucl. Phys.*, A757:102–183, 2005. doi:10.1016/j.nuclphysa.2005.03.085. nucl-ex/0501009.
- [2] ALICE Collaboration, Bruno Alessandro, Federico Antinori, Jouri A Belikov, Christoph Blume, Andrea Dainese, Panagiota Foka, Paolo Giubellino, Boris Hippolyte, Christian Kuhn, Gines Martínez, Marco Monteno, Andreas Morsch, Tapan Nayak, Joakim Nystrand, Mercedes López Noriega, Guy Paic, Jan Pluta, Luciano Ramello, Jean-Pierre Revol, Karel Safarik, Jürgen Schukraft, Yves Schutz, Enrico Scomparin, Raimond Snellings, Orlando Villalobos Baillie and Ermanno Vercellin. Alice: Physics performance report, volume ii. *Journal of Physics G: Nuclear and Particle Physics*, 32(10):1295–2040, 2006. URL <http://stacks.iop.org/0954-3899/32/1295>.
- [3] Aliroot. URL <http://alisoft.cern.ch/AliRoot/>.
- [4] Anton Andronic et al. Space charge in drift chambers operated with the Xe,CO₂(15%) mixture. *Nucl. Instrum. Meth.*, A525:447–457, 2004. doi:10.1016/j.nima.2004.01.076. physics/0402043.
- [5] Venelin Angelov. Design and performance of the ALICE TRD front-end electronics. *Nucl. Instrum. Meth.*, A563:317–320, 2006. doi:10.1016/j.nima.2006.02.169.
- [6] Venelin Angelov et al. ALICE TRAP User Manual, 2008.
- [7] Raphaelle Bailhache and Christian Lippmann. New test beam results with prototypes of the ALICE TRD. *Nucl. Instrum. Meth.*, A563:310–313, 2006. doi:10.1016/j.nima.2006.02.157.
- [8] R. Brandelik et al. Evidence for a spin-1 gluon in three-jet events. *Phys. Lett. B*, 97, Issues 3-4:453–458, 1980.
- [9] Olivier Brüning, Paul Collier, P Lebrun, S Myers, Ranko Ostojic, John Poole, and Paul Proudlock. LHC Design Report. Technical report, CERN, 2004.
- [10] Federico Carminati, Panagiota Foka, Paolo Giubellino, Andreas Morsch, Guy Paic, Jean-Pierre Revol, Karel Safarik, Yves Schutz, and Urs Wiedemann. Alice: Physics performance report, volume i. *Journal of Physics G: Nuclear and Particle Physics*, 30(11):1517–1763, 2004. URL <http://stacks.iop.org/0954-3899/30/1517>.

REFERENCES

- [11] CERN. New state of matter created at cern, 2000. URL <http://press.web.cern.ch/press/PressReleases/Releases2000/PR01.00EQuarkGluonMatter.html>.
- [12] ALICE Collaboration. Letter of intent for a large ion collider experiment. Technical Report CERN-LHCC 93-16, CERN, 1993.
- [13] ALICE Collaboration. ALICE technical proposal. Technical report, CERN, 1995.
- [14] ALICE Collaboration. ALICE TRD Technical Design Report. Technical Report CERN/LHCC 2001-021, CERN, 2001.
- [15] ALICE Collaboration. Technical Design Report of the Trigger Data Acquisition High-Level Trigger and Control System. Technical Report CERN/LHCC 2003-062, CERN, 2004.
- [16] Jan de Cuveland. private communication.
- [17] Jan de Cuveland. Entwicklung der globalen Spurrekonstruktionseinheit für den ALICE-Übergangsstrahlungsdetektor am LHC (CERN), 2003.
- [18] Jan de Cuveland, Felix Rettig, and Stefan Kirsch. Alice trd daq data format, 2008.
- [19] Clara Gaspar. *DIM*. CERN, 2008. URL <http://dim.web.cern.ch/dim>.
- [20] Clemens Haltebourg. Implementation of the alice trd trap-chip into aliroot, 2008.
- [21] Stefan Kirsch. Development of the supermodule unit for the alice trd, 2007.
- [22] Stefan Kirsch and Jochen Klein. TRD online checker.
- [23] Tobias Krawutschke et al. Dcs board documentation. URL <http://www.kip.uni-heidelberg.de/ti/DCS-Board/current/index.html>.
- [24] MinJung Kweon. Private communication.
- [25] William R. Leo. *Techniques for Nuclear and Particle Physics Experiments*. Springer-Verlag, 2nd revised edition, 1994.
- [26] Yuval Ne'eman and Yoram Kirsh. *The particle hunters*. Cambridge University Press, 1st edition, 1986.
- [27] Ken Oyama, Clemens Adler, Venelin Angelov, David Emschermann, and Christian Lippmann. Alice trd raw data format specification, 2008.

- [28] Donald H. Perkins. *Introduction to High Energy Physics*. Cambridge University Press, 2nd edition, 2000.
- [29] Felix Rettig. Private communication.
- [30] Felix Rettig. Entwicklung der optischen ausleseketten fuer den alice trd, 2007.
- [31] Root. URL <http://root.cern.ch>.
- [32] Jens Steckert. Design and implementation of a high-reliability dcs-board power control system for the alice trd detector, 2007.
- [33] D. Sundarajan. *The Discrete Fourier Transform*. World Scientific, 1st edition, 2001.
- [34] TRD software repository. URL <http://alice.physi.uni-heidelberg.de/svn/trd/>.
- [35] Timing, Trigger and Control (TTC) Systems for the LHC. URL <http://ttc.web.cern.ch/TTC/intro.html>.
- [36] Uwe Westerhoff. Private communication.
- [37] Alexander Wilk. Analysis of the electron / pion separation capability with real size ALICE TRD prototypes using a neural network algorithm. *Nucl. Instrum. Meth.*, A563:314–316, 2006. doi:10.1016/j.nima.2006.02.165.
- [38] Nu Xu. private communication.

REFERENCES

Erklärung:

Ich versichere, dass ich diese Arbeit selbständig verfasst habe und keine anderen als die angegebenen Hilfsmittel benutzt habe.

Heidelberg, den 5. November 2008